SCHMIDT, KIRBY B., Ph.D. Exploiting Nanoscale Variations in Two Dimensional Materials for Predicting Material Properties and Machine Vision Applications. (2023) Directed by Dr. Tetyana Ignatova. 116 pp.

Two dimensional nanomaterials are atomically thin sheets of molecules that have properties significantly different to their bulk counterparts. This dissertation investigates the electronic and optical properties of two dimensional materials and their Van der Waals heterostructures, employing Raman spectroscopy as a powerful tool for characterization. A relationship between strain, doping and photoluminescence in Van der Waals heterostructures is established which contribute to the nanovariations to the optical signal in microscale devices. These nanoscale variations in a two dimensional sensing devices contribute to inaccuracies in the detection of analytes adsorbed to the surface. Further, Machine vision techniques are also utilized to enhance the efficiency and accuracy of Raman spectroscopy data analysis and image registration. This registration leads to novel analysis of multispectral images. The research uses advanced strain analysis from Raman spectroscopy of two dimensional nanomaterials to register Raman spectral maps with images of data acquired from different microscopic techniques, such as Scanning Electron Microscopy, Kelvin Probe Force Microscopy, and Scanning Near-Field Optical Microscopy. Optical microscopy is also used for the rapid identification of high quality cleaved two dimensional flakes in an automated way. A one-stage object detection neural network is used for identifying high quality nanoflakes, and the model uses reinforcement learning as new high quality flakes are confirmed via Raman spectroscopy. Novel machine vision techniques are further used to subsegment multiterraced layers. The results contribute to the advancement of two dimensional materials research and provide insights into potential applications of

these materials in various fields.

EXPLOITING NANOSCALE VARIATIONS IN TWO DIMENSIONAL
MATERIALS FOR PREDICTING MATERIAL PROPERTIES AND MACHINE
VISION APPLICATIONS

by

Kirby B. Schmidt

A Dissertation Submitted to

the Faculty of The Graduate School at

The University of North Carolina at Greensboro

in Partial Fulfillment

of the Requirements for the Degree

Doctor of Philosophy

Greensboro

2023

Approved by

_____

Committee Chair

This dissertation written by Kirby B. Schmidt has been approved by the following committee of the Faculty of The Graduate School at The University of North Carolina at Greensboro.

Committee Chair _____

Tetyana Ignatova

Committee Members _____

Joseph Starobin

_____

Shyam Aravamudhan

_____

Hemali Rathnayake

_____

Date of Acceptance by Committee

_____

Date of Final Oral Examination

ACKNOWLEDGMENTS

I would like to thank my committee for their input on this dissertation and my research plan. I would like to thank NSF for their funding, and Brookhaven National Lab for the use of their equipment, and the internship opportunity I had with them. Finally, I would like to thank my advisor Dr Ignatova for her advice, encouragement, and endless patience.

Table of Contents

List of Tables

List of Figures

Chapter 1: Introduction

1.1   Overview and Motivations

Heterostructures of stacked two dimensional (2D) materials have developed into a major field in materials and condensed matter physics in recent years. Research on the novel exotic phenomena that emerge when layered materials are reduced to a single layer, and this is novel phenomena is compounded by combining dissimilar materials through 'stacking' to form heterostructures. The interactions between these layers in these heterostructures are often more than the sum of their parts. In addition to fundamental materials properties, the ultimate length scale of these materials and their promising properties are hoped to eventually turn into practical applications and devices. 2D materials are the individual or few layered sheets of bulk layered Van der Waals materials. These bulk Van der Waals materials have strong covalent or ionic bonds in the 2D plane but are glued together by weakly interacting Van der Waals interactions out of plane. These materials are often one atom thick, like graphene and boron nitride, or consist of multiple layers of atoms like transition metal dichalcogenides (TMDCs). In the latter, chalcogenide layers sandwich a transition metal, creating a 3 atom thick monolayer. In fig 1.1 a graphene TMDC heterostructure is shown. The first discovered, and most widely studied of these materials is graphene, and is the primary discussion of this dissertation.

Graphene is a single layer of sp^2 bound carbon atoms in a hexagonal pattern. It is an isolated layer of the bulk graphite mineral. Graphene in particular is an exciting material because of its high electron mobility and ease of doping. Because of the extreme
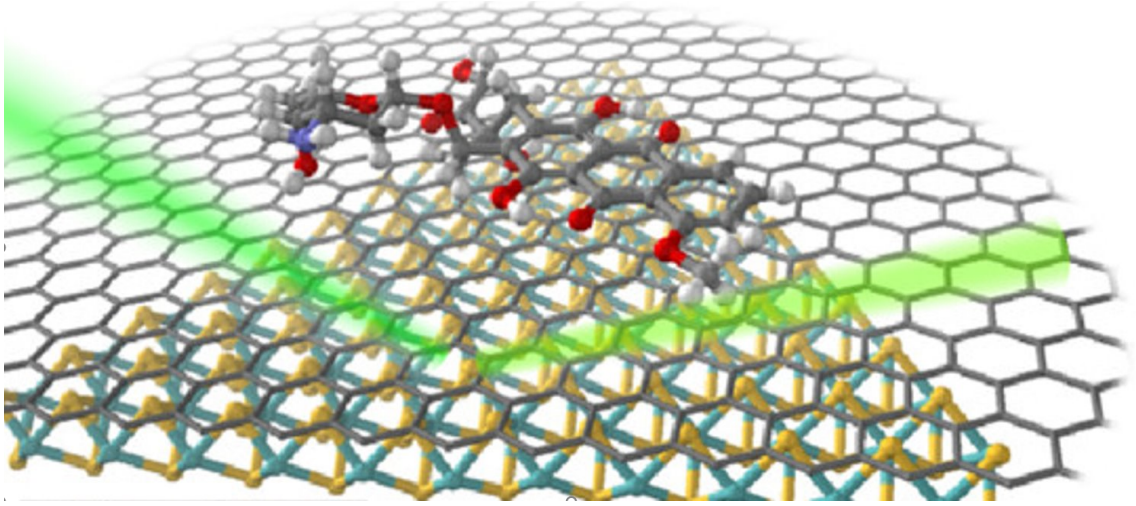
Figure 1.1. A schematic representation of a Van der Waals heterostructure device. The bottom layer is a monolayer molybdenum disulfide MoS_2 flake, the top layer is a monolayer graphene sheet. The heterostructure has a doxorubicin molecule adsorbed to the surface. In section 4 we describe probing this heterostructures electronic structure to detect the adsorbed molecule.

exposed surface area, two dimensional materials are highly designable. Graphene has been fabricated into field-effect transistors, inductors, antennas, waveguides, and a host of other devices [13, 16]. Due to its high strength and flexibility it is also seen as a primary candidate for flexible devices[1]. Flexible optoelectronic devices like lasers, LEDs, modulators and solar cells have been proposed that operate from the UV spectrum down to the terahertz range [21]. This is because of graphene's unique optical and electronic properties such as its ultrahigh carrier mobility, zero bandgap, tunable work function, fast carrier dynamics and strong light-matter coupling[43, 52, 147].

Molybdenum disulfide is another material that is a hot topic in the two dimensional devices field. It was one of the first two dimensional materials isolated after graphene and has a number of properties that make it ideal for fabricating devices with, including a tuneable direct bandgap with large on/off ratios and absorption in the visible spectrum[113, 143]. MoS_2 is also flexible, and with its superior semiconducting

properties compared to graphene it is natural to assume it can be used in flexible electronics.

Layered Double hydroxides (LDH) are ionic solids made out of metal cations sandwiching a layer of hydroxide anions. Research is ongoing in using these layered double hydroxide materials as catalytic materials and in electrodes. Research into the use of these layered double hydroxide materials in heterostructures is lacking. But layered double hydroxide materials offer interesting applications in ion transport and anion replacement inside of these Van der Waals heterostructures.

Fabrication of these materials is also a labor intensive process that is prone to error and inconsistent results. The process generally involves a bottom up approach or a top down approach. Bottom up approaches are the growth of monolayer materials, often on conductive substrates. Top down approaches are exfoliation methods where single layers are taken from a bulk crystal. Both methods have their advantages and disadvantages, but from the growth substrate or from the crystal, transfer is inevitable. This transfer process often damages the two dimensional materials, and detecting damaged flakes is a laborious process. From cleaved samples, the researcher must sift through the hundreds or thousands of flakes to locate mono or few layered materials that are not excessively damaged. Then they must analyze these flakes to find high quality samples. The automation of this process is necessary for higher throughput sample preparation. In this thesis I intend to show new techniques for automating this process, specifically in characterization of flakes and heterostructures.

These materials are often characterized using multiple microscopy and spectroscopic techniques. However, due to the high uniformity of these materials, registering the images of these microscopy methods can be difficult. To perform co-analysis, new registration techniques must be developed. By analyzing the strain and doping of

these materials, we may find key points to register images. Location of these flakes can also be problematic because of the low contrast between flake and substrate; and monolayer and multilayer. Standard machine vision techniques and convolutional neural networks can be used to assist in the identification of flakes.

1.2 Outline of Thesis

Current device fabrication techniques fail to produce devices with consistent material properties. This is due to inhomogenieties induced from transfer methods and growth conditions which lead to device to device variations that will effect the performance of two dimensional devices. New techniques must be developed to detect these variations to ensure uniform properties across all fabricated devices. In this dissertation I intend improve the knowledge of two dimensional materials research by improving in the detection of these inhomogenieties as well as develop techniques for optical characterization of these materials.

In this dissertation I intend to show new techniques for determining layer number of two dimensional materials using purely optical methods. I also intend to show new techniques for registering Raman spectral maps with images of greatly different resolution and information content using advanced Raman analysis. Finally, I intend to use multimodal analysis to improve the understanding of variations between nanoscale multilayered structures and report novel material properties that can be found in these heterostructures by beating the diffraction limit when using advanced methods of optical characterization.

Aim 1: Automatically detect monolayered materials using computer vision techniques and optical microscopy by predicting material color based on Fresnel equations.

Aim 2: Exploit the extraction of strain and doping of Raman spectra for image registration of Raman maps and other microscopy images of greatly different size and scale.

Aim 3: Report novel material properties inside multilayered materials caused by inter and intra device inhomogeneities. Determine the mechanism which cause these inhomogeneities in these heterostructures so that they may be avoided or mitigated in future fabrication efforts by using our techniques in Aim 2 to obtain sub-resolution

This dissertation begins with a literature review on the various materials I will be examining, including previous research into their electrical and properties and the devices which they are used for. Then I will discuss the methods I am using for analyzing these materials, which is primarily focused on Raman spectroscopy, atomic force microscopy and Kelvin Probe force microscopy. Finally I will discuss my three aims of using Machine vision techniques for identification of flakes and layer number estimation. Using advanced Raman analysis for image registration of Raman spectral maps, and discussing the causes of the inhomogeneities of layered materials as well as their unique properties.

Chapter 2: Literature Review

2.1   Graphene

Graphene was first isolated and characterized by Novoselov and Geim, who were awarded with the Nobel Prize in physics in the year 2010. Their work with graphene proved that atomically thin metallic films could be thermodynamically stable, which was previously thought to be impossible. They also found a way to isolate this material, through the "Scotch tape" method, or better known now as mechanical exfoliation. Their initial characterization of few layer graphene included Resistivity based on gate voltage, hall coefficient, carrier concentration and electron mobility. They found these two dimensional films to be semimetalic with an overlap between the valence and conduction bands and had electron mobilities greater than 10,000 cm^2/Vs [88].

They later went on to show that charge carriers in pristine single layer graphene behave like massless Dirac fermions opening up the field quantum electrodynamics to bench top experiments[87]. Then later characterized graphene by Raman spectroscopy, noting the differences between single layer, multilayer and bulk carbon sheets. This allowed for fast, nondestructive characterization of single layer graphene which until this point was lacking[35].

Raman spectroscopy offers fast, non-destructive characterization of the mechanical and electrical properties of a sample that is useful both in the lab and in large scale applications. Graphene's spectra is very similar to that of other carbon allotropes which have been studied rigorously, reaching back almost 50 years ago by Koenig and Tuinstra[124]. The spectra of carbon allotropes have given insight to the Raman

spectra of graphene, the primary difference is that graphite has 4 atoms per unit cell whereas single layer graphene has two as shown in fig 2.1 .
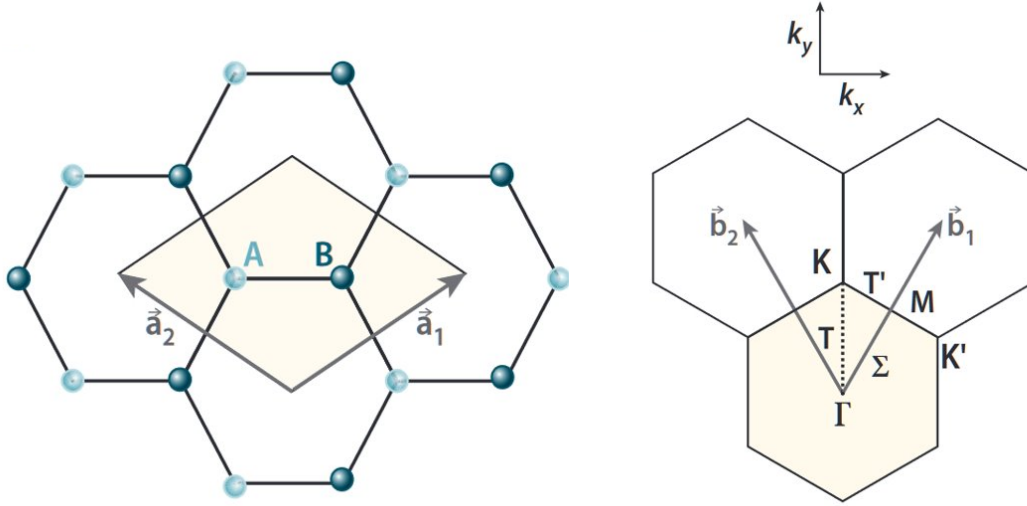
Figure 2.1. (Left) Top view of the unit cell of monolayer graphene showing the nonequivalent atoms A and B and unit vectors a_1 and a_2. (Right) The reciprocal space unit cell of graphene with high symmetry points Γ, K, K' and M points[89].

Graphite has six phonon mode branches at the Brillouin zone center Figure 2.2, three optical and three acoustic with two being doubly degenerate. These are $\Gamma = A_{2u} + B_{2g} + E_{1u} + E_{2g}$. The out of plane modes A_{2u} and B_{2g} are Raman inactive, and the E1u mode is only infrared active. There is one other normal mode, A_{1g}, at K that is Raman active, but only if a defect is present. This gives rise to the primary designations of the peaks of Raman spectroscopy. The E_{2g} phonon is attributed to the "graphite" G peak, while the A_{1g} creates the "Defect" D peak. [37] The D peak from the A_{1g} mode is doubly resonant and shifts due to excitation energy[98] by roughly $50\ cm^{-1}/eV$ and its intensity decreases with increasing excitation energy because of the Kohn anomaly at K[97]. The 2D peak is a D peak overtone caused by a double phonon process where momentum is conserved by two phonons where the two phonons

are created with opposite wave vectors. Because of this, the 2D peak does not need a defect to be Raman active. Much of the characterization below will be focused on the 2D and G peaks. There are several other peaks which include the D + D" and 2D' peaks but are much weaker than the primary G and 2D peaks. The Raman spectrum of
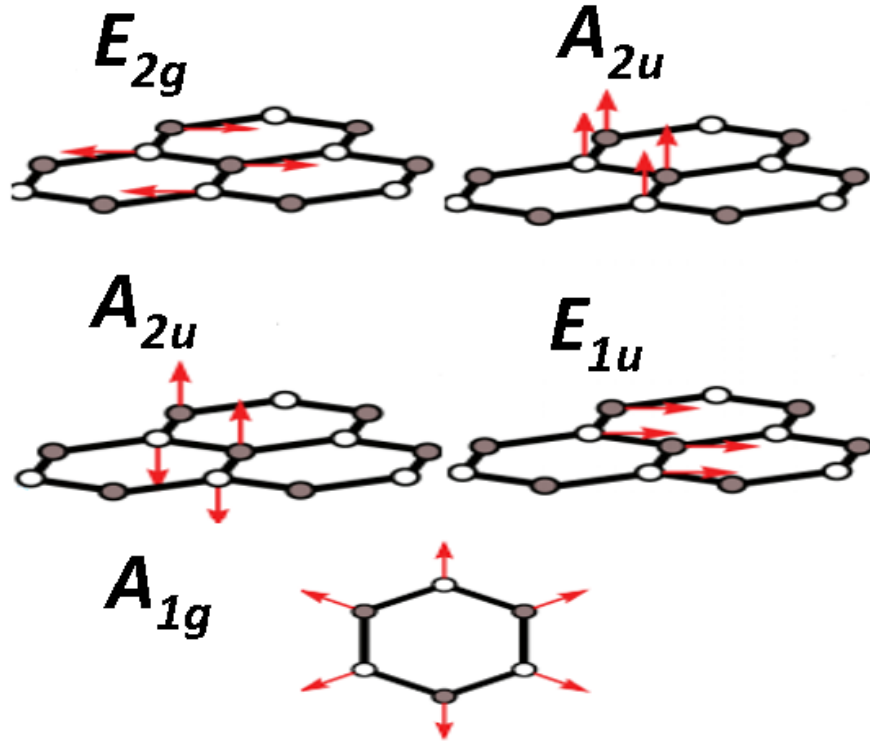
Figure 2.2. Vibrational modes of graphene. E_{2g} and E_{1u} modes are in plane vibrations. The E_{2g} mode is associated with the "Graphite" G peak in Raman spectroscopy. the A_{2u} and B_{2g} modes are out of plane and are Raman inactive. The A_{1g} mode at the K point is also Raman active and responsible for the 'Defect' D peak [87].

graphene is sensitive to several external perturbations including gate voltage, magnetic fields, strain, doping and others. This makes Raman characterization a powerful tool. When a magnetic field is applied to the graphene perpendicular to the graphene plane electron trajectories become circular, which affects the backscattering condition. Faugeras et al. shows that this causes the 2D peak to broaden and red shift. Under

large magnetic fields of >10T the electron energies are quantized into discrete Landau levels[33]. When the separation of these energy levels reaches the phonon energy level the phonons become strongly coupled. This allows Raman spectroscopy to probe electron Landau levels [3].

An edge of a graphene crystal has open bonds which make graphene edges ideal candidates for chemical functionalization. Graphene edges have different electrical properties than central graphene. A graphene edge acts as defects as they break translational symmetry of the crystal. There are two types of graphene edges, the armchair and zig-zag edges. You et al. showed that you can determine edge chirality (armchair or zig-zag) by Raman spectroscopy. The D band is shown to be stronger in armchair regions while weaker in zig-zag regions. This was done using polarized Raman spectroscopy, as the D band along the edge shows a strong polarization dependence [141]. Casiraghi et al. showed that the D to G ratio indicative of a well-ordered edge was not dependent on edge orientation. A macroscopically smooth edge was not necessarily a microscopically smooth edge [17]. These changes in the Raman spectra along the edge are caused due to the change in electron-phonon coupling and the electron-photon electron-phonon matrix responsible for the Raman process[107].

Raman spectra of graphene has been used to great affect to determine the electron doping and strain in graphene. When strain in graphene was first being discussed these two phenomena were looked at individually. But, as I discussed in my aims, this is not possible due to the bimodal sensitivity of the 2D and G peaks this is not a perfect way of determining strain and doping. Strain properties of graphene were measured by Lee et al. and found that this astounding material was the strongest material ever researched with a breaking strength of 42 N m^{-1}. This study was done by nanoindentation with an atomic force microscope [61]. These discoveries drove

an intense amount of effort into the mechanical properties of graphene and their application in electronics. Strain engineering devices were theorized where graphene's band gap could be directly controlled by "graphene origami" and straining the graphene through changes to the substrate[96] as well as stretchable electrodes [54, 64].

Characterization of strain in graphene has been done by a number of groups. Proctor et al. observed graphene on a silicon substrate under high pressure in a diamond anvil. They pressurized the substrate to 3.5 GPa and pressurized unsupported graphene up to 8 GPa. They that the G and D peak would shift to a higher wave number when pressure was applied[99]. Ni et al placed graphene on a flexible polyethylene terephthalate substrate and applied tensile strain up to 0.8% and found that the G and 2D bands shifted to lower wave numbers as much as -14.2 and 27.8 cm^{-1} per 1% strain. They calculated this strain could create a 300 meV band gap in graphene[84]. Huang et al. showed peak splitting in the G and 2D modes due to strain. This analysis shows an opening of the band gap, deformation of the Dirac cones at K and K' points, and displacement from the K point [[48, 49, 76]. In these works they also determine the Grüneisen parameters for the G peak splitting.

Mohr et al. explains the origin of the 2D peak splitting in uniaxially strained graphene. The polarization and strain direction cause different shifts in the D and 2D bands due to symmetry breaking of the hexagonal system. In high strain scenarios the 2D peak splits differently based on phonon direction, the K – M direction and the Γ – M direction[78]. A number of ab initio and TB calculations have been performed and show that under very high strain values between 16-23% a band gap could be formed by shifting the Dirac cones located at K and K'. The strain causes the Dirac cones to move toward each other and eventually merge, resulting in an opening of a realistic band gap.[27, 95, 96, 112]. Because of the linear electronic dispersion in

graphene, it is much more susceptible to changes in its carrier concentration than other semiconductors like silicon. Graphene can be doped in a variety of ways but most common is electrostatic doping. In this method source-drain electrodes are fabricated onto graphene on top of a Si/SiO_2 substrate which is used as a back gate [89, 147], or an electrolyte gel can act as a top gate[31, 114]. Because graphene is a single atomic layer it is sensitive to contact doping. Graphene can reach levels of $4x10^{12}$ cm^{-2} on SiO_2 [116]. Chemical doping is also common by adsorption of a donor or acceptor onto the graphene surface. Common dopants include nitric acid[53], ammonia[104], water[111], NO_2[108], and various metal chlorides and organics. Heteroatom doping has been used to replace a carbon with a nitrogen or boron atom, opening a band gap but also creating unwanted defects[91].

Much of the characterization was done early by Ferrari where he shows that the G peak FWHM decreases as doping increases with either holes or electrons. This is because the Fermi level shift reduces the number of electronic states available causing Pauli blocking. The G peak blue shifts with both hole and electron doping because of the electron phonon coupling is reduced due to the Fermi shift, inhibiting the Kohn anomaly at Γ [36]. The 2D band shifts primarily because of the lattice constant change. The Kohn anomaly at the K-point is unaffected because the phonons involved in the 2D band are too far away from the K point to affect the Kohn anomaly [30].

Lee et al. is the primary source of separating strain from doping. In his work he describes the trajectories of the 2D and G peaks in graphene that is strained or doped[63]. By plotting the 2D peak location against the G peak location he shows a simple vector decomposition method for the separation. This approach has been used extensively[2, 15, 38, 62, 74, 83]. The largest problem with this method is that the one must assume either uniaxial or biaxial strain. Mueller et al. introduced a method for

averaging peak splitting due to strain and decomposing any strain configuration into a hydrostatic component and a shear component[82]. Hydrostatic strain represents a uniform increase in graphene lattice. Shear strain represents a nonuniform deformation of the lattice while leaving the area of the unit cell unchanged. In this calculation the direction of doping must be know beforehand, but that is much more easily determined than the strain configuration.

For all of graphene's beneficial qualities, it lacks a band gap and interactions with it's substrate can lead to defects and unwanted doping or strain. Creating new Van der Waals heterostructures and layered materials using graphene as a base opens up opportunities for finding creating new materials that overcome the weaknesses inherent in graphene. In particular hexagonal boron nitride (h-BN) and transition metal dichalcogenides (TMDCs) have received a significant amount of attention.

Using h-BN as a substrate for graphene can offer several significant advantages compared to other substrates. h-BN has a similar lattice structure as graphene, showing only a 1.5% mismatch [134]. The different onsite energies of the B and N atoms give a large band gap of 5.97 eV. The energies of the surface optical phonon modes of h-BN are much larger than similar modes in SiO_2, giving improved high-temperature performance in h-BN/graphene devices. Banszerus et al. showed very small doping values when graphene was placed on h-BN [11]. Because of the insulating properties of h-BN, it has been incorporated into many different devices from light-emitting diodes [138], field effect transistors[105], gas sensor[139], gate dielectric and ferroelectrics [93] and many others.

2.2 Transition Metal Dichalcogenides

Transition metal dichalcogenides are a type of material that consists of a transition metal atom such as molybdenum of niobium bonded to two chalcogen atoms such as sulfur or selenium in a honeycombed layered structure. These materials have unique electronic and optical properties, including strong light-matter interactions, which make them interesting for a variety of applications. As the material is scaled down from a bulk material to a monolayer material the band gap aligns, and transfers from an indirect band gap semiconductor to a direct band gap semiconductor [90]. MoS_2 is one of the most interesting and widely researched monolayer material. This is because of its indirect bandgap of 1.2 eV to direct bandgap of 1.8 eV transition, high on/off current ratios of 10^8 at room temperature and carrier mobility of 200 cm^2/Vs [5]. Like other TMDCs, MoS_2 is a layer of molybdenum sandwiched between two layers of sulfur to form a single total layer that is 0.65 nm thick as shown in Figure 2.3. These atoms are bonded by strong covalent bonds and each layer is held together by weak an der Waals forces.

Molybdenum disulfide has a number of interesting electronic capabilities when compared to graphene. MoS_2's non zero bandgap means that it behaves as a semiconductor and it is efficient for logic and electronic devices. Short channel FETs and low power electronic devices have been created with MoS_2 due to its two dimensional structure [130]. Because of the 1.8 eV direct bandgap in MoS_2 it is an appropriate material for switchable transistor devices. A monolayer of MoS_2 was been deposited on SiO_2 substrate with a 30 nm thick layer of HfO_2 has been used to cover it that work as a top-gated dielectric layer. The device displays the current on/off ratio at room temperature 10^8 [102]. Lei Ye et al. prepared a heterojunction based on few
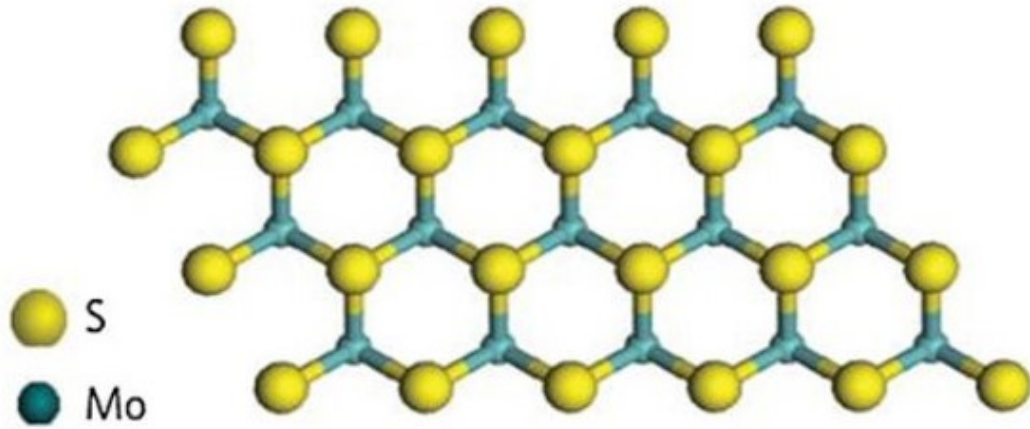
Figure 2.3. Schematic representation of MoS_2. [130]

layers of black phosphorous and molybdenum disulphide associated by Van der Waals forces for photodetector based application in visible to infrared observation range. The photoresponsivity achieved in this device 22.3 AW^{-1} observed at 532 nm wavelength and at 1.55 μm wavelength photoresponsivity has the value of 153.4 mAW^{-1} in a response time of 15 μs[140]. Tyagi et al. utilized the magnetron sputtering technique to explore the fabrication of a thin film transistor which contains crystal structure that is hexagonal vertically aligned. This thin film Transistor exhibits a high field effect Mobility of 24.1 cm^2 V^{-1} s^{-1} and contains appreciable on/off current ratio 10^6 [125].

TMDCs have also been used as biosensors which is discussed later in this dissertation. The evolution of biosensors has an important role in detecting various disease-causing factors. Biosensing has been used in some elementary ways to observe these disease-causing factors more efficiently. MoS_2 exhibits promising semiconducting properties, luminescence properties, and electrochemical properties as an excellent probe for biosensing for the observation of the number of analytes. MoS_2 quantum

14

dots exhibit a zero dimension also known as inorganic fullerenes have a size in the range of less than 10 nm[34]. FET biosensors based on MoS_2 nanosheets illustrated to observe pH, cancer biomarkers, proteins, etc. with enhanced selectivity and sensitivity. In contrast to monolayers, few layer-based on MoS_2 displays a better sensitive response[67]. Li et al. demonstrated the MoS_2 based FET sensors to detect arsenite. MoS_2 covered with an ionophore. As a result, great selectivity was accomplished. MoS_2 sensors with Ti contacts detect 0.1 ppb amount of arsenite which is twofold less than the consumption value of the world Health Organization (WHO). Various reports have been demonstrated that are based on FET based biosensors. Sarkar et al. illustrated that the detection of streptavidin (protein) with the utilization of the MoS_2-SiO_2-Si interface with the detection limit of 100 fM [106].

The phonon dispersion of MoS_2 has been theoretically and experimentally determined by a number of groups. However, only one high-symmetry direction of the Brillouin zone in MoS_2 has been access by inelastic neutron scattering [132] which has limited phonon dispersion DFT calculations. Tornatzky et. al. probed the phonon dispersion in the high-symmetry directions by inelastic x-ray scattering [123]. This study was done on 2H-MoS_2 however due to the 2D nature shown in the brilloin zone by the quadratic dispersion of the out-of-plane acoustic modes (ZA) which is characteristic of 2D materials, this phonon spectra is highly applicable to 2D MoS_2.MoS_2 has four first-order Raman active modes, at 286, 383, 408, and 32 cm^{-1} for the E_{1g}, E_{2g}',A_{1g} and E_{2g}'' respectively, with the E_{2g} and A_{1g} peaks the most pronounced.

2.3 Layered Double Hydroxides

Layered double hydroxides have sparked a significant amount of interest as electrodes for supercapacitors as they have facile tunability of their composition, structure and morphology. Electrodes with high specific capacitance is one of the keys to improve the energy density of supercapacitors. Recently, a specific capacitance over 103 F·g^{-1} has been reported for transition metal oxides/hydroxides [120]. This is due to the rich redox states, which can provide significantly improved specific capacitance compared with carbon-based materials. Layered double hydroxides (LDHs) are a class of multi-metal clay formed of brucite layers of metal cations surrounded by hydroxyls, forming a $M^{2+}(OH)_6$ octahedra. The ease of tuning of the cation layer, with the exchangeability of anions without altering the structure also give layered double hydroxides interesting electrochemical/electronic properties. layered double hydroxides are easily exfoliated into monolayer sheets making them perfect for electrode use[68]. Much research has been focused on the fabrication of layered double hydroxide devices, including core/shell nanoplatelet arrays [44, 121], carbon nanotube hybrid electrodes [22], 3D flower structures [10, 69] and flexible solar cells [40]. One interesting effect of layered double hydroxides is their "memory effect". Calcinating carbonate layered double hydroxide materials at moderately high temperatures forms layered double oxide, and rehydrating the LDH can be done to reintroduce OH^{-} as the interlayer anion[18]. This leads to structural deformations in the material by increasing the inter-layer spacing, as well as storage for OH^{-} ions which creates a self-generated electrolyte reservoir. For device fabrication, layered double hydroxide materials have been created using one-dimensional heterostructures using carbon nanotubes [149], two dimensional heterostructures using graphene [137], and 3d structures like nanoflowers

and nicklefoam [10, 69]. My research focuses on the two dimensional face-to-face structures which make full use of the large surface area of 2D substrates.

Chapter 3: Methods

3.1 Raman Spectroscopy

A photon incident on a medium results most often with the transmission and reflection of the photon. But for a small number of incident photons, scattering occurs due to in inhomogeneities inside the medium. This can be elastic scattering with no change of wavelength or non-elastic caused by atomic vibrations which produce a change in the wavelength. Raman spectroscopy is a technique which analyzes the inelastically scattered light from the sample, which is produced by the interaction of light with atomic vibrations. The Raman effect has been studied since its discovery in 1930, and today is a standard technique for analyzing crystals, pharmaceuticals, semiconductors, and many other materials. The classical description of Raman scattering in crystals considers an infinite crystalline sample. The atoms in the sample undergo quantized vibrations which are represented by phonon quasiparticles.

Unlike IR spectroscopy, which requires a change in the dipole moment, Raman spectroscopy requires a change in the polarizability of a molecule. Consider a dynamic electric field characterized by E, which is a monochromatic plane wave of frequency ω_1 and momentum k_1:

$$E(r,t) = E e^{i(k_1 \cdot r - \omega_1 t)} + E^* e^{-i(k_1 \cdot r - w_1 t)} \tag{3.1}$$

We can write the displacement of the medium as a function of position and time by a sum of random oscillations with wave vectors q and frequency ω_q as:

$$X(r,t) = \sum_q (X(q,\omega_q)e^{i(q\cdot r - w_q t)} + X^*(q,t)e^{-i(q\cdot r - w_q t)}) \tag{3.2}$$

We also consider the susceptibility tensor χ_e of the medium. We will use a Taylor series expansion and only keep the first two terms because atomic displacements are very small. Further terms in the expansion would concern a multi-phonon process.

$$\chi_e \approx \chi_{e0} + \left(\frac{\delta\chi_e}{\delta X}\right)_{X=0} X(r,t) \tag{3.3}$$

and the polarization $P(r,t)$ is:

$$P(r,t) = \epsilon_0 \chi_e(\omega_1) E(r,t) \tag{3.4}$$

The combination of the previous 4 equations leads to:

$$
\begin{aligned}
P(r,t) =& \epsilon_0 \chi_{e0} \left(E e^{i(k_1\cdot r - \omega_1 t)} + E^* e^{-i(k_1\cdot r - w_1 t)} \right) + \\
& \epsilon_0 \chi_e \left(X(q,w_q) E e^{i((k_1+q)\cdot r - (w_1+w_q)t)} + X^*(q,w_q) E^* e^{i((k_1+q)\cdot r - (w_1+w_q)t)} \right) + \\
& \epsilon_0 \chi_e \left(X(q,w_q) E e^{i((k_1-q)\cdot r - (w_1-w_q)t)} + X^*(q,w_q) E^* e^{i((k_1-q)\cdot r - (w_1-w_q)t)} \right)
\end{aligned}
\tag{3.5}
$$

This combined equation leads to three components. One term is in phase with the incoming light and represents Raleigh scattering. The other two out-of-phase components are caused by interactions with the susceptibility of the medium and represent inelastic Raman scattering. The inelastically scattered radiation has two terms, the stokes scattering with wave vector $k_1 - q$ and frequency $w_1 - w_q$; and the anti-Stokes term with wave vector $k_1 + q$ and frequency $w_1 + w_q$. In most studies

19

only the Stokes component of the spectrum is considered, the intensity of Stokes radiation is much larger than the anti-Stokes radiation and both components give similar information.

The lattice vibrations, described by $X(r,t)$ are represented by the phonon quasi-particle. But not all of these lattice vibrations can be probed by Raman scattering. The selection rules:

1. Energy Conservation:

   $$\hbar\omega_1 = \hbar\omega_s \pm \hbar\omega_q$$

2. Momentum Conversation

   $$k_1 = k_s \pm q \rightarrow 0 \le |q| \le 2|k|$$
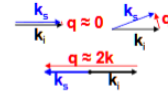
3. specific crystal symmetry considera-
   tions

The first rule, energy conservation, is self evident. The second rule, momentum conservation of maintaining $q \le k$ is shown in figure above. Because of this, single phonon processes can only occur near the Brillouin center, the Γ point. The third point concerns modes of vibration where polarizability does not change in specific crystal configurations.

These rules can be bent in a two phonon scattering process. If we were to continue on the previous Taylor expansion of the susceptibility, we would include an additional frequency component ω_1 and ω_2 for the two phonons included in this process. The momentum conservation can be maintained for $q_1 = -q_2$. In this case, there is no limit to the magnitude of possible wave vectors and phonon modes outside of the Brillouin center may participate in Raman scattering.

3.1.1 Graphene phonon dispersion

To determine the physical properties of graphene from Raman spectroscopy we need to examine the phonon dispersion of graphene. Phonon dispersion refers to the relationship between the frequency and wave vector of phonons, which are quantized lattice vibrations in a crystalline material. The phonon dispersion relation describes how the vibrational frequency of a phonon changes as the wave vector is varied. Phonon dispersion can be measured experimentally using techniques like inelastic neutron scattering or Raman spectroscopy. The phonon dispersion relation is important for understanding the thermal and mechanical properties of materials, as well as for predicting their behavior in response to external stimuli.This phonon dispersion can be calculated computationally with ab-intio density functional theory[129], or measured experimentally by X-ray scattering[77]. Both figures agree on the phonon dispersion which is shown in Figure3.1.

In graphene, the unit cell of the crystal is composed of 2 unequivalent atoms, and the phonon dispersion is made of six branches: three optical and three acoustic. For both the optical group and acoustic group, one branch corresponds to an out-of-plane vibration mode, with the other to being in-plane longitudinal or transverse modes. The optical transverse and longitudinal phonon modes near the brillouin center Γ are degenerate and correspond to the in-plane E_{2g} mode. The vibrations at the K and K' points have an A_{1g} symmetry, and is Raman active in a 2 phonon process, or a defect activated process. It is this phonon that gives rise to the G and 2D peaks.

At the Γ point the longitudinal optical phonon has a sharp kink in the phonon dispersion where the derivative is discontinuous. This phenomena is known as the Kohn anomaly and is found in the phonon dispersion of metals. There is another Kohn

anomaly in the transverse optical branch at the K point. This discovery as made by Piscance et al. [97]. The slope of this dispersion informs us on the strength of the electron phonon coupling , the slope around the Γ and K points is large, therefore the electron phonon coupling around these points is also very large.

The two main peaks in graphene are the G peak and 2D peak at approximately 1580 cm^{-1} and 2680 cm^{-1} respectively when probing with a 532 nm laser. The G band is due to a single phonon scattering event at the Γ point. The G peak excitation process is described in Figure 3.2. A photon is absorbed by the graphene, which creates an electron/hole pair and the electron resides in an unstable virtual energy state. The electron scatters a phonon which transfers energy from the electron to the phonon. Then the electron recombines and emits a photon of a lower energy. The 2D peak is a two phonon intervalley process described by Thomsen and Reich [122] where an electron-hole pair is created like in the case for the G peak, But in the case of the phonon scatters the electron from the K point to an nonequivalent K' point, and is scattered back to the original K point. This is a resonant two phonon process. The 2D band is dispersive and shifts at a rate of 100 cm^{-1} per eV of excitation energy. The 2D peak's dispersivity is due to the linearity of the band structure near the K point. This linearity leads to a large range of resonant absorption energies. A different energy of phonon is scattered at different absorption energies, and a because the phonon band is so steep in this area, a small change in excitation energy leads to a large change in the scattered phonon energy.

The identification of monolayer graphene is also important, and it is identified primarily by the 2D peak. In bilayer and multilayer graphene the band structure differs slightly. In multilayer graphene the coupling of out of plane interactions leads to four parabolic bands instead of the single linear phonon band around the K point
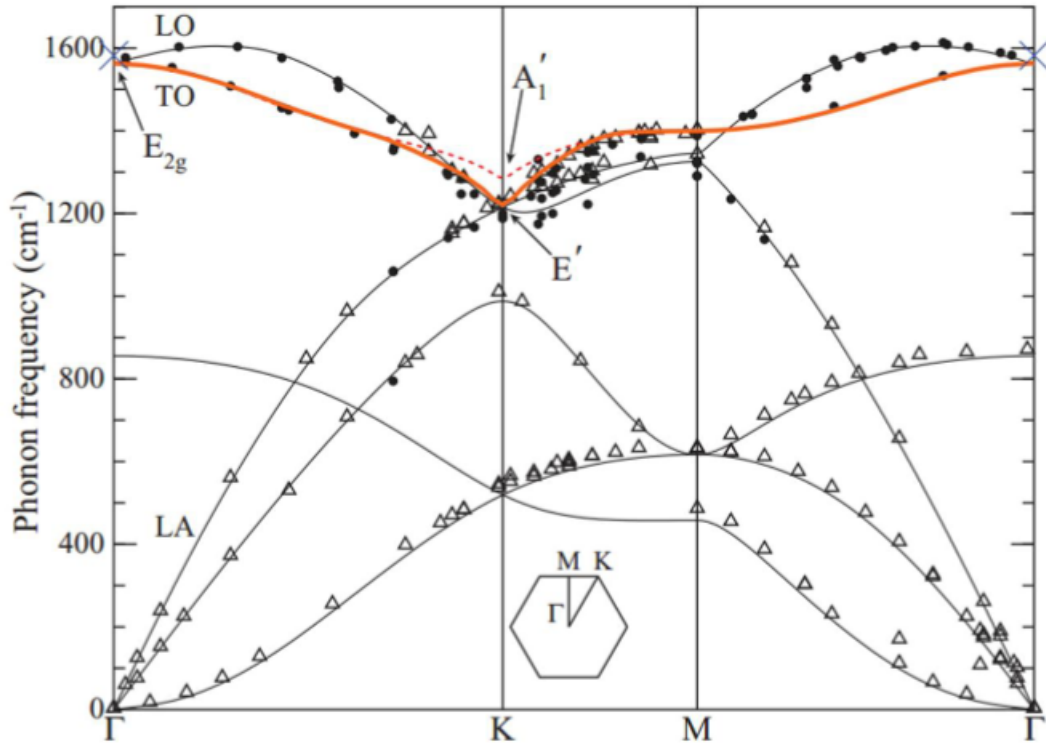
Figure 3.1. adapted from [129], Phonon dispersion of graphene. With two atoms int he unit cell, graphene has six phonon branches: three are acoustic (A), three are optical (O) phonon branches. The in-plane phonon modes are classified as longitudinal (L) or transverse (T) according to the direction of the nearest carbon–carbon atoms. Longitudinal (transverse) modes refer to vibrations parallel (perpendicular) to C–C directions. The six phonon branches are named as follows: out-of-plane acoustic (ZA) and out-of-plane optical (ZO) phonons, whereby the Z indicates that the displacement vector is along the Z axis; transverse acoustic (TA), transverse optical (TO), longitudinal acoustic (LA) and longitudinal optical (LO) phonons.
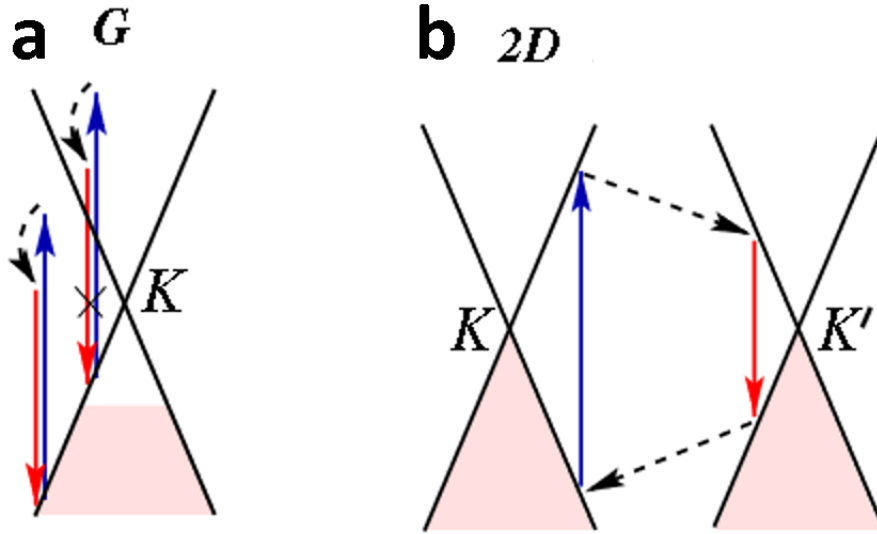
Figure 3.2. Adapted from [37], The Raman process. Electron dispersion (solid black lines), occupied states (shaded areas), photon absorption (blue lines) and emission (red lines), intraband transitions accompanied by phonon emission (dashed arrows)

in Dirac space [73]. Due to this the 2D peak is no longer a single Lorentzian peak, but is made of four closely clustered Lorentzian peaks

3.1.2   MoS$_2$and Raman spectroscopy

MoS$_2$ is in a family of TMDC's composed of two adjacent sheets of chalcogen atoms separated by a layer of transition metal atoms, therefore a monolayer of the material is a trilayer structure. A unit cell of MoS$_2$ is made up of three atoms, two sulfur and one molybdenum. It has the same reciprocal lattice as graphene, as well as the same symmetry points. In MoS$_2$ the two main bands are from the E^1 and A$_{1g}$' phonon modes. The E$_{2g}$' phonon mode is similar to the graphene's E$_{2g}$ phonon mode (G band) which is typically observed for MoS$_2$ at around 383 cm^{-1}. The A$_1$' phonon mode is an

24
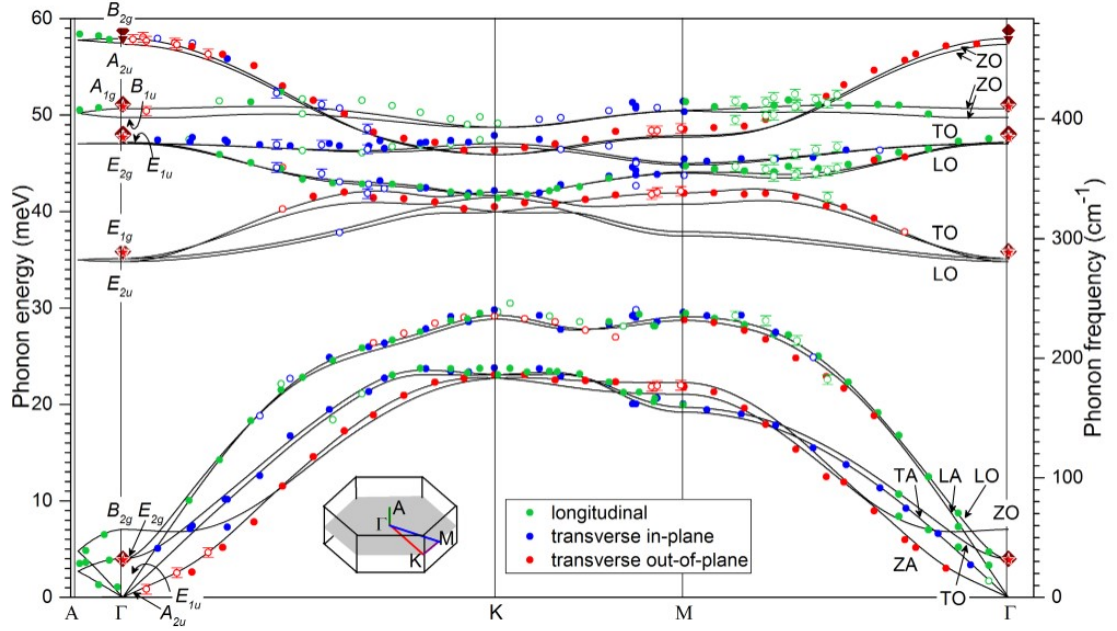
Figure 3.3. Inelastic X-ray scattering measurements and density-functional perturbation theory calculations of the phonon disperision of MoS_2 along the high-symmetry directions. Circles represent measurements probing phonons with an in-plane longitudinal (L)/ in-plane transverse(T)/ and out-of-plane transverse (Z) components. Values at the Γ point are Raman and IR spectroscopy data.[123]

out-of-plane vibration not shared by graphene which is observed in MoS_2 at 407 cm^{-1}, and the 2LA(M) mode at around 408 cm^{-1} are also commonly observed. The phonon dispersion is shown in 3.3

The Raman set up may also be used to study the photoluminescence of nanomaterials. When a material is excited by a photon of light, it can generate excitons, which can subsequently decay and emit photons through the process of luminescence. The energy and lifetime of these emitted photons can provide information about the properties of the excitons, such as their binding energy and mobility. Two dimensional MoS_2 experiences a marked increase in photoluminescence compared to its bulk counterpart. This is because the strong layer interaction between individual layers in MoS_2 which

can result in forming excitons with low binding energies and short lifetimes. These excitons are prone to dissociate before emitting a photon. Monolayer MoS_2 lacks additional layers to form strong bonds with, allowing the formation of high binding energy excitons with longer lifetimes.

Excitonic effects in MoS_2 very strongly influence the electronic properties. One of the key features of monolayer

The relative intensity of the A and B exciton peaks can be strongly influenced by external factors, such as temperature, doping, and strain. For example, at low temperatures, the A exciton peak dominates the photoluminescent spectrum, while at higher temperatures or under certain types of doping or strain, the B exciton peak may become more prominent. (Include citations and Figures, which are representing Raman and photoluminescence in MoS_2)

Trions can also affect the photoluminescence of monolayer MoS_2 in several ways. A trion is a three-particle complex formed by two electrons and one hole or two holes and one electron in a material. In monolayer MoS_2, trions can form due to the strong Coulomb interaction between the electron and hole carriers in the material. One effect is seen in the modification of the intensity of the excitonic peaks. Trions can act as a competitor for excitons in the recombination process, leading to a reduction in the intensity of the excitonic peaks. This effect is particularly pronounced at high carrier densities, where the formation of trions becomes more probable due to the higher density of carriers.

Trions can also modify the linewidth and energy position of the excitonic peaks. The presence of trions can lead to a broadening of the excitonic peaks and a shift in their energy position. This effect is due to the interaction between the trion and exciton, which modifies the binding energy of the exciton and changes the energy

required for their recombination.

3.1.3   Extracting Raman doping and Strain information

The primary information which we extract from the Raman spectral data is strain and doping information. The background signal of Raman spectra for single layer graphene was fit and subtracted using air PLS [148]. Then peaks were fit for both single layer graphene and TMDC spectra using the non-linear least-squares minimization and curve-fitting library (LMFIT) for python. Peaks were fit using Lorentzian line shapes around the D, G^+, G^-, $2D^+$ and $2D^-$ peaks, as well as around nearby shoulder peaks if they were distinguishable.

The initial separation of strain and doping is accomplished by examining the central peak position of the 2D and G line fits. These Raman frequencies are sensitive to both strain and doping because of the change in lattice constants and force fields that effect the phonon frequencies. Lee et al. created a procedure for extracting the strain and doping of graphene through the statistical analysis of the changes in the Raman frequency position [63]. By plotting the 2D and G peaks against each other we are able to see trends in the spectra which represent modulation either by strain or by doping, or both. Strain is seen in the single layer graphene Raman data as a cluster in of the 2D/G correlation plot (Figure 3.4) with a linear slope of approximately 2.2. The linear slope for p-doped single layer graphene is approximately 0.75 which is also seen in Figure 3.4. At very low values of p-doping and n-doping the dependence should be nonlinear, though, due to Fermi velocity (density of states) renormalization.

It is known that graphene on MoS_2 and SiO_2 substrate is typically p-doped. Assuming linear correlation with Raman frequencies, we can extract the relative
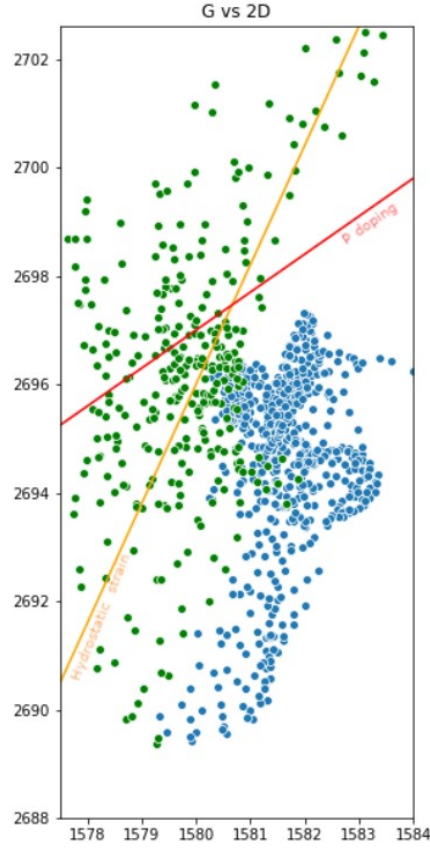
Figure 3.4. G vs 2D plot showing the split of graphene on the bare SiO$_2$ substrate (light blue) and over MoS$_2$ island (green). Red/yellow line indicates a characteristic slope for G-2D data correlation caused by pure doping/strain (isotropic biaxial).

change in strain and doping by solving the linear equation system:

$$
\begin{pmatrix} \omega_G \\ \\ \omega_{2D} \end{pmatrix} = \begin{vmatrix} a_{\varepsilon,g} & b_{\rho,g} \\ \\ a_{\varepsilon,2D} & b_{\rho,2D} \end{vmatrix} \begin{pmatrix} \varepsilon \\ \\ \rho \end{pmatrix} + \begin{pmatrix} \omega_{G_0} \\ \\ \omega_{2D_0} \end{pmatrix}
\tag{3.6}
$$

Where the vector $(\omega_{G_0}, \omega_{2D_0})$ should be calibrated against unstrained and undoped graphene reference sample, and $a_{\varepsilon,2D}/a_{\varepsilon,g} = 2.2$ and $b_{\rho,2D}/b_{\rho,G} = 0.75$ This equation gives the system of equations:

$$\omega_G = \varepsilon + \rho + \omega_{G_0} \qquad (3.7)$$

$$\omega_{2D} = 2.2\varepsilon + 0.75\rho + \omega_{2D_0} \qquad (3.8)$$

Graphene has two different polarizations of optical modes that are degenerate at zero strain. Depending on the axial direction of (uniaxial) strain, position of one of the modes shifts with respect to the other one. This generates a Raman doublet for general strain. Knowing a particular strain configuration is only possible with Raman mapping in polarized light, which resolved the polarization of a phonon mode. However, even in the case of non-polarized Raman data, position of individual components of the doublet allows to separate the isotropic and anisotropic components of the strain. The latter corresponds to the shear strain, although in order to determine specific shear direction, a polarized spectroscopy will be required, also on a calibration sample with know lattice orientation.

Mueller et al. developed a formalism to separate the doping and hydrostatic strain and shear strain components[82] . Critically, the shear strain component does not change the strain/doping correlation, that is, the slope of the curves in Figure 3.4. While the hydrostatic component does not affect the splitting of the 2D or G peaks into doublet, as it shown on Figure 3.5. The amount of the splitting allows us to determine the magnitude of the shear strain, while the magnitude of the hydrostatic strain can be determined by examining the averaged peak position (after splitting). We can then determine the magnitude of the strain components and the doping by examining the shift of the peaks in a "zero strain" case or a "zero doping" case. Parametrization follows the paper by Das et al.: in the undoped case the 2D peak shifts at a rate of 1.04 cm^{-1} per 10^{12} cm^{-2} hole density [29]. We use 2D splitting
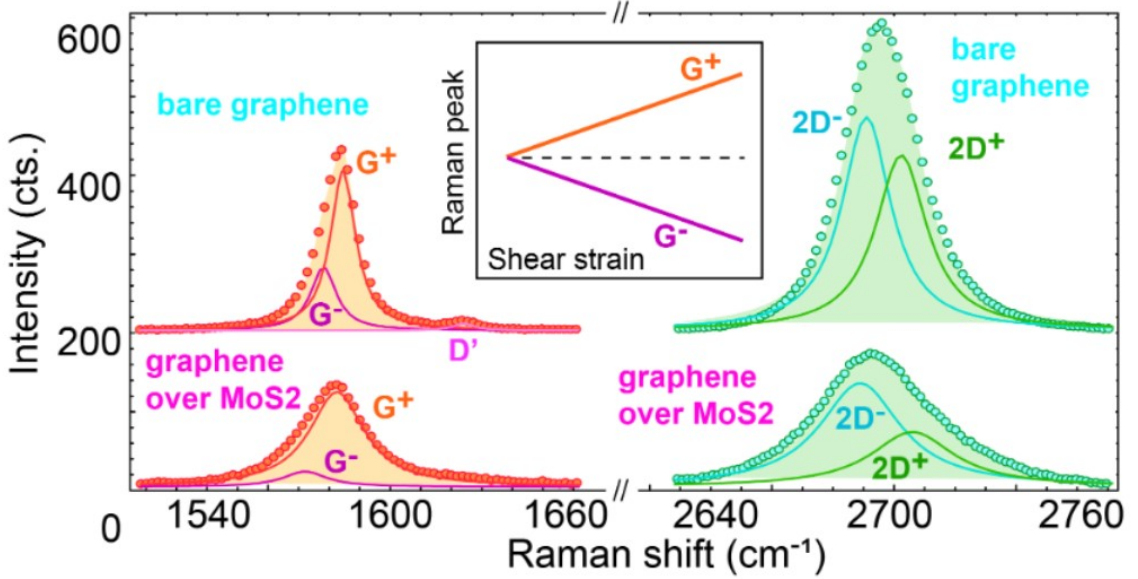
Figure 3.5. from [50]The dots and filled line represent the experimental data and the total fitted curve. The individual components of the doublet are shown with the thin lines. Additional D'-component is needed for fitting the spectrum in vicinity of the G-doublet for bare graphene. (inset) Schematics of G-line splitting with the shear strain. Hydrostatic strain, on contrary, shifts the whole doublet but does not influence the splitting.

data and the Grueneisen parameter and the shear deformation potential from [82] to determine the strain components from:

$$\omega_{2D}^{\pm} = \langle \omega_{2D} \rangle \left(-\alpha \, \varepsilon_h \pm \beta \, \varepsilon_s \right) \tag{3.9}$$

where $\alpha = 1.8$ is the Grueneisen parameter for single layer graphene, and $\beta = 0.99$ is the shear deformation potential. in figure 3.6 and 3.7 we see the fit parameters for the graphene spectra.

The strain and doping of MoS_2 can also be determined from Raman correlation data [103]. Peaks for MoS_2 were fit in the same way as the graphene peaks (Figure 3.8). For the case of MoS_2 we compare E peak and A peak that are near 382 and
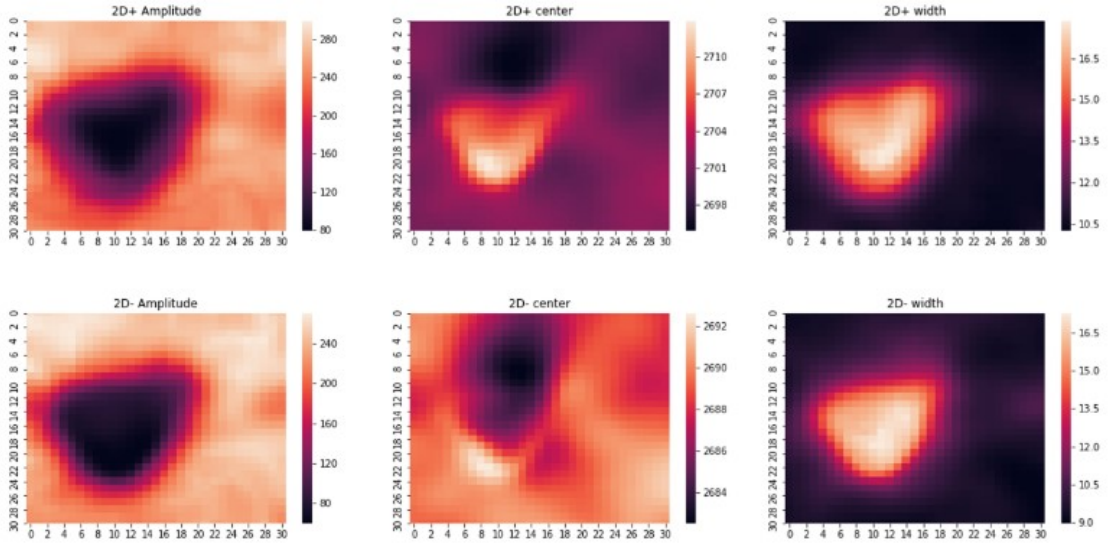
Figure 3.6. The maps showing the fitted parameters for splitting of 2D peaks.

404 cm^{-1} respectively. The E peak position is more sensitive to strain, similar to the 2D peak of single layer graphene, while the A peak position is more sensitive to doping, like the G peak of single layer graphene. The slope for strain correlation is $\sim$4; the slope for doping is $\sim$0.12. We can then use the undoped E peak position, and a Gruneisen parameter for MoS$_2$ of $\sim$0.86, to obtain the average strain. Then we examine the unstrained A peak position which shifts at a rate of 4 cm^{-1} per 1.8 10^{13} cm^{-2} [19] and determine the doping. Unlike graphene, the peak splitting in MoS$_2$ is is not discussed.

$$\omega_E = \varepsilon + \rho + \omega_{E_0} \tag{3.10}$$

$$\omega_A = 0.12\varepsilon + 0.86\rho + \omega_{A_0} \tag{3.11}$$
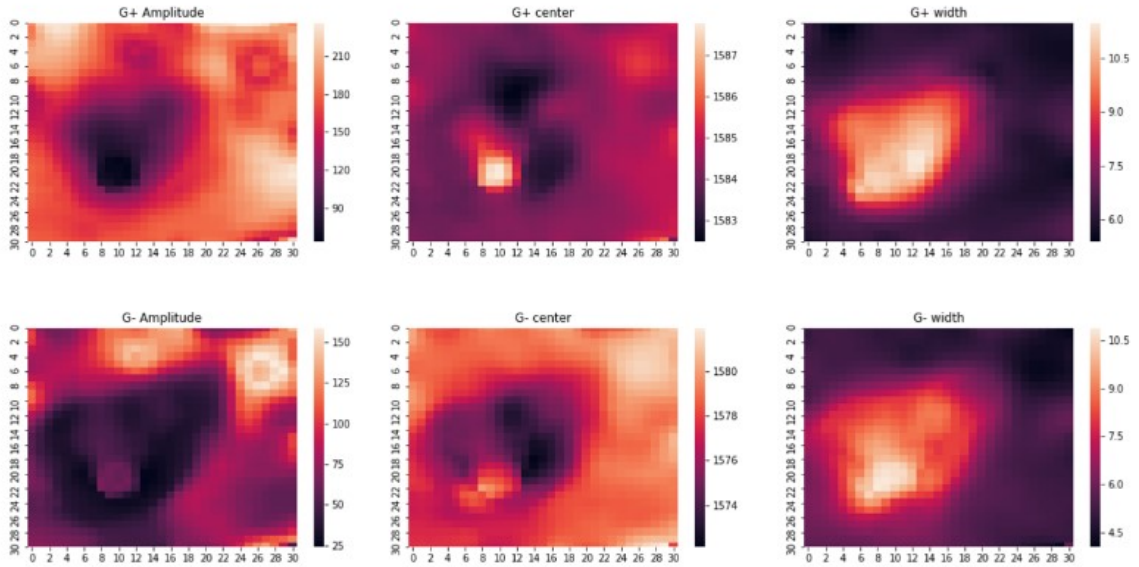
Figure 3.7. The maps showing the fitted parameters for splitting of G peaks.

3.2 Atomic Force Microscopy

Kelvin Probe Force Microscopy (KPFM) is a scanning probe microscopy technique that measures the surface potential and work function of a sample. This technique is a non-destructive, non-contact method that can be used to study the electronic properties of a wide range of materials, from semiconductors to insulators. KPFM has emerged as a powerful tool for the characterization of surface electronic properties and has been used to study a variety of systems, including thin films, surfaces, and interfaces.

The basic working principle of KPFM is based on the measurement of the electric force between a conductive probe tip and the sample surface. A conducting tip is brought close to the sample surface, and a small AC voltage is applied between the tip and the sample. The AC voltage produces an electric field that perturbs the surface
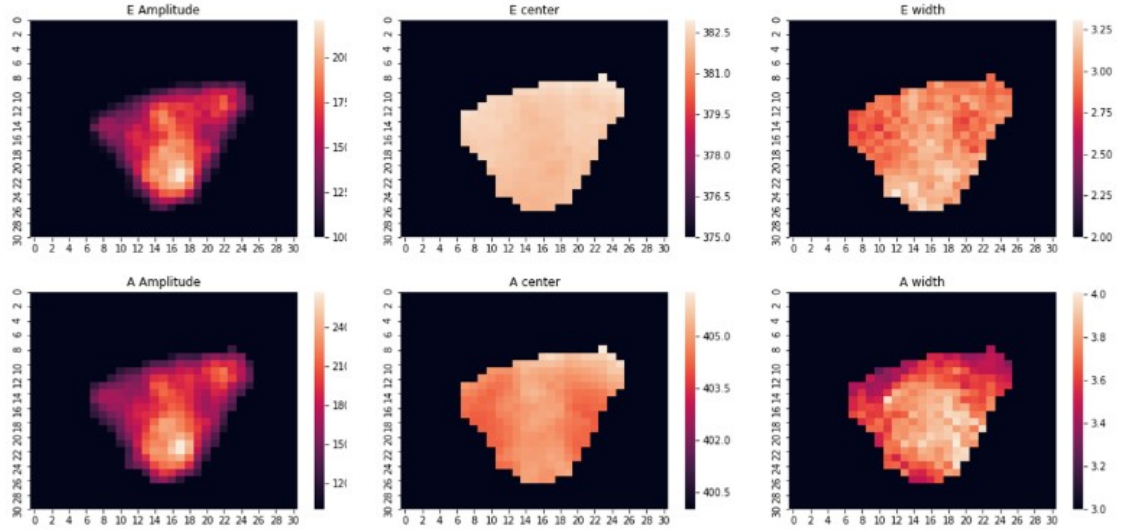
Figure 3.8. The maps showing the fitted parameters for MoS_2 peaks.

potential of the sample. The perturbation in the surface potential is detected by measuring the change in the frequency of the AC voltage applied to the probe tip.

The principle of KPFM is based on the Kelvin probe, which was first introduced by William Thomson, also known as Lord Kelvin, in 1867. The Kelvin probe is a method for measuring the work function of a material by bringing it into contact with another material of known work function. The Kelvin probe method measures the potential difference between the two materials, which is proportional to the difference in their work functions. The work function is a fundamental property of a material that determines its electronic properties, such as electron affinity and ionization potential.

KPFM is a non-contact method of measuring the work function that is based on the Kelvin probe method. In KPFM, a conductive probe tip is brought close to the sample surface, but without touching it. The tip and the sample are separated by a small gap, typically in the range of a few nanometers. The probe tip is then biased with a small AC voltage, which creates an electric field in the gap between the tip and

the sample. The electric field perturbs the surface potential of the sample, creating a small AC voltage that is detected by a lock-in amplifier.

The lock-in amplifier is used to measure the change in the frequency of the AC voltage applied to the probe tip. The frequency shift is proportional to the surface potential of the sample. By measuring the surface potential, the work function of the sample can be determined. The work function is an important parameter that characterizes the electronic properties of the material, such as its electronic band structure and its ability to form interfaces with other materials.

KPFM has several advantages over other techniques for measuring the work function, such as photoemission spectroscopy and inverse photoemission spectroscopy. KPFM is a non-destructive method that can be used to study samples in situ, under a variety of environmental conditions, such as high vacuum, ambient, or in a liquid environment. KPFM is also a high-resolution technique that can be used to study surfaces with a resolution of a few nanometers. KPFM can be used to study a wide range of materials, from metals to insulators, and it has been applied to study a variety of systems, such as thin films, surfaces, and interfaces.

The value given by the KPFM probe is the contact potential difference (CPD) which is the difference between the work function of the tip and the probed surface. given by the equation below equation, where ϕ is the work function and e is the elementary charge.

$$CPD = (\phi_{tip} - \phi_{sample})/e \qquad (3.12)$$

Prior to each set of the experiments, the ϕ_{tip} of the tip was calibrated with freshly cleaved highly oriented-pyrolytic graphite at ambient conditions. This value was used for the sample ϕ_{tip} calculations:

$$CPD = (\phi_{tip} - \phi_{HOPG})/e \qquad (3.13)$$

In fact, highly oriented pyrolytic graphite (HOPG) doesn't form interface dipoles with ambient contamination on the surface such as hydrocarbon, waters, etc., because it is chemically inactive[45]. The KPFM measurements are done in dual-pass regime: during the first pass the instrument is measuring topography of the sample surface in tapping mode, during the second pass the AFM tip is hold on distance z above the surface. To measure CPD the electrostatic field is created by applying AC voltage between tip and sample (VAC) during second pass and a lock-in amplifier tracks variations in the response amplitude. An additional DC bias (VDC) is applied to the tip, that the force is minimized when $V_{DC} = V_{CPD}$ .The electrostatic force is related to the capacitance C between AFM tip and the sample:

$$F_E = \frac{1}{2}\frac{\delta C}{\delta z}(\Delta V)^2 \qquad (3.14)$$

Here, the potential difference between the tip and the sample $\Delta V = V - V_{CPD}$. V is the sum of all externally applied voltages to the tip or sample. As a result, with both AC voltage and a constant bias, $V = V_{DC} - V_{AC} \times sin(\omega_E t)$, the resulting electrostatic force can be divided into one static and two dynamic spectral components:

$$F_{static} = \frac{1}{2}(\frac{\delta C}{\delta z}\left[(V_{DC} - V_{CPD})^2 + V_{AC}^2/2\right] \qquad (3.15)$$

$$F_{we} = \frac{\delta C}{\delta z}(V_{DC} - V_{CPD})V_{AC}sin(\omega_E t) \qquad (3.16)$$

$$F_{2we} = \frac{1}{4}\frac{\delta C}{\delta z}V_{AC}^2 cos(2\omega_e t) \qquad (3.17)$$

3.17 is the fundamental equation describing AM-KPFM: When $V_{DC} = V_{CPD}$, the amplitude of the response at the angular frequency ωE vanishes. In AM-KPFM, a feedback loop minimizes the response amplitude by adjusting V_{DC} [8].

3.2.1 Extracting Charge Density in monolayer graphene and MoS$_2$

For 2D materials with parabolic dispersion relation (with massive fermions), like MoS$_2$, the energy is given by: $E = E_c + \hbar^2 k^2/(2m^*)$. Then, the density of states (DOS) is constant for each band: $= 2m^*/(\pi\hbar^2)$. Then, the following integral gives the carrier density dependence on the Fermi level (spin and valley degeneracy included):

$$n(F) = \frac{2m^*}{\pi\hbar^2} \int_{E_c}^{\infty} \frac{dE}{1 + \exp[\frac{E-F}{kT}]}$$
$$= \frac{2m^* kT}{\pi\hbar^2} \log\left(1 + \exp\left[\frac{F - E_c}{kT}\right]\right) = N_c \log\left(1 + \exp\left[\frac{|E_c| - |F|}{kT}\right]\right)$$

where we assume that both Fermi level F and $E_c = -4.21$ eV[60] are taken with respect to the vacuum level and, thus, are negative (this definition is consistent with the definition for Dirac point E_D, conduction band edge E_c and Fermi level F. The conduction band DOS is given by:

$$N_c = \frac{2m^* kT}{\pi\hbar^2} = \frac{2m^*}{m_o} \frac{kT}{\pi a_B^2 \, E_B} \simeq 7.6 \, 10^{12} \, \text{cm}^{-2} \tag{3.18}$$

with m_o being the free electron mass, $a_B = 0.53$ Å, $E_B = 27$ eV, and effective mass in MoS$_2$ is taken to be $0.35m_o$[94].

There are two limits to be noted: for non-degenerate doping ($|F| > |E_c|$, Fermi

level lies below the bottom of CB), one can use $\log(1 + x) \sim x$ and write:

$$n \simeq N_c \exp\left[-\frac{|F| - |E_c|}{kT}\right] \qquad (3.19)$$

while in the degenerate doping limit ($|E_c| - |F| \gg kT > 0$, Fermi level is within the CB), unity is neglected compared to the large exponential, and we derive linear dependence of the charge density on the Fermi level:

$$n \simeq N_c \frac{|E_c| - |F|}{kT} \qquad (3.20)$$

Correspondingly for the monolayer graphene, which is gapless with a linear dispersion relation $E = \hbar v_F k$, we derive:

$$n_g(F) = \frac{(E_D - F)^2}{\pi \hbar^2 v_F^2} = N_g (E_D - F)^2 \qquad (3.21)$$

where the Dirac point $E_D = \chi_{SLG} \simeq -4.57$ eV[144], and Fermi velocity $v_F \simeq 1.16\,10^6$ m/s[58]. We emphasize that N_g is not a density of carriers, neither it is a 2D-DOS in a classical sense: $N_g \simeq 5.46\,10^{13}$ cm^{-2} eV^{-2}.

Since the 2D materials are electrically isolated from the Si substrate by the oxide layer, they are at floated potential and the charge transfer produces 2D charge densities $\pm e n_1$, equal (by magnitude and opposite by sign) in both layers, and generates $2\delta V$, a potential difference between TMDC and single layer graphene ($\phi(z \pm d/2) = \pm \delta V$). This potential difference is linearly proportional to the surface charge formed at each of the materials, as the result of charge transfer.

Then, the positions of the Fermi levels, both defined with respect to the higher

vacuum level in single layer graphene, are:

$$|F_g| = |F_g^{(o)}| - \Delta_F \qquad\qquad |F_{MoS_2}| = |F_{MoS_2}^{(o)}| + 2\delta V + \Delta_{FMoS_2} \qquad (3.22)$$

where the differences: $\Delta_F = F_g^{(o)} - F > 0$ is the Fermi level (up)shift in graphene, which can be measured as work function difference taken on and off the TMDC island, and Δ_{FMoS_2}, the Fermi level (down)shift in MoS_2.

Knowing the expression for TMDC and single layer graphene DOS, one can easily calculate the charge transfer and, then, the potential difference between the layers in the vertical heterostructure. Thus, the relation between the measured single layer graphene work function and the doping level of TMDC can be established, as shown in the Figure 4d of main text.

3.3   Sample Preparation

Exfoliation of layered materials, also known as mechanical cleaving, into few layers of high quality material was the first developed method of exfoliation with graphene [89]. This is a relatively easy approach for material production but comes with a number of issues such as the inability to scale, and the relatively small area one can acquire. There have been a number of other methods of exfoliation from bulk crystals of layered materials which include sonication, intercallation, ball-milling and others [72]. Chemical vapor deposition (CVD) provides a continuous sheet of layered material but some CVD grown materials only work on specific substrates. For graphene this is most often copper but also on nickel, platinum or gold [117]. The CVD grown product can be transferred to semiconducting substrates through various means discussed

below.

CVD graphene is grown through the decomposition of CH_4 gas in high temperatures (>1000 °C). Graphene has also been grown on silicon silicon carbide which creates high quality large area graphene on a semiconducting substrate. In this method, SiC substrates are annealed at high temperature (>1400 °C). The SiC decomposes into silicon and carbon. The silicon evaporates and leaves behind monolayer sp^2 hybridized carbon. However, amorphous carbon is sandwiched between the graphene and SiC substrate [85]. The limited growth substrate for graphene introduces a new challenge, transfer of the graphene onto a new target substrate. Wet chemical and dry chemical techniques have been utilized for transferring epitaxially and CVD grown graphene [126]. In the wet process, graphene transfer is directed by etching away a metal substrate with iron cloride, hydrochloric acid, or nitric acid or electrochemical bubbling based on the permeation based on permeation of H or O ions through the graphene metal interface. Dry methods use an adhesive which can pull the graphene off of its substrate and releases through heat, pressure or UV exposure[24]. We used CVD grown graphene transferred with the assistance of polymers such as PMMA to prevent the graphene from tearing . This introduces yet another problem, the contamination of the sample by transfer medium. The polymer must be cleaned through dissolution by organic solvent such as acetone. Polymer residue introduces impurities which dope the material. Numerous treatments have been proposed including annealing, plasma treatment, ozone treatment, laser cleaning, and e-beam treatment [25, 115, 118, 133]. These treatments, however, bring additional challenges. They may increase the chemical sensitivity or oxidation of the graphene surface which would lead to additional defects.

Many methods have been reported to prepare MoS_2 such as mechanical exfoliation

of bulk MoS_2, chemical exfoliation , CVD (sulfurization of Mo based compound or sulfurization of Mo and Mo based oxides), thermal decomposition of $(NH_4)_2MoS_4$ and vapor-solid growth from MoS_2 powder. Despite the great progress in preparation methods, controllable synthesis of 2D TMDCs with a uniform-large scale production remains an open question. Among all synthesis methods,the CVD one is a promising candidate for production of 2D MoS_2 films on a wafer-scale, necessary for practical applications like large scale integrated electronics[119]. In CVD process, 2D MoS_2 is grown under the flow of argon gas in a quartz tube furnace at high temperature. Molybdenum trioxide (MoO_3) is placed in a high-temperature area of the furnace (600-800 °C) and sulfur powder is put in a low- temperature area of furnace. The reaction starts while argon gas continuously flows to protect the atmosphere. After evaporation of two precursors, the sulfur vapor is driven by argon gas through molybdenum source. The reaction of sulfur and molybdenum vapor leads to grow 2D MoS_2 on a substrate, placed upside-down close by MoO_3. When the reaction is completed, argon is pumped to cool it to room temperature. The stoichiometric ratio of Molybdenum to sulfur plays a key role in the morphology and shape of 2D MoS_2: the ratio of 1:1 causes to grow the hexagon shape flakes and an uneven ratio will give rise to triangles as seen in Figure 4.13. Because some substrates of MoS_2 growth are unsuitable, it may also be transfered with many of the same drawbacks as transferring graphene.

Graphene was transferred in a number of ways throughout this dissertation. For bubble transfer, graphene (purchased form Graphenea, grown by CVD method on Cu foil) was covered by polysiloxane film. Then, it was put under pressure 1 MPa for 30 min. To delaminate graphene from the Cu foil, the electrochemical method (10V and 1A) has been applied. In this process, H2 bubbles were generated at the interface between graphene and the substrate (Cu) and caused graphene to detach from Cu.

The reduction reaction (equations shown below) of aqueous solution (NaOH) occurred according to the voltage applied between anode (Pt) and the cathode (Cu). This causes hydrogen bubbles and hydroxide ions to form at the interface between copper and graphene. To rinse the polymer film/graphene, it was transferred into DI water and left it for 10 min, this step was repeated twice. Then, the polymer film/graphene was scooped onto a clean SiO_2/Si substrate. Finally, polysiloxane film was peeled off from graphene after baking on hot plate (at 100∘C and for 30 min) (Figure.3.1).

One alternative to peeling off the graphene film was dissolution of the sacrificial PMMA polymer support via the new Soxhlet extraction method developed by Ayodele et al. [9]. The apparatus, as shown in Figure 3.9, consists of a glass chamber equipped with a siphoning tube, vapor tube, and reflux condenser. The composite sample was carefully inserted into the extraction chamber using tweezers, and reagent-grade acetone was added into the flat bottom flask placed inside a heating mantle. The solvent was heated to achieve steady boiling of the solvent (> 57 °C), allowing ultra-pure acetone to evaporate and subsequently condense and fill up the chamber containing the PMMA/graphene/SiO2 composite. The automated batch extraction process was allowed to continue for 4 h without any mechanical disturbance, after which the 2D material was removed from thimble, dried in a stream of ceN2 gas, and then stored in an air-tight sample holder.

For mechanical exfoliation, highly oriented pyrolitic graphite was cleaved using dicing tape from Ultron Systems. Repeated cleaving of a graphite flake increases the likelyhood of acquiring monolayer graphene. Graphene was then deposited manually from the tape onto a substrate or automatically using the QPRESS exfoliator module provided by Brookhaven National Labs.

For our experiments, MoS_2 was grown in accordance with [6]. High quality 2D MoS_2
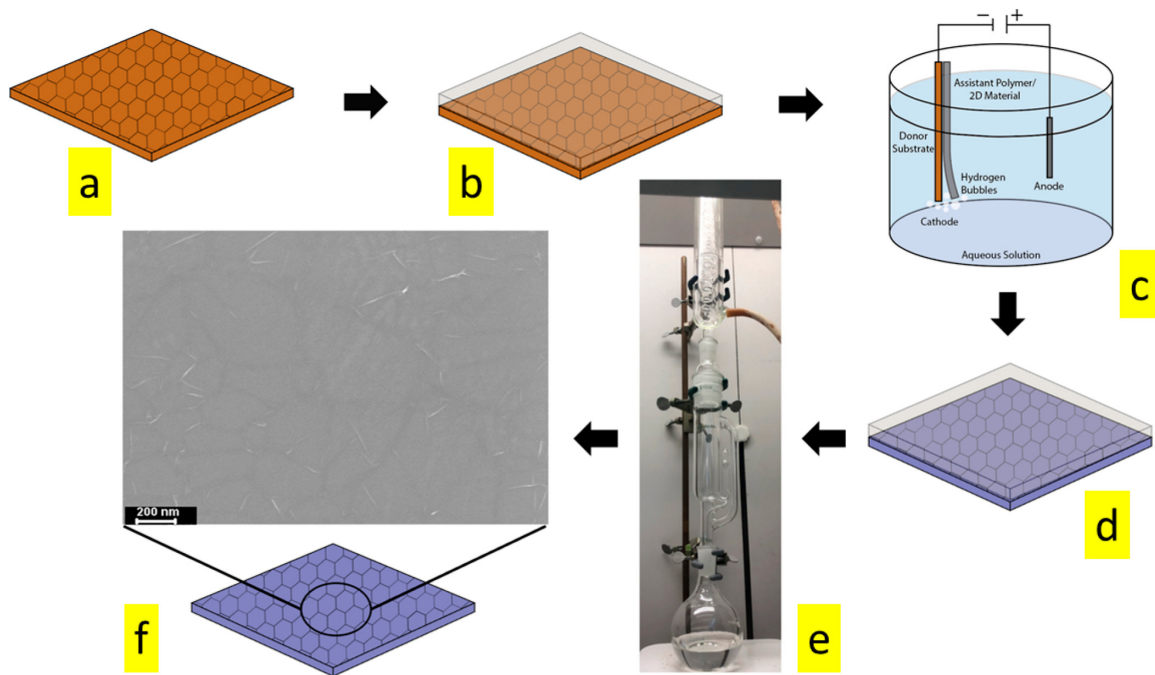
Figure 3.9. from [9], diagram of Soxhlet-assisted graphene transfer. (a) Graphene on Cu foil, (b) graphene spin-coated with PMMA, (c) Cu foil removal by the electrochemical method and subsequent transfer on the SiO2/Si substrate, (d) graphene attached on the SiO2/Si-PMMA composite, (e) Soxhlet apparatus setup for PMMA removal, and (f) ultra-clean graphene on the target substrate.

samples were grown at 650 °C on Si/SiO_2 substrates using a home-built CVD setup with a one-inch quartz tube fitted in Lindberg furnace equipment. Figure 3.10 shows that the morphology and shape of 2D MoS_2 varies depending on the stoichiometric ratio of Molybdenum to sulfur:hexagon shape flakes grow when the ratio is 1:1, an uneven ratio will give rise to triangles. The SEM and Raman analysis confirm that the majority of MoS_2 flakes are monolayers, however, some flakes, especially hexagons, have small islands of second- and third-layer.

Figure 3.10. from [6], (a and b) Helium Ion Microscopy of as-grown MoS$_2$; (c and d) SEM images of MoS$_2$ transferred to conductive substrate for CAFM characterization; Raman maps of monolayer MoS$_2$: (f) at 383 c^{-1}, and (e) at 402cm^{-1}. The scale bars in (a, d, e and f) are 5 μm and in (b) 50 μm, in (c) 500 nm

Chapter 4: Results

4.1 Nanoflake Detection
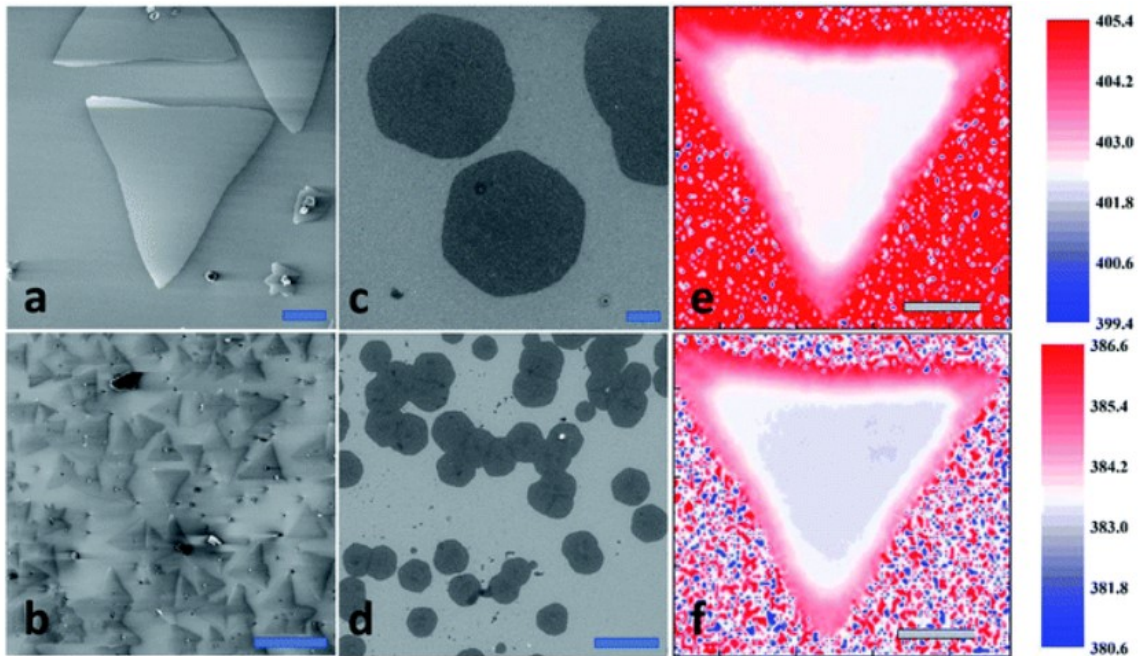
The quality of graphene and other layered materials depends highly on fabrication method. Exfoliated graphene is generally considered to be the highest quality when compared to other methods of graphene growth, mainly chemical vapor deposition (CVD) graphene and epitaxially grown graphene. This is because the graphene grown through CVD or epitaxy is not grown on a suitable substrate for most use cases. CVD graphene is grown on metallic foils, and epitaxial graphene is grown on silicon carbide which contains a buffer layer of bulk carbon. The transfer of these materials can leave induce wrinkles, tears, contamination and defects on the graphene.Many researchers have attempted to resolve this issue [9, 126]. However exfoliated graphene is still considered the highest quality material for individual flakes [131].

Exfoliated materials have a number of benefits, for small sample sizes the researcher requires almost no equipment other than tape. Samples are relatively pristine as the cleaving process exposes sheets interior sheets which have minimal exposure to the atmosphere. Layered material exfoliation is relatively fast and easy. The technician touches tape to a bulk crystal, for graphene that would be Highly oriented pyrolytic graphite which is pure and ordered graphite. The technician folds and peels the tape repeatedly to exfoliate thinner and thinner crystals of layered material before touching the tape to the final substrate. Exfoliating technique, peeling speed, angle of the peeling, and other variables can affect the yield of the layered material and most of this is guesswork by the technician. Because of this, layered material exfoliation

requires trained technicians and the process only works on small samples. Exfoliated layered materials generally can not reach sizes greater than a few hundredμm^2 and for high quality monolayered material it is much more likely to see flakes in tens of μ_2 size. These samples are much higher in quality than their CVD or epitaxial counterparts, but CVD and epitaxial graphene may be measured in areas of hundreds of cm$_2$ or more.

Automation of large area, high yield, high quality layered materials is critical to research efforts. The QPRESS team at Brookhaven National Lab have developed the first fully mechanized exfoliation platform, or "exfoliator" using pressure sensitive adhesive tape on rollers which can precisely measure pressure, temperature, speed and angle peeling in this exfoliation process. This completely removes the technician from the process. Due to this the exfoliator can create a significant amount of high and low quality samples which must be categorized.

After flakes have been exfoliated, they must be categorized as high quality or low quality. This is generally by a trained technician who inspects the flakes optically to find high quality candidates and then confirms the quality of the flakes through Raman spectroscopy or atomic force spectroscopy to identify layer count. While this is possible to do by hand it is also time consuming and prone to error.

In this section I will discuss the use of convolutional neural networks for detecting high quality samples, the potential for reinforcement learning towards finding and categorizing high quality exfoliated flakes. We use Retinanet one-stage detector which has two key advantages to standard one stage region-proposal detection networks. The first is a set of hierarchical feature pyramids that merge information from different scales. This multi-scale learning is beneficial when material flakes may be very large or very small. The second is a focal loss function, which minimizes the foreground-background

45

class imbalanced that is a common issue in single-stage detectors. Retinanet is a fast detection network that has shown strong performance in traditional computer vision benchmarks [70, 71].

In any given image of a substrate it is unlikely that there is a high quality sample of graphene. As can be seen in Figure 4.1 most individual images in a single section of the stitched image do not contain a flake, and there may be thousands of region proposals for flake detection that are easy to disprove as the target class, that class being a high quality flake. The generic loss function for region proposals is cross entropy, which is defined as:

$$CE(p, y) = \begin{cases} -log(p), & \text{if } y = 1 \\ -log(1 - p), & \text{otherwise} \end{cases} \tag{4.1}$$

in the above, $y \in \{\pm 1\}$ where y specifies the ground truth, and and $p \in \|0, 1\|$ is the model's estimated probability for the class with label y=1. We can simplify this by saying

$$p_t = \begin{cases} p, & \text{if } y = 1 \\ 1 - p, & \text{otherwise} \end{cases} \tag{4.2}$$

$$CE(p, t) = CE(p_t) = -log(p_t) \tag{4.3}$$

In training the network, loss for each region proposal is summed to define a total loss for each training example. It can be seen that if there are thousands of region proposals with only one or two positive classes the small loss from the negative classes will still be overwhelming. This has normally been addressed by adding a term α for

positive classes where $alpha \in [0, 1]$ and $1 - \alpha$ for negative classes. therefore:

$$[ht]\alpha_t = \begin{cases} \alpha, & \text{if } y = 1 \\ 1 - \alpha, & \text{otherwise} \end{cases} \tag{4.4}$$

$$CE(p_t) = -\alpha_t log(p_t) \tag{4.5}$$

however, for a very large class imbalance, this is not enough. Focal loss modifies this α term:

$$FL(p_t) = -(1 - p_t)^\gamma log(p_t) \tag{4.6}$$

where γ is a modulating factor generally between 0 and 5. $\gamma = 0$ is equivalent to Cross Entropy. as γ increases, the loss is more heavily downweighted. For our training we used a γ of one.

4.1.1 Results

We used a pretrained Retinanet framework trained on the COCO dataset, stripped the final classification layer and substituted our own class of monolayer flakes. We trained on 400 annotated images of exfoliated graphene flakes. We evaluated our model on a F_β score of $\beta = 1/2$ as we were more concerned with Recall than precision.

In training it was discovered that the neural network had a hard time distinguishing monolayer samples from bilayer samples. As it is possible to determine layer count through Raman spectroscopy, and the color difference betwee mono and bilayer is so small, this distinction wasn't made. Instead the model was trained to find few-layer

samples and ignore bulk samples. If a flake had a portion of few layer material it was considered a true positive. Figure 4.1 shows 50cm by 50cm stitched scan with a 20x magnification objective. Each blue boxed region is an individual image with potential high quality graphene. The right image in Figure 4.1 shows an individual image with a bounding box surrounding a flake. The flake on the right is a mono layer flake, while the flake on the left may contain a monolayer flake.
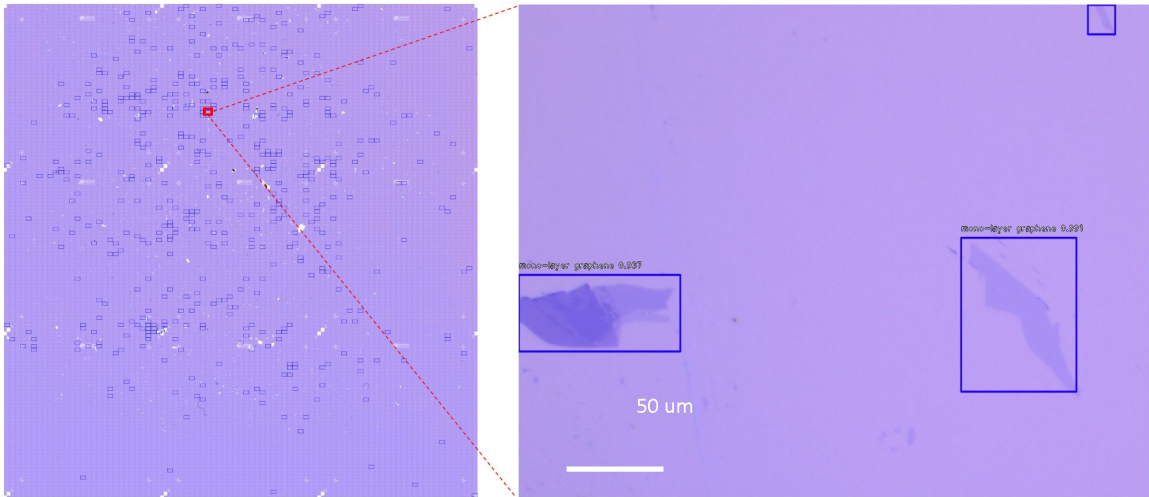
Figure 4.1. Output of the flake detection algorithm for flake detection. (Left) 5 cm by 5 cm stitched image of 4 inch SiO_2 wafer with exfoliated graphene. Graphene exfoliation includes multilayer and monolayer samples. (Right) One image of the stitched macroimage that contains three graphene flakes.

We wish to estimate the layer number of multi terraced flakes, we examine the optical characteristics of the nanomaterials. Optical contrast between the material and substrate, and different levels of the multi terraced flake originates from the integrated contrast of each wavelength component. A reflection based model based on Fresnel's law has been adopted[39]. The model tracks the reflection or transmission of a wavelength of light through the material, dielectric film and substrate. The total reflected light is a beam resulted from all the optical paths which is dependent on the

wavelength of the incident light, the incident angle, refractive indices, and thickness. For a three material system, we can estimate the reflection by:

$$R(\lambda) = \left(\frac{r_1 + r_2 e^{-2i\phi_1} + r_3 e^{-2i(\phi_1+\phi_2)} + r_1 r_2 r_3 e^{-2i\phi_2}}{1 + r_1 r_2 e^{-2i(\phi_1)} + r_1 r_3 e^{-2i(\phi_1+\phi_2)} + r_2 r_3 e^{2i(\phi_2)}} \right)^2 \tag{4.7}$$

where r is the relative index of refraction:

$$r_1 = \frac{n_0 - n_1}{n_0 + n_1}, r_2 = \frac{n_1 - n_2}{n_1 + n_2}, r_3 = \frac{n_2 - n_3}{n_2 + n_3} \tag{4.8}$$

and ϕ is the phase shift:

$$\phi_1 = \frac{2\pi h_1 n_1 cos\theta_1}{\lambda}, \phi_2 = \frac{2\pi h_2 n_2 cos\theta_2}{\lambda} \tag{4.9}$$

n_0, n_1, n_2, n_3 are the refractive indexes of air ($n_0 = 1$), 2D material, dielectric layer and silicon respectively. These are each dependent on wavelength while h_1 and h_2 are the thickness of the 2D flake and the dielectric layer. θ_1 and θ_2 are the angle, which we will approximate to be one because of the angle of illumination of the microscope. we can estimate the optimal Si/SiO$_2$ thickness for distinguishing monolayer materials by finding the largest contrast magnitude given the the above equations. We used a refractive index of 1, 2-1.1i, 1.45 and 3.88 for air, graphene, SiO$_2$ and Si respectively. For graphene layer thickness we used $33 * 35n$ where n is the number of layers. In Figure 4.2 we see the calculated contrast of graphene at various layer thicknesses and substrate thicknesses.

Unfortunately, our images have a significant vignetting effect which can be seen in Figure 4.3.Without removing this, any machine learning algorithm for clustering these materials is bound to fail. Correcting for vignetting has been applied before
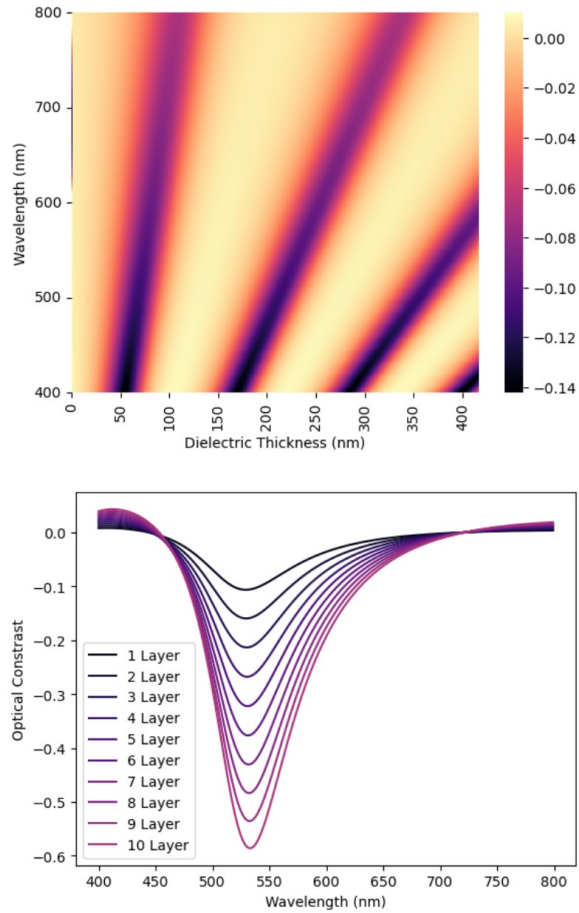
Figure 4.2. (top) Optical contrast of a monolayer layer of graphene at different wavelengths and dielectric thickness. (bottom) Optical contrast of multiple layers of graphene at various wavelengths when a 285 nm substrate is used.

using a gaussian blur and blending[66] however because we had multiple images A more accurate background could be calculated by applying a Gaussian filter to each image for each multi-image in a multi-image set, then finding the median brightness value at every pixel. This creates a vignette mask which we can invert and blend with each image individually. The blend we used was the same proposed by [66] which is a "hard light" blend, where each pixel of each RGB channel undergoes the following:
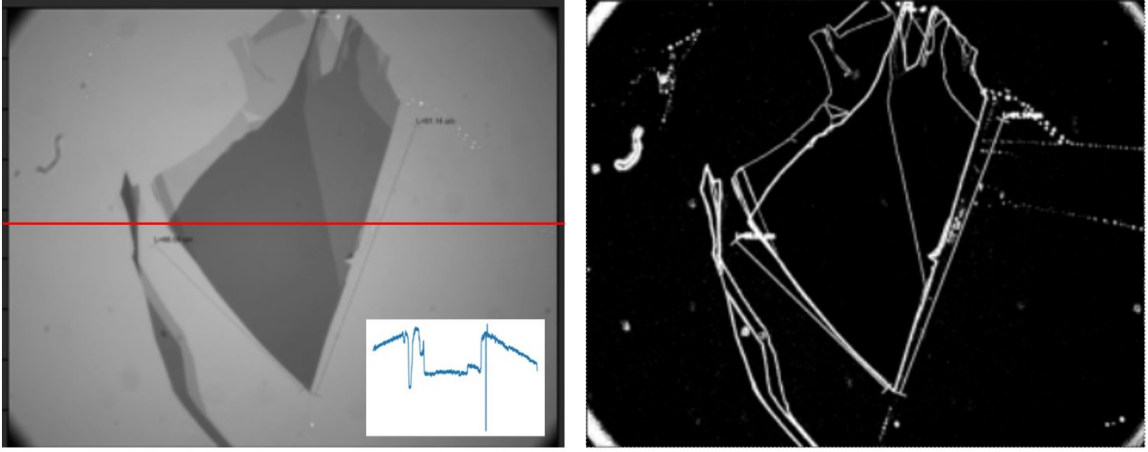
Figure 4.3. (Left) gray scale image of multi-layer graphene flake. (Left inset) intensity profile across the image. (Right) Sobel filter showing potential regions for classification.

$$f(a, b) = \begin{cases} 2ab, & \text{if } a < 0.5 \\ 1 - 2(1 - a)(1 - b), & \text{otherwise} \end{cases} \tag{4.10}$$

where a and b are pixel intensities in a given RGB channel for the image and mask respectively. This approach to background subtraction even removes some artifacts that are unique to every microscope. figure 4.4 shows this subtraction on an arbitrary image.

After correcting for vignetting effects, we may begin an unsupervised clustering to determine flake color. The apparent color and contrast of our material depends on the sensitivities of the microscope's camera. We employ a number of clustering algorithms to attempt to find the mono layer material. Some work has been done in this space [101]. However, these papers have focused on individual pixel values. Instead, we use a Sobel filter as seen in Figure 4.3. We cluster pixels inside detected edges, and normalize their color. Then we may use a single layer as a data point instead of every pixel. This allows us to work with much larger data sets in a reasonable amount of

51
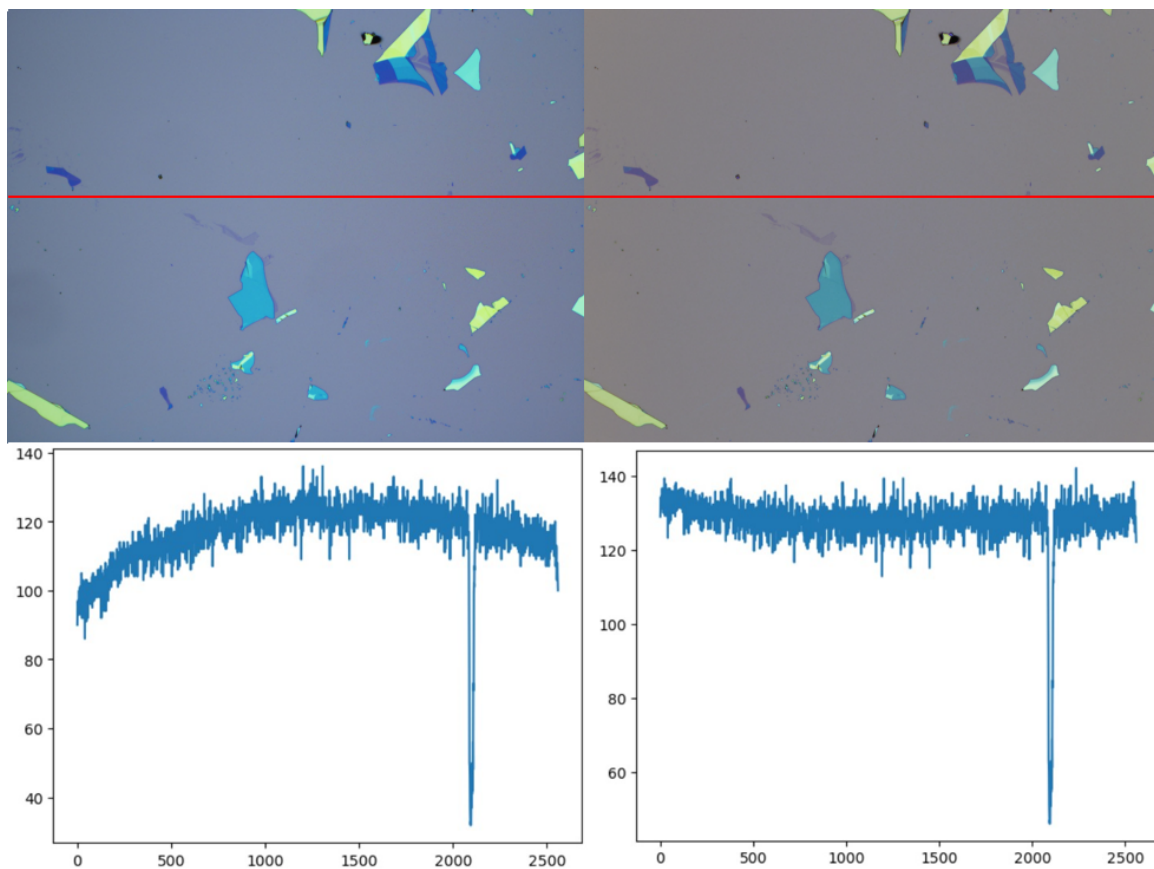
Figure 4.4. Top left) A microscope image before vingetting removal. Top Right) A microscope image after vingetting removal. Notice that this median subtraction even removes some lighting artifacts seen in the left side of the left image. Bottom left and right, gray scale intensity plots taken along the horizontal red line in the top images.

compute time. Detected monolayers are shown in figure 4.5

These values shown in Figure 4.6 are the center location of RGB values determined by K means clustering. Due to the nature of the clustering exact layer differentiation was not possible, however the clusters roughly align with color values of mono and bilayer graphene, 3-5 layer graphene and 5+ layer graphene as determined Raman spectroscopy from previously labeled flakes used to train the flake detection neural network. These clusters show a relatively linear increase in contrast from the SiO_2

Figure 4.5. (Left) Raw, unfiltered image of possible few layer graphene. (Right) Masked detection of few layer graphene.

Figure 4.6. RGB clustering using K means clustering arrived at these RGB values for few and multi-layer graphene.

substrate which is expected from Fresnel equations. Using this methodology it is possible to interpolate a linear relationship between these data points using this RGB color space for more accurate e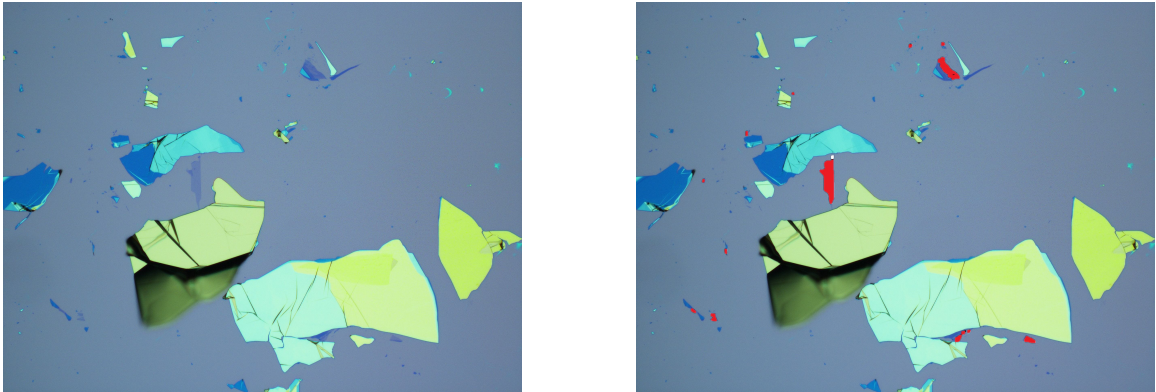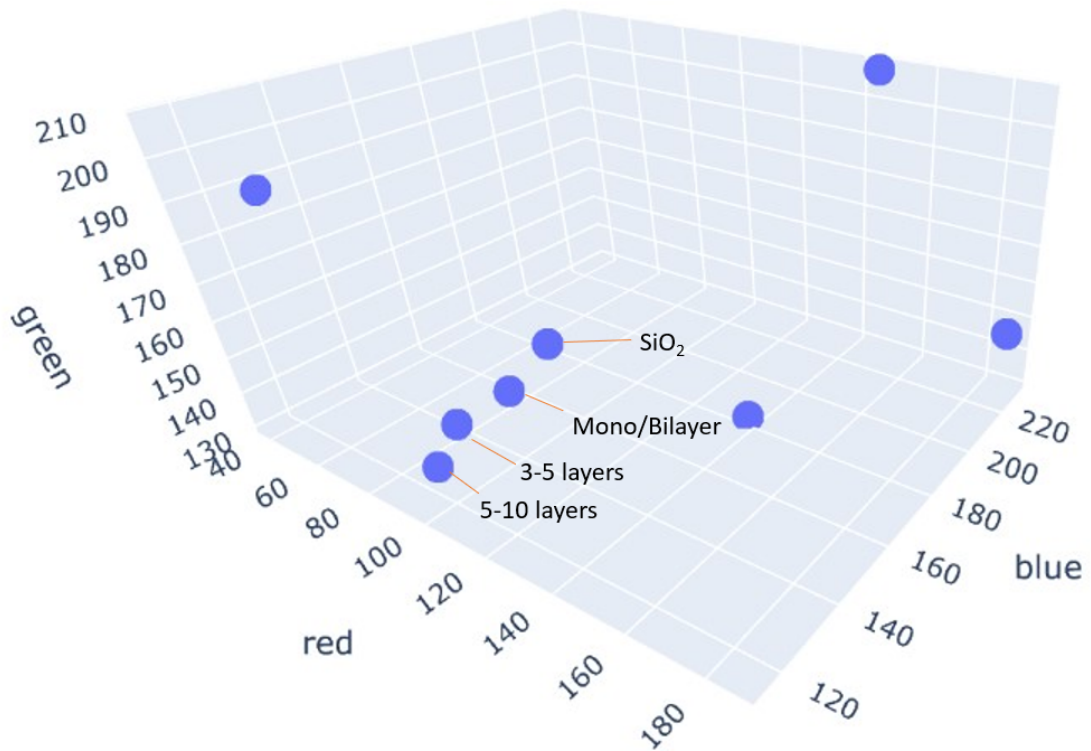stimations of layer numbers in graphene. This technique may also be used in other two dimensional materials, or the Fresnel equations may be modified for any number of heterostructures by adding additional reflection terms.

4.1.2 Summary

I have used machine vision techniques to improve the detection of few layer graphene flakes by creating a median subtraction unique to the microscope which will allow for more accurate flake detection using regional neural networks. Using the dataset generated from this flake detection algorithm I was able to generate a simple algorithm for predicting layer number of two dimensional flakes using only optical methods. I used Fresnel equations to predict the optical contrast of layered materials at specific layer counts. The relationship between layer number and contrast is linear, which allows us to predict layer count of two dimensional materials. This method will be extended to Van der Waals heterostructures to estimate layer count of individual materials inside a heterostructure in future research.

4.2 Image Colocalization/registration

Since the discovery of graphene the preparation and classification of two dimensional (2D) materials has seen large improvements[12, 41, 42, 47, 55, 65, 136]. Analysis of these materials is done on a variety of instruments that output information at different resolutions, physical scale and orientation. Correlating information between images from different instruments is a labor intensive process that involves overlaying images

and is prone to error and guess work. The issue increases when different methods do not closely resemble one another as is the case with Raman vs. electron microscopy characterization. In this work we use novel techniques to extract strain and doping information in order to find similarities between microscopic images and Raman spectral maps. This novel advanced Raman analysis allows us to correlate features in SEM and AFM images that would otherwise not be visible in the Raman spectral map.

Classification of 2D samples must be done manually by locating and characterizing these materials via Raman spectroscopy, atomic force microscopy (AFM) and scanning electron microscopy (SEM) to determine layer count and quality of these materials. This is a time intensive process that requires trained personnel. Subsequent processing includes projection of Raman maps onto AFM or SEM images to correlate data, requiring further manual alignment. This process is a good candidate to be improved by machine vision technology. Due to diffraction limited resolution Raman spectral maps are at a much lower spacial resolution and often do not show the same patterns as AFM/SEM images. We found that by analyzing the strain and doping of 2D materials these characteristic features appear in the Raman spectral images. The techniques described in this paper will allow one to correlate multimodal images containing Raman spectral maps allowing for accurate coanalysis and simplifying the task of building large libraries for machine learning approaches in the future.

Raman spectroscopy correlation of monolayered materials can be particularly difficult since these materials are often very uniform optically and microscopy images (Figure 4.7a,b) do not share features with the Raman spectral maps (Figure 4.7 c-e,h-j). While some features correspond to the wrinkles in the SEM image and AFM topography scan, no one image has enough information to correlate the Raman map

55

with either SEM or AFM image. Extracting strain and doping information from the Raman spectral data (Figure 4.7 f,g) allows us to more accurately correlate images by revealing features that are not present in other characteristic measures. Defected areas in the graphene like wrinkles and cracks often show a large shift in the strain or doping of the materials, and these wrinkles are visible in the microscopy images. The regions with large strain or doping variations appears with high contrast in the Raman spectral maps. Much research of hyperspectral image registration is done in the medical field where high resolution Raman maps of tissue samples can be overlayed with high resolution MRI or optical data. There are two primary ways to register images, feature based methods and intensity based methods. Feature based methods extract some information from the image, such as key points, edges, or corners. Researchers may implant markers in their tissue samples before beginning, giving key points to reference [80, 92] or they may use automatic identification of key points by using the SIFT or SURF algorithms [23, 142]. These detect key points such as edges and corners and register the key points between images. These methods require distinct features for the best results. Intensity based methods are most often used when key points are difficult to determine. They attempt to match pixel intensities by minimizing some metric like mutual information [56] or cross correlation [7].

In this work, data from different instrumentation are set into a similar coordinate base and resolution matched using ridge detection and Hough transformations. This study provides an excellent method for the coanalysis of Raman spectroscopy mapping, atomic force microscopy and other microscopic techniques using strain and doping analysis to register Raman spectroscopic map as key points. Sample under investigation is graphene field-effect transistor (GFET).
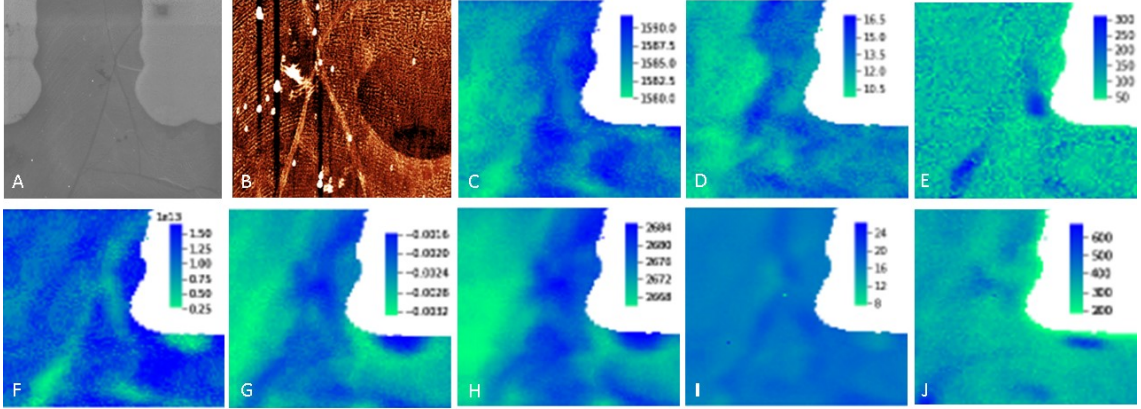
Figure 4.7. from [109] A) SEM image of GFET sample. B) $10 \times 10 \ \mu m^2$ AFM image of GFET sample. C-E) graphene G Raman peak center, width and amplitude respectively. F) graphene doping extracted from Raman Map. G) graphene strain extracted from Raman map of sample. H-J) graphene 2D Raman peak center, width and amplitude respectively. It is clear from these images that the characteristic G and 2D peaks of graphene do not give enough information to register all images. However, strain and doping maps provide enough information to register all images.

4.2.1 Strain and Doping Analysis

Strain and doping information can be extracted from Raman spectra for a number of materials including graphene [81], MoS_2 [128], WSe_2 [59] as well as other transition metal dichalcogenides [50, 51]. The process is similar for all of these materials, and follows the process put forth by Mueller et al. [81]. In monolayer graphene, strain and doping will shift the 2D and G Raman peaks linearly with increasing strain and doping. The shift of both peaks can be characterized by the ratio $\Delta\omega_{2D}^h / \Delta\omega_g^h$ and $\Delta\omega_{2D}^d / \Delta\omega_g^d$ where ω is the peak center, h is the influence due to hydrostatic strain,

and d is the influence due to doping. The vector $\vec{O} = (\omega_{2D}^0, \omega_g^0)$ represents the peak location of an unstrained and undoped spectra of monolayer graphene. The shift away from $\vec{0}$ can be represented by a linear combination of $\Delta\omega_{2D}^h/\Delta\omega_g^h$ and $\Delta\omega_{2D}^d/\Delta\omega_g^d$, whose magnitudes correspond to the magnitude of strain and doping respectively. This analysis is applicable to other materials where the Gruneisen parameter and the shear strain deformation potential is known. We used a $\vec{O} = (1583, 2678)$, $\Delta\omega_{2D}^h/\Delta\omega_g^h = 2.2$, $\Delta\omega_{2D}^d/\Delta\omega_g^d = 0.75$

4.2.2 Image Preparation

First, Raman hyperspectral maps must be converted to images that will undergo image registration. The wrinkles in 2D material create doping effects that radiates out from the wrinkle. We can detect where the wrinkle is by applying a ridge filter. This will calculate the center of the wrinkle using the eigenvalues of the Hessian matrix. Then binarize the image and remove noise by masking over areas of low strain. Images, which are all gray scale at this point, are processed using median or bilateral filtering based on image quality, resolution and contrast. For samples with good contrast and high resolution, median filtering can be applied. This technique reduces shot-noise by replacing the center pixel of the filtering kernel by the median pixel in the kernel. Due to this however, ridges can be moved a few pixels so this technique should only be used on high resolution images. If contrast or resolution is lower, bilateral filtering should be applied. Bilateral filtering applies a Gaussian filter over largely uniform areas, while preserving edges. This filtering will also reduce noise, but leave the edge positions intact. We use median filtering for AFM and SEM images, while optical images are filtered using the bilateral filter. Raman-spectra mapped images are not

Figure 4.8. from [109], Automatic Line recognition using Hough Transformation. Left Ridge filter is applied by convolving Hessian Matrix and extracting eigen values. (center) Image erosion to remove noise. (right) example of a simple Hough Transformation from 2 lines to two points.

filtered due to their low resolution.

Binary images must be created after the filtering, as shown in Figure 4.8 Each image has a ridge filter applied by analyzing the Hessian matrix. The maxima of this matrix represents the center of ridges. Thresholding is then applied, creating a binary image where white pixels represent the wrinkles in the graphene. A series of opening and closing morphological operations can be used to smooth the edges.

A Hough transformation is applied to the binarized images to transform our ridge pixel coordinates into parameter space[32] of $x\sin(\theta) + y\cos(\theta) = R(\theta)$. The pixel coordinates are transformed to sinusoidal functions and plotted on a 2D histogram. The largest bins are along the intersections of these functions. The location of the largest bin describes the equation of a line corresponding to a ridge. By selecting a number of the largest bins we extract the longest strait wrinkles in the pictures. These maxima may be used as key points for our transformation. The selection of these key points is critical to successfully aligning images. Wrinkles must be long enough to appear in the Hough transformation, and should be straight.

4.2.3 Registration

In order to register images extrinsic or intrinsic information is required. Extrinsic information requires the use of markings placed on the substrate which adds time, complexity and cost to a project. Intrinsic information would take the form of information inside of the image which we can use to link images such as key points from edges and corners, or intensity from hyperspectral information. Mutual Information is a intensity metric of two images which is maximized to register two images. This is often the preferred method of image registration in most applications where the images are of similar scale, and the images may contain similar information. However because these hyperspectral images are often very different in resolution and information, Mutual Information maximization is not a good candidate for registration. Raman spectral maps of heterostructures at the small scale often have large intensity shifts over micron distances which do not appear in microscopy images. This makes intensity based matching problematic. Key point identification is the method we wish to pursue.

Because 2D materials are nearly uniform over their surface it can be difficult to register two images. If a given sample was perfectly uniform over the entire image area, it would be impossible to register. However, most two dimensional materials are non-uniform at the smallest scales where we can detect wrinkles, tears and defects in the materials. These small defects show brightly in the hyperspectral Raman images after strain and doping is extracted. Two dimensional materials that are folded or wrinkled show large strain or doping variations around these defects, and these defects can be used for image registration. We can find the maxima of this strain variation in the Raman spectral map and use these as 'edges' for keypoint matching. In Figure 4.9 a and b, wrinkles can be seen in the SEM and AFM images. These wrinkles align well

with the doping maxima in Figure 4.9 c. Figure 4.9 d includes all three characterization methods registered. We can transform the spacial coordinates of the wrinkles and strain into Hough space. The units of Hough space are r and theta, and every point in Hough space describes a line in real space with the equation $x\sin(\theta) + y\cos(\theta) = R(\theta)$. A two dimensional histogram is generated by the sinusoids in Hough space. The largest bin in this histogram describes a line in real space. Because of our preprocessing this line will match strait sections in the wrinkles of our two dimensional materials.
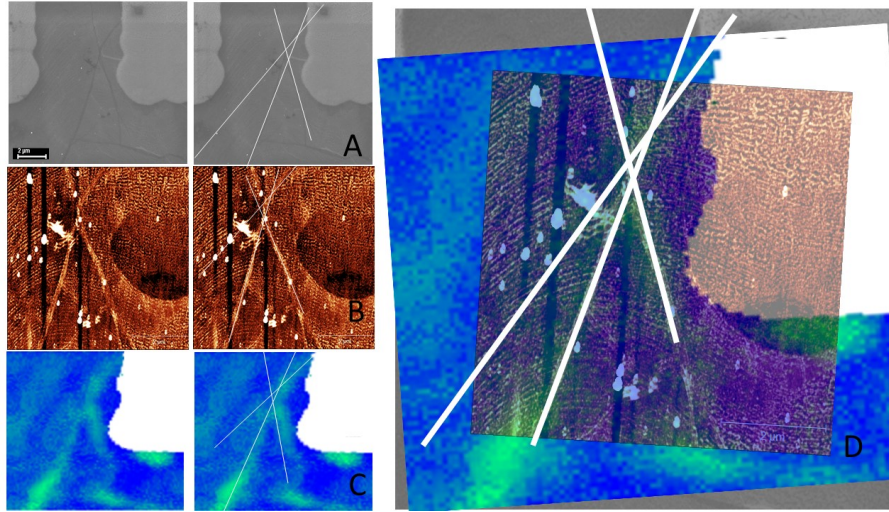
Figure 4.9. from [109] A) SEM image with detected wrinkles on right. B) Raman image, with detected lines on right C) AFM image, with detected lines on right. D) Aligned images by Hough transform.

4.2.4 Alignment

Using the spacial coordinates of wrinkles, we can determine rotation of the images by following the procedure presented by Chitsobhuk et al[26]. Rotation of an image in Hough space is represented by a shift along the X axis. By aligning our key points vertically we determine the rotation of the image. We can also use phase correlation

to determine the translation. By transforming the spacial coordinates by a discrete Fourier transform we determine translation by:

$$f_2(x, y) = f_1(x - t_x, y - t_y) \tag{4.11}$$

$$F_2(\psi, \nu) = e^{i2\pi(\psi t_x + \nu t_y)} F_1(\psi, \nu) \tag{4.12}$$

where f_1 and f_2 are signals related by a translation (t_x and t_y), (F_1 and F_2 are their Fourier transformations, the transformations will have the same intensity but will be shifted by the phase $e^{i2\pi(\psi t_x + \nu t_y)}$

We also attempted SIFT and SURF based registration of our images by registering the doping map with the AFM and SEM images. In the AFM and SEM images, many key points could be detected, and the AFM and SEM images could be registered. However, due to the low resolution of our Raman maps, few keypoints were detected. corners and T junctions are difficult to distinguish in these low resolution areas and fine detail is lost. Matching key points between the images may have been possible with fine parameter tuning, but we could not accomplish it with our samples.

4.2.5 Sample Preparation

The GFET-S10 was acquired from Graphenea. SEM paramaters for image acquisition of GFET include an accelerating voltage of 3.0 kV and a working depth of 3.4 mm. The equipment used in the experiment include Horiba Raman Confocal Microscope with 532 nm Laser excitation, Zeiss Auriga FIBFESEM, and Asylum MFP-3D Origin+ AFM. This method requires two criteria to be met in order to perform alignment. Crystal edges must be distinguishable and images must be roughly the same size and

scale. Raman features must be fit and converted into an image prior to alignment.

Samples analyzed with Raman Spectroscopy are fit by Lorentzian function using the non-linear least-squares minimization curve-fitting python library (LMFIT). For graphene flakes these include D, G, and 2D peaks at $\sim$1350 cm^{-1}, $\sim$1580 cm^{-1} and $\sim$2690 cm^{-1} respectively.

4.2.6 Summary

In this work I show new techniques for Raman Image registration using advanced strain and doping analysis of the Raman signal of monolayer graphene. Registering hyperspectral images of 2D materials is particularly difficult due to the lack of keypoints on un-patterned substrates. The strain/doping maps can assist by creating these keypoints. Registration of these images allow for multimodal analysis from these various instruments by aligning multiple images into a single coordinate space. This is done by Hough transformations and arbitrary resolution definitions to generate a new coordinate frame where spatial information may be preserved and correlated on a pixel by pixel basis. With this method, a Raman map of graphene has been registered with SEM and AFM images after extracting strain and doping information from the Raman spectroscopic map. This technique can also be applied to other two dimensional materials where strain and doping information can be extracted, such as MoS_2 [128], WS_2 [59], and other transition metal dichalcogenides [51]. The ability to register and correlate Raman spectral maps with other microscopy methods will be useful to both researchers and industry for device fabrication.

4.3 Multimodal Analysis of Graphene in bilayer and heteromaterial structures

In nano-scale devices, small deformities in the materials can lead to drastic differences in the electrical and optical properties of these devices. These deformities may come from strain induced in the material, contamination, or crystal lattice mismatch. In this section I intend to show a number of intra-device inhomogeneities which effect the electrical and optical characteristics of potential Van der Waals structures. I have discovered a number of unique properties emergent from these structures and will discuss the causes of these below. I show 5 different two dimensional materials and Van der Waals structures each with unique properties below. Graphene Bilayers which exibit lattice mismatching detected via Raman spectroscopy and confirmed with scanning nearfield optical microscopy. Graphene niobium diselenide heterostructures with large strain mismatch on the niobium crystal. Graphene MoS_2 heterostructures that show doping dependent photoluminescence and charge transfer variations between the graphene and MoS_2 layers. And Graphene Layered Double Hydroxide heterostructures which show incredibly high graphene strain and unexpected doping effects.

4.3.1 Improved Graphene Monolayer Transfer

As previously discussed in this dissertation, transfer methods can leave residue and introduce defects into the monolayer material. Polymer residue can significantly influence the charge carrier density and mobility of graphene [14, 100]. In my lab a polymer blend of polyfuranone chain products (PCP) derived from angelica lactone and polymethylmethacrylate (PMMA) was used to transfer graphene via wet chemistry
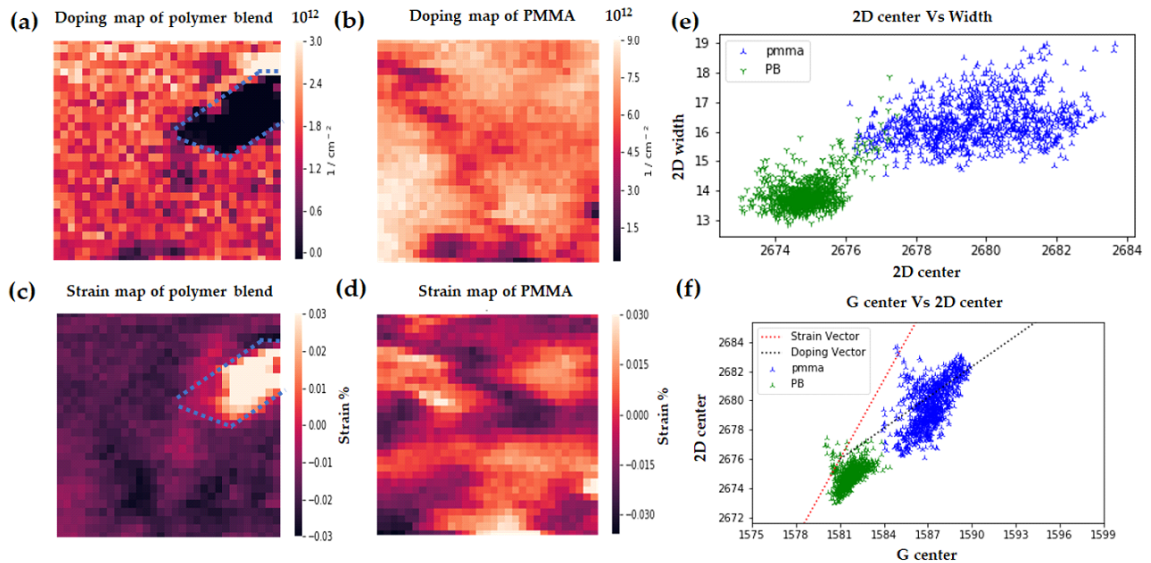
Figure 4.10. from[9] Analysis of the purity of graphene using mixed polymer transfer method. a) doping map of graphene transferred by polymer blend method. Blue dotted region is few layer graphene. b) doping map of graphene transferred by PMMA method. c) strain map of graphene transferred by polymer blend method. Blue dotted region is few layer graphene d) strain map of graphene transferred by PMMA method. e) 2D center vs 2D width. f) 2D center vs G center.

and below we show a reduced polymer residue with this polymer blend (PB).

The Raman spectra was fit using Lorentzian peaks for the 2D, G, and D peaks. We observed a uniform doping in PB-transferred sample which is in contrast with PMMA where a larger doping variance was obtained. The PB sample has an area of few layer graphene, which has been removed as outliers from the scatter plots (green hexagon shapes in Figure 4.10 a,c. Likewise, in Figure 4.10 b,d, we see that there are areas of comparatively high strain and low strain in both samples but the PB sample has more uniform strain. From the correlation plot, we clearly observed that the PMMA-transferred sample has a wider 2D peak, and a significant shift in both the G and 2D peak when compared with PB sample (Figure 4.10 e). In Figure 4.10 f, we plot the G peak vs the 2D peak of both samples. Using vector decomposition, we obtained

the amount of strain and doping that causes peak shift as previously discussed in this dissertation. Points on the plot which lie at the intersection of the two lines would have zero strain and zero doping. As strain is introduced to the sample, the peak locations will shift along the red curve, with both G and 2D peaks shifting to a lower wave number for tensile strain and shifting to a higher wave number for compressive strain. Higher p-doping values will shift the peak along the magenta curve away from the intersection. We expect our sample to be p-doped and so n-doping is ignored. The correlation map of the Raman G and 2D peaks shows that the PB-transferred graphene has less variation in both strain and doping and is closer to Dirac point than the PMMA-assisted transfer. From the Raman spectra characterizations, the PB transfer method shows more uniform, high-quality graphene than the PMMA transfer method.

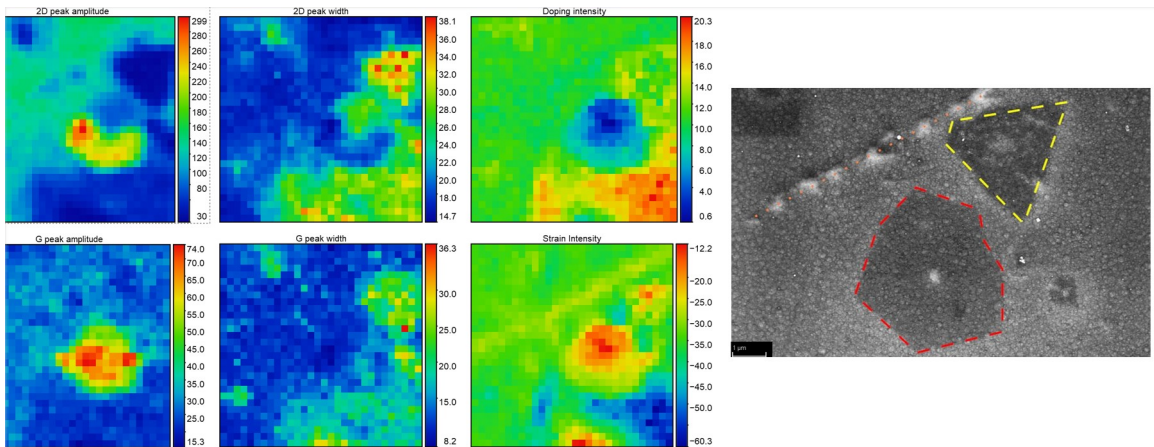### 4.3.2   Graphene Bilayers

Figure 4.11. The red dashed lines surround an island of multilayer graphene. At the center of this location we see a pillar of Molybdenum Oxide. We can see Raman spectral maps of this region showing multiple different strain and doping regions on this multilayered graphene.

The unique properties of stacked layered materials cause nano-scale variations in strain and charge transfer due to lattice mismatch and work function differences. These variations lead to signal distortion when using 2D materials as devices. In this chapter we attempt to categorize some of variables and quantify them. Figure 4.11 and Figure 4.12 show a graphene bilayer (outlined by red dashes in Figure 4.11) suspended by a MoO post. What appears to be a uniform bilayer graphene crystal on the scanning electron microscope shows significant variation of the Raman signal. In the Raman spectra of Figure 4.11, the bottom of the graphene bilayer shows an increase in 2D and G peak amplitude, and a sharpening of both peaks as well. near the top of the bilayer is a separate region where the material is significantly doped and strained. We can analyze Figure 4.12 to understand why. In this figure, the graphene was analyzed with Kelvin probe force microscopy and scanning nearfield optical microscopy. The KPFM shows an increase in the CPD along the top of the material, indicating an increase in the work function of the material. The bottom image shows the first and second harmonic of the sSNOM device. The left and right show two distinct regions where the local density of states is radically different from one another. The darker region in the sSNOM image correlates with the reduced doping region in the Raman map, and a higher work function in the Kelvin Force Probe image. This is caused by two separate twist angles between the graphene layers. When first grown, the bilayer graphene grew from two different seed crystals, which spread to merge into a single area of bilayer graphene .The sSNOM image shows qualitative differences in the local density of states of the two regions of this bilayer graphene area. The change in magnitude of this density of states implies the brighter region has a 30 degree relative twist angle[127]. Using the registration techniques I discussed in Aim 2, we correlate Raman spectral data with sSNOM and KPFM results. We see that this twist angle

67

reduces P doping of the bilayer, as well as greatly increases strain. We expect that the bright region of the sSNOM image has the larger twist angle compared to the dimmer region which has a small twist angle corresponding to A-B stacked graphene. This 30 degree twist would cause a lattice mismatch and would account for the greatly increased strain. We intend use this information in future work to more accurately determine doping values for bilayer graphene at various twist angles. The 2D peak in bilayer graphene splits to 4 separate peaks due to the degenerate nature of the peak, and it is not clear the best way of extracting strain and doping information from these bilayer peaks.
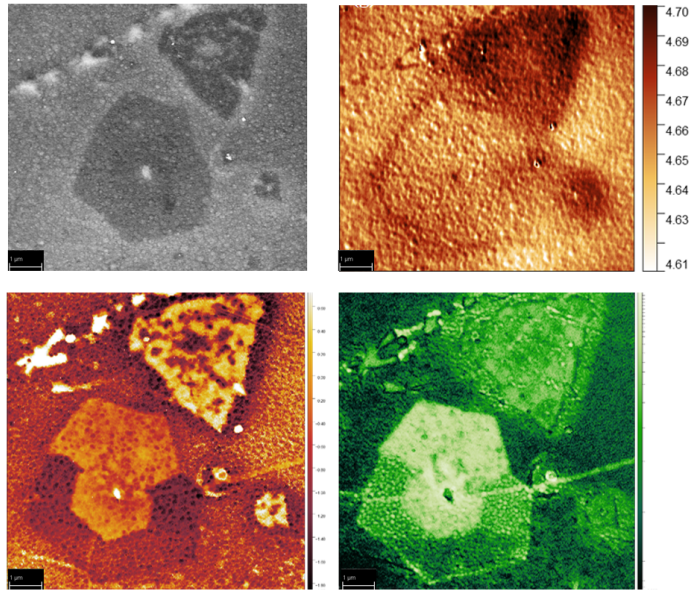
Figure 4.12. (Top Left) SEM image of Bilayer graphene. (Top Right) KPFM image of bilayer graphene. The KPFM image shows a 2meV difference between the top of the bilayer and the bottom of the bilayer. (Bottom Left and Right) SNOM images showing First harmonic (Left) and second harmonic (Right). The darker regions indicate a lower local density of state.

In Figure 4.13 we see another bilayer graphene region covering small MoS_2 flakes. this bilayer area is lifted slightly off of the substrate by MoO posts marked by stars.
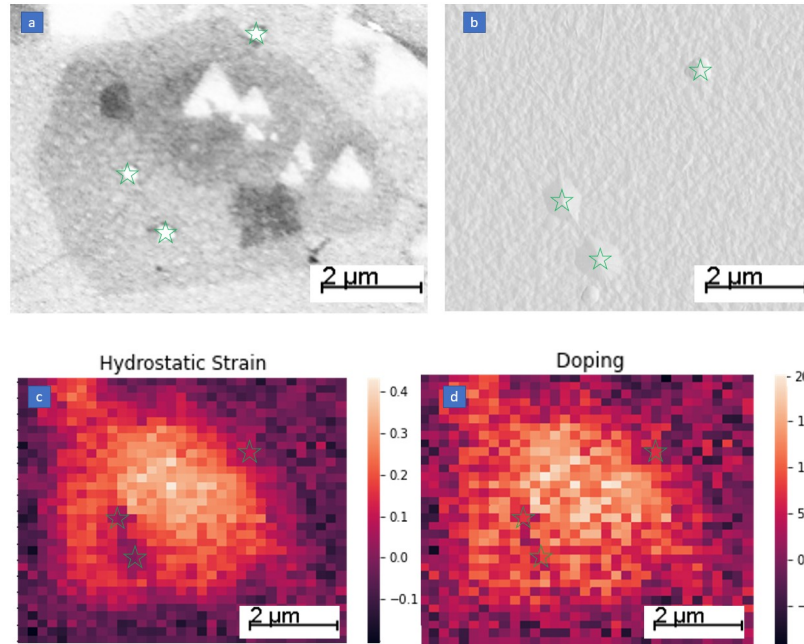
Figure 4.13. (a) Scanning electron microscope image of a bilayer region of graphene covering MoS_2 crystals. (b) Atomic Force Microscope topography map showing graphene forming a tent on top of MoO posts. (c) Hydrostatic strain of the graphene. (d) doping of the bilayer graphene. Magnitudes of the shear strain in bilayer graphene is not well defined.

The Raman signal of this material shows significant strain and doping across the bilayer area, however there is a reduction of strain around these posts, caused by lifting the graphene off of the substrate. The MoS_2 crystals underneath do not appear to affect the bilayer graphene. By lifting the graphene off of the substrate we are applying a strain to the material. With this suspended graphene we should expect to have less doping due to interactions with the substrate. In future work, we will use this information to more accurately characterize the Raman signal of bilayer graphene.

4.3.3 Graphene / NbSe$_2$ heterostructure

With the registration techniques discussed in Aim 2, we are able to correlate Raman spectral data of NbSe$_2$ with KPFM imformation. Figure 4.14-4.17 show analysis of monolayer graphene on top of NbSe$_2$ flakes. Raman spectroscopy shows significant variation in the spectra of graphene on top of this crystal, while this difference is not reflected in in the Kelvin Probe Force Microscopy. The graphene on top of NbSe$_2$ shows an increased work function between 3 to 4 meV. However, the 2D and D center positions are red shifted on the majority of the flakes, representing a tensile strain, but towards the top of the crystal there is a blue shift representing a compressing strain. The blue shifted area also has a significantly higher magnitude. This differential in strain is incredibly high, up to 10% compared to previous results. This differential in shear strain is close to opening a band gap in the graphene, where a shear strain of 14% may open a bandgap. This discovery could lead to simplified fabrication of non-zero bandgap graphene devices due to the simplicity of this graphene NbSe$_2$ heterostructure.

Figure 4.14. NbSe$_2$ flakes on SiO$_2$ covered by graphene.

4.3.4 Grapene / Layered Double Hydroxide heterostructure

Mg/Al Layered double hydroxide flakes were deposited onto SiO$_2$ substrates shown in 4.18. The layered double hydroxide flakes are reported to have Raman active signatures however they were incredibly faint and we were unable to resolve the Raman spectra of our layered double hydroxide material [57]. The Mg/Al layered double hydroxide material we fabricated is reported to be positively charged[68]. However, in our study of the material using Raman spectroscopy of the heterostructure which is shown in 4.19, we find that the graphene Raman signature shows significant N doping compared to the substrate where the graphene is P doped by the SiO$_2$. This implies that the
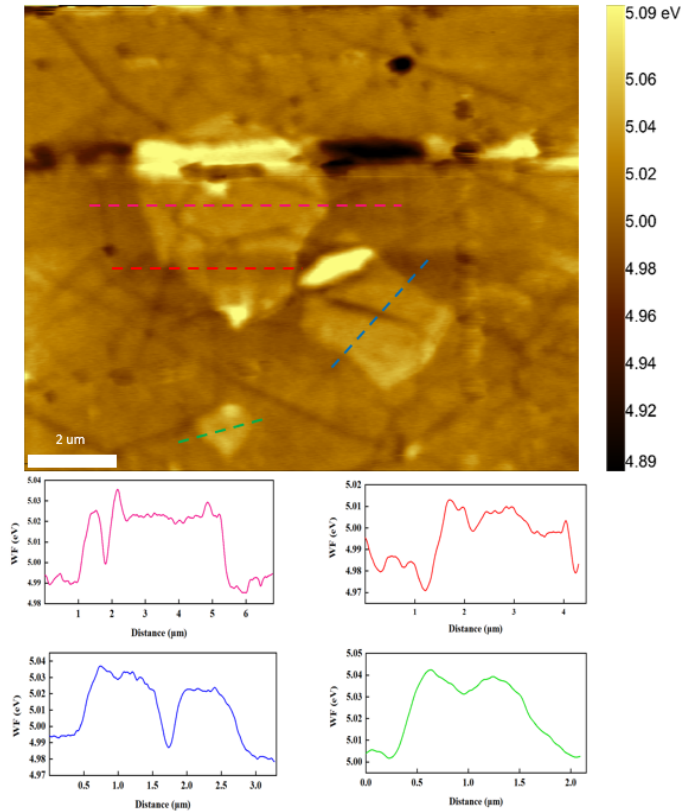
Figure 4.15. Work function of graphene on $NbSe_2$. (Top) Kelvin Probe Force image of graphene covering Niobium Diselenide ($NbSe_2$, (Bottom) line plots of work function across the $NbSe_2$/graphene heterostructure. The graphene on bare SiO_2 has a work function of 4.7 eV, The work function of graphene on top of $NbSe_2$ increased by 3-4 meV compared to graphene on SiO_2.

layered double hydroxide material is an electron donor. The graphene spectra shows a change in carrier density of more than $10^{13}/cm^2$. This may be higher, as N type doping quickly becomes nonlinear in the Raman spectra, making it difficult to predict using Raman spectroscopy. This result also implies a large imbalance in the work function of the material at the edge of the layered double hydroxide materials, as the graphene changes from being P doped to N doped. This large shift in doping values compared to the expect P doping result may be caused in the fabrication. In the
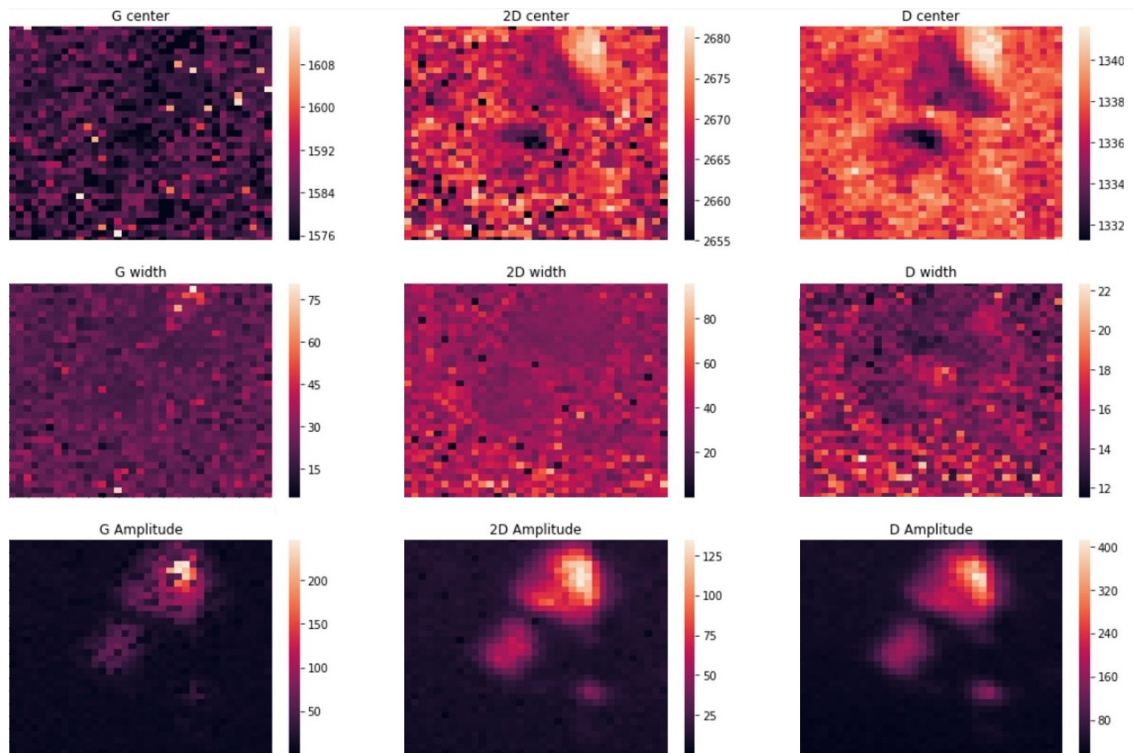
Figure 4.16. Raman maps of graphene covering $NbSe_2$. The graphene covering $NbSe_2$ has sharpened peaks for the G, 2D and D peaks. The 2D center shifts strongly with strain and the D center shifts with doping. Indicating tensile strain and doping on top of this crystal. Each pixel is 200 um.
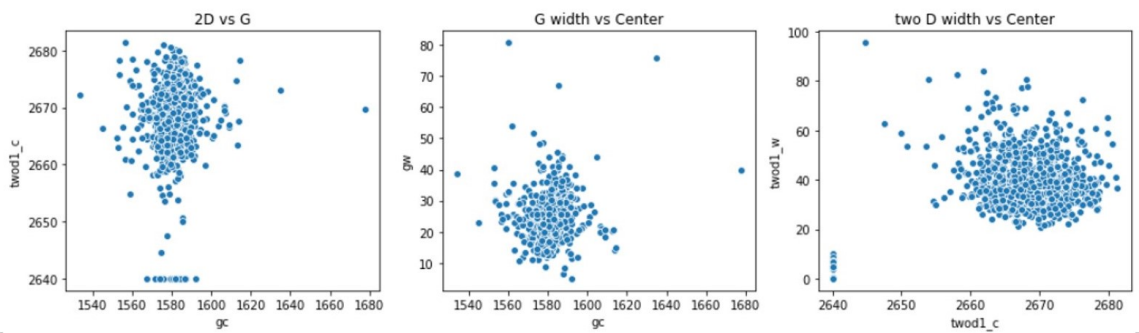
Figure 4.17. Raman Scatter plots of graphene on $NbSe_2$. The 2D vs G plot shows some strain represented by the vertical stretching of cluster of points. The G peak has a tight distribution between its peak location and width, which is expected. However, the 2D peak shows a bimodal distribution along of width vs peak location, representing high hydrostatic and tensile strain.
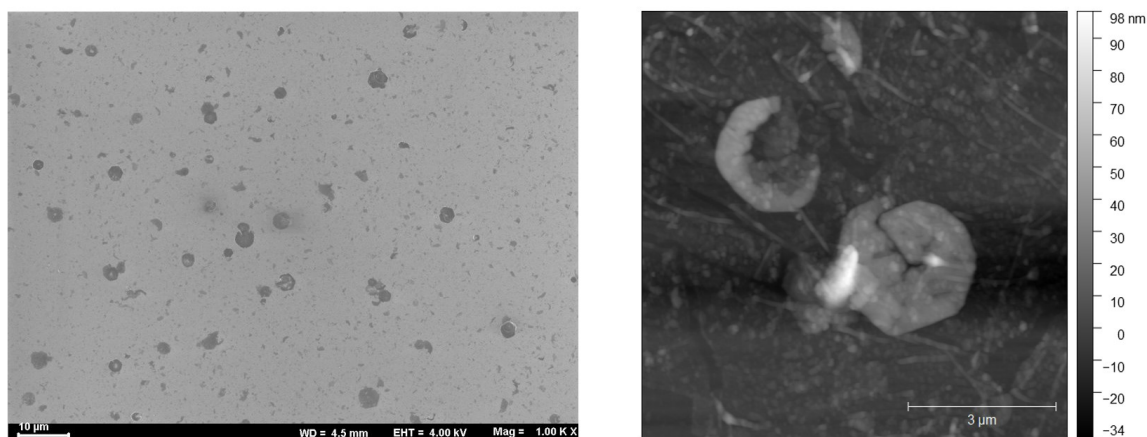
Figure 4.18. (Left SEM image of Mg/Al layered double hydroxide material deposited on SiO_2 substrate. Large hexagons are bulk crystals roughly 60 nm in height. Smaller crystals are visible covering the substrate. (Right) Atomic force microscope height map of graphene covering Mg/Al layered double hydroxide flake. Thinner, but still bulk layered double hydroxide crystals are visible in this Afm map, however the surface roughness of the substrate combined with the graphene covreing the layered double hydroxide makes the thinnest layered double hydroxide material very difficult to detect via AFM.

process of exfoliating and depositing the layered double hydroxide material, formamide or counteranions like NO_3^- or CO_3^- may have been adsorbed to the surface of the layered double hydroxide material. Another possible explanation is anion adsorption onto the graphene surface from the mobile anion layer between static cations. This opens up the possibility for controlled doping through anion exchange inside the layered double hydroxide material or controlling the "memory effect" of these materials which was discussed in the literature review.
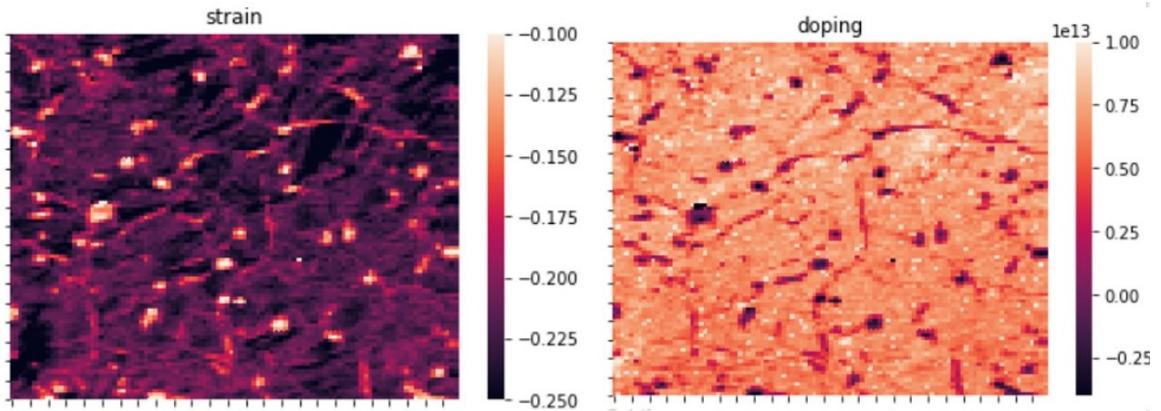
Figure 4.19. Strain (Left) and doping (Right) Raman spectral maps of graphene covering Mg/Al layered double hydroxide flakes. The graphene on top of layered double hydroxide crystals has a small factor of strain due to lattice mismatches compared to the SiO_2 substrate, however the doping map shows significant N doping of the graphene on top of these layered double hydroxide crystals.

4.3.5 Graphene / MoS2$_2$ Label-free Detection of Doxorubicin

In this section, a multidimensional optical technique is developed to understand the role of strain in its effects on the electrical properties of these Van der Waals heterostructures. We fabricated a heterostructure out of monolayer graphene and monolayer Molybdenum Disulfide crystals, which were used for Biosensing. We report optical label-free detection of doxorubicin, a common cancer drug, via photoluminescent shift, Raman shift, and graphene enhanced Raman scattering. The physical origin of the local non-uniform optical broadening of these signals may be revealed by this multidimensional nanoscale imaging, leading to better strategies for the mitigation of this variability in these materials for future device fabrication. Significant efforts have been made to fabricate biosensing devices from a range of 2D materials [4,110,135,146]. Knowledge on what allows successful multimodal detection and what limits biosensing capabilities of 2D heterostructures is scarce. Two dimensional materials often have

75

atomic impurities, crystalline defects, or folds which can modify their optical properties. Study into how these nano-scale non-uniformities affect the micron scale devices is critical, and the role that these defects play in a materials properties is not yet understood. Techniques which can detect these non-uniformities such as Scanning Electron Microscopy lack the ability to detect the electrical properties of the materials, while the optical methods which can detect the inhomogeneities lack the resolution to see the defects. The scale of these non-uniformities can also be signifigantly smaller than the active area of a sensing device. Thus, in order to reveal mechanisms that control sensing, we use multiple characterization tools to correlate these techniques. We use Raman and near-field microscopies, scanning probe, and electron microscopy to unvail physical processes behind label-free multimodal detection of doxorubicin (DOX), which is an anthracycline cancerdrug, using vertical heterostructures from two dimensional materials.

Doxyrubicin, a widely used drug for treating various types of cancer, is known for certain drug resistances and side effects. A reliable method for detecting the amount of drug in different biological samples, especially at the point of care, is crucial. Recently, DOX has been detected on various two dimensional materials including graphene oxide and other nanocomposites [20, 46, 86, 150]. Dox has been detected in various cell lines and real samples through Raman microscopy and surface enhanced Raman spectroscopy. We use three different channels are used to detect DOX: throug hanalyzing the graphene enhanced Raman spectra of the drug, the Raman shift of monolayer graphene, and the photluminescence shift of single-layer MoS_2.

This device we studied is a label-free device which avoids the need for a high-optical-contrast receptor for the analyte. This device shows the capability of being more versatile in sensing a wide array of analytes, which could enable agnostic biosensing
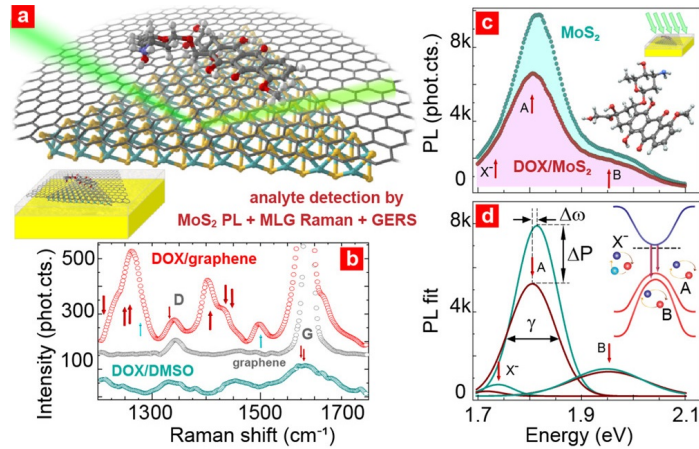
Figure 4.20. from [50]Multidimensional detection of doxorubicin (DOX) drug in Van der waals heterostructure using Raman shift of graphene, DOX GERS, and photoluminescence of MoS_2. A) schematic representation of analyte molecule on monolayer graphene / MoS_2 heterostructure on Si/SiO_2 substrate. B) GERS signal of DOX/single layer graphene (red), vs reference Raman spectra of DOX in dimethyl sulfoxide solution (cyan), and single layer graphene (gray); red (cyan) arrows mark DOX (DMSO) lines. C) shift of the MoS_2 photoluminescent spectrum: with DOX (red) and w/o Dox (cyan); inset shows DOX molecular molecule. D) The fit of the measured photoluminescence spectra from (C). A/B-exciton and trion (X$^-$) lines are shown; shifting of peak position ($\Delta\omega$) and intensity (ΔP) are indicated using A-exciton fit; The inset shows the schematics of the optical bands of MoS_2.

and detecting of unknown biothreats where receptors are unavailable or have not yet been developed. However, lable-free biosensing has lower specificity than labled biosensing. To increase specificity we choose to use multiplex sensing which has shown promise when combined with machine learning to converting multiple inputs to a readable test result. [28, 75, 145]

Molybdenum disulfide is a well known two dimensional transition metal dichalcogenide with a strong photoluminescent(PL) signal. Adsorption of molecules to the TMDC modulates the photoluminescence signal. In Figure 4.20c, we show the photoluminescence spectra of MoS_2 before and after incubation with 172 nM solution of DOX for 15 minutes and note a marked difference. The photoluminescence spectra is
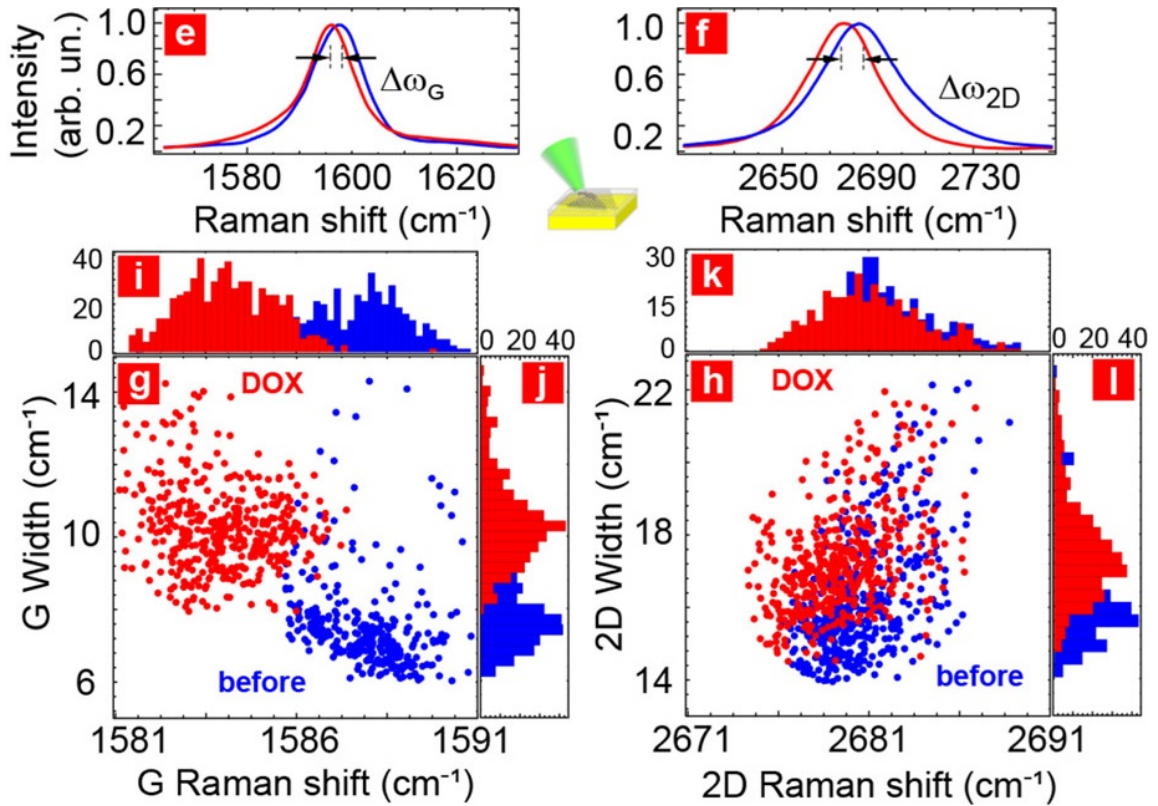
Figure 4.21. from [50], e and f) Typical G and 2D Raman spectra of single layer graphene: with DOX (red) and before incubation (blue); G and 2D-line intensities were normalized by unity. g and h) Correlation plots and (i-l) partial distribution plots for peak position and with for G- and 2D- lines, spaced equally on the MoS_2 island, at diffraction limited step sizes, same color code as in (e and f); clear line red shift and broadening is detected with DoX.

dominated by two excitonic subbands B- and A- excitons, and a trion X^-. We plot these points in Figure 4.20d. The shift of the peak position ($\Delta\omega$), peak intensity (ΔP), and with ($\Delta\gamma$) are evidence of analyte adsorption, resulting in doping and strain imposed onto the 2D material. These shifts vary depending on the type and concentration of the analyte. Table 4.1 provide the values for a given concentration. Our fitting shows that the peak positions of the A-exciton and trion, the width broadens and the intensity decreases, while the B-exciton is only partially influenced with a small

intensity difference. Reducing noise in the signal would improve the ability to detect low concentrations of DOX. The variation of the signal in the pristine no-analyte material increases the total uncertainty and reduces device performance as discussed below.

Table 4.1. photoluminescence Fit Parameters for Figure 4.20d

	ω_c	γ	P
	Trion		
With DOX	1.739 ± 0.002	$60. \pm 3$	32 ± 4
W/O DOX	1.719 ± 0.003	$60. \pm 9.$	15 ± 3
	A-exciton		
With DOX	1.815 ± 0.0002	82.0 ± 0.3	793 ± 4
W/O DOX	1.806 ± 0.002	90.7 ± 0.3	586 ± 3
	B-exciton		
With DOX	1.953 ± 0.001	135.8 ± 2	203 ± 1
W/O DOX	1.955 ± 0.002	135.0 ± 2	197 ± 2

The graphene Raman spectra may also be analyzed, adding another channel to this multiplexed detection with the photoluminescence data. Parts e and f of Figure 4.21 show a strong red shift and broadening of the G and 2D bands when DOX is adsorbed. Panels g-l show statistical information about the shift and broadening of both peaks where each point is a diffraction limited region on the sample with a spot size less than 0.1 μm^2. The data points aggregate in two separate clusters with point-to-point variability caused by non-uniformity of the signal in the 2D-mode which will be discussed next.

4.3.6   Stability of 2D Van der Waals heterostructure Materials

Scanning electron microscopy reveals non-uniformities in the structure of the MoS_2 / graphene heterostructure. Figure 4.23e shows SEM of a typical heterostructure of MoS_2 covered by monolayer graphene. White nanocrystals are visible near the edge of the heterostructure (metal precipitation cite) which shows charging, likely due to growth of insulating molybdenum oxide or Mo_2O_3. Other samples also had this contamination near the center of the MoS_2 crystals (metal nucleation site).
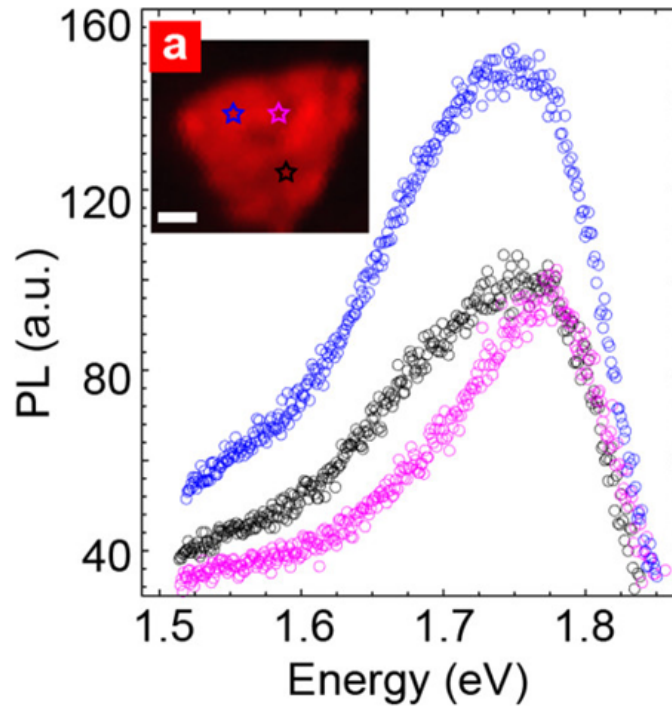
Figure 4.22. from [50] Photoluminescence spectra of MoS_2 island. Stars in inset show location the photoluminescence was taken.
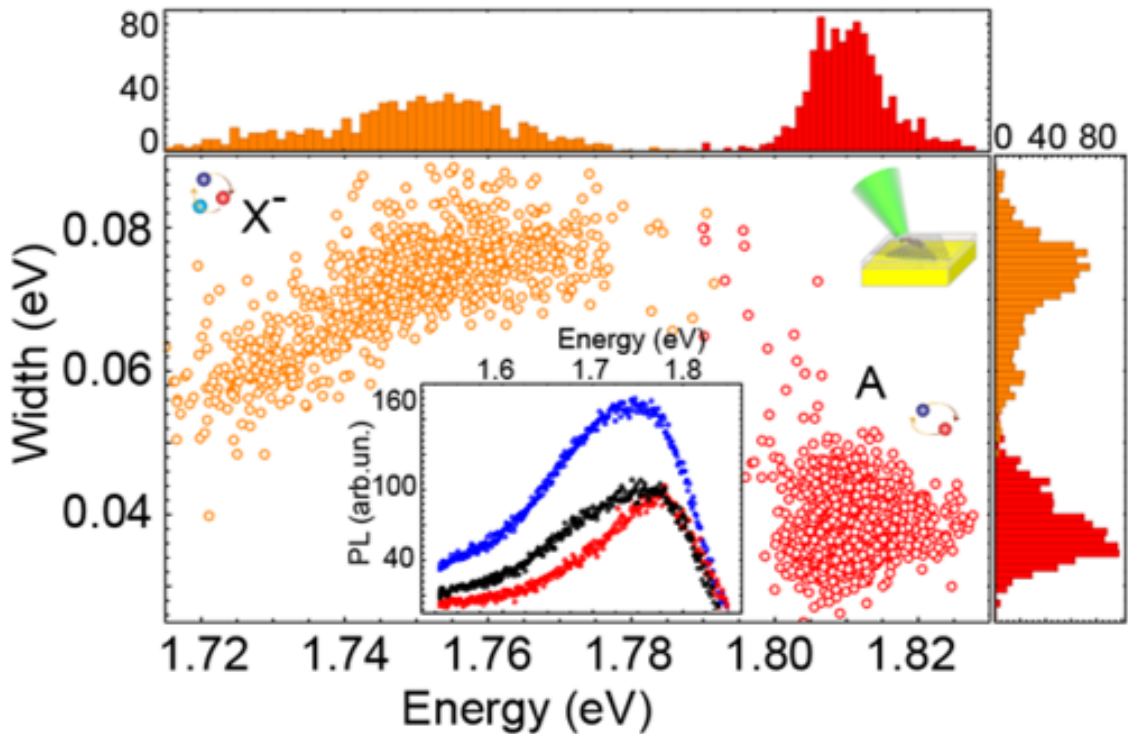
Figure 4.23. from [50], Correlation plots and partial distribution functions for peak positions and with for A-exciton (red) and trion (orange) lines, measured locally; Clustering is visible for trion points, which are highlighted in the partial distribution plots.

The surface of the MoS_2 heterostructure appears mostly uniform in the SEM image. However, the optical properties of the heterostructure show substantial variation with the large scatter of Raman and photoluminescence distributions Figure 4.21 and Figure 4.22. The variability in pristine material could produce uncertainty in detection of analytes. In order to find the physical origin for such variation, we used scattering scanning near-field optical microscopy (sSNOM). By aligning the large area scans of the heterostructer we correlate different characterization channels including SEM, scanning probe imaging, as well as photoluminescence and Raman microscopy at a lower resolution. in Figure 4.25 b-d, the sSNOM image of second harmonic optical
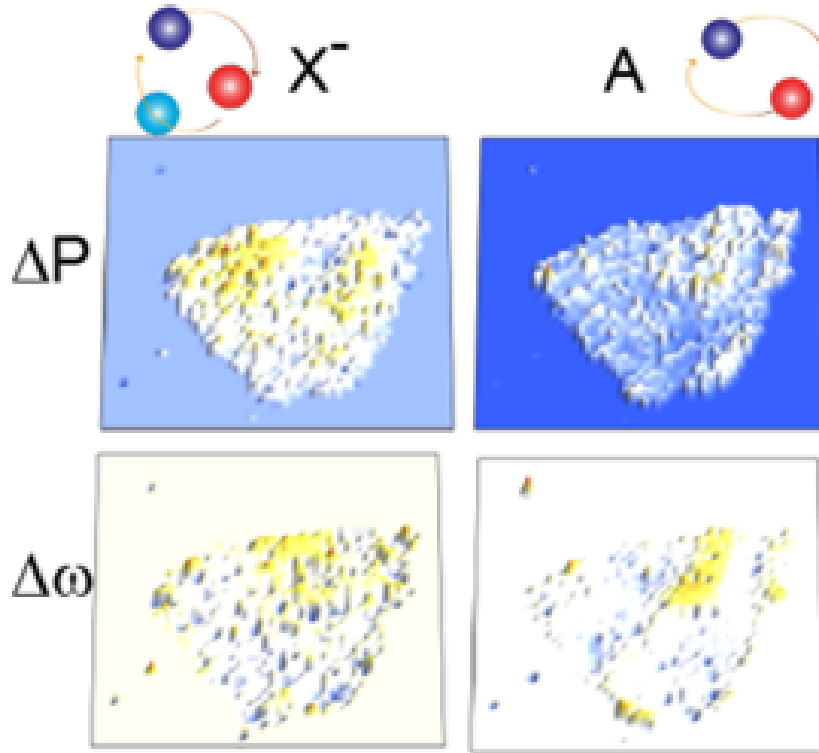
Figure 4.24. from [50], confocal maps of MoS$_2$ PL: (top row) fitted intensity and (bottom row) peak position for (left) trion and (right) A-exciton; arrows show regions of higher photoluminescence intensity for trion(lower for A-exciton). All scale bars are 1 μm.

amplitude (see methods section) reveals variation of the surface impedance of the heterostructure at submicrometer scale not captured by SEM or AFM. We claim that the bright regions correspond to the local defects of the MoS$_2$. We regularly observe such contrast at the edges of MoS$_2$ crystals which are prone to oxidation. Similar regions in the center of the island should correspond to concentrated sulfur vacancies, reactive to oxygen, and formation of oxy-sulfate regions which may appear as nanoscale posts that wrinkle the graphene which drapes above. The series of maps in Figure
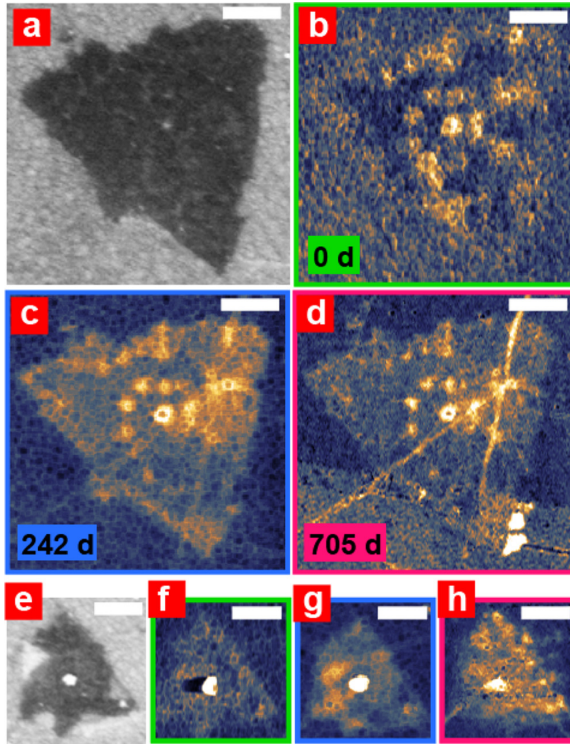
Figure 4.25. from [50], test of the MoS_2/graphene heterostructure. (a and e) Scanning electron microscopy image, and (b-d and f-h) sSNOM images of two MoS_2 islands covered by monolayer graphene. The island that is well covered by graphene (a) shows nearly no degradation after 242 or 705 days in ambient conditions. The island (e) has torn graphene covered the MoS_2 island, which has lead to severe degradation of the device. All scale bars are 1 μm.

4.25 b-d, f-h show how such regions may grow while protected (or not protected) by graphene. The larger island (a), is covered with intact monolayer graphene, which preserves the oxidized region after nearly 2 years in ambient conditions, except for a small oxide crystal growth near the bottom right corner where a gouge in the graphene has exposed the MoS_2 to oxygen. While in the smaller island (e) the graphene is cracked, leading to oxidation over the same period. The sSNOM mapping also shows large wrinkles in the graphene which show up as bright diagonal lines in (d) which do not contribute to alterations of the optical properties over time.

Pristine material was also analyzed in another island of the same MoS_2/graphene heterostructure mapped in Figure 4.22 by photoluminescence in panel a and by SEM in panel e (and will be correlated in Figure 4.27h. Several features are clearly resolved: graphene ruptures off of the island, an oxide crystallite on the bottom left edge of the MoS_2 crystal, numerous oxy-sulfate nanoposts and graphene wrinkles around those posts, as well as several regions of darker SEM contrast (likely, more conductive than bare monolayer graphene). Confocal photoluminescence image of the same area is present in Figure 4.22a, inset. On this MoS_2 island there is considerable variability in the photoluminescence intensity and lineshape.Similar to the large area photoluminescence data in Figure 4.20. The main variability of micro-photoluminescence results from the A and X^- states, to be analyzed separately. Panel b presents the correlation plot for fitted photoluminescence peak position and width for A-exciton (red) and trion (orange) states by the local optical probe on the surface of the graphene/ MoS_2 heterostructure. This corresponds with the analysis in figure 4.24. Microphotoluminescence reveals a large non-uniformity in optical signal. Trion partial distribution functions for both $\Delta\gamma$ and $\Delta\omega$ show three major clusters (highlighted by ovals in panel b and green curves in c and d), which correspond to the regions of heterostructure where materials properties are locally modulated. Maps in Figure 4.22f-i show the distribution of the peak position, $\Delta\omega$, and peak intensity, ΔP, with diffraction limited resolution. These maps show a negative correlation for the photoluminescence strength of A-exciton and trion (shown by the red and orange arrows). The trion photoluminescence is at a maximum where the A-exciton photoluminescence is depressed which is what is shown in the blue and black spectra in panel A. The A-exciton dominated spectra is shown in the purple photoluminescence curve in panel a. We speculate that this correlation may be the result from the non-uniform doping of the MoS_2 island.
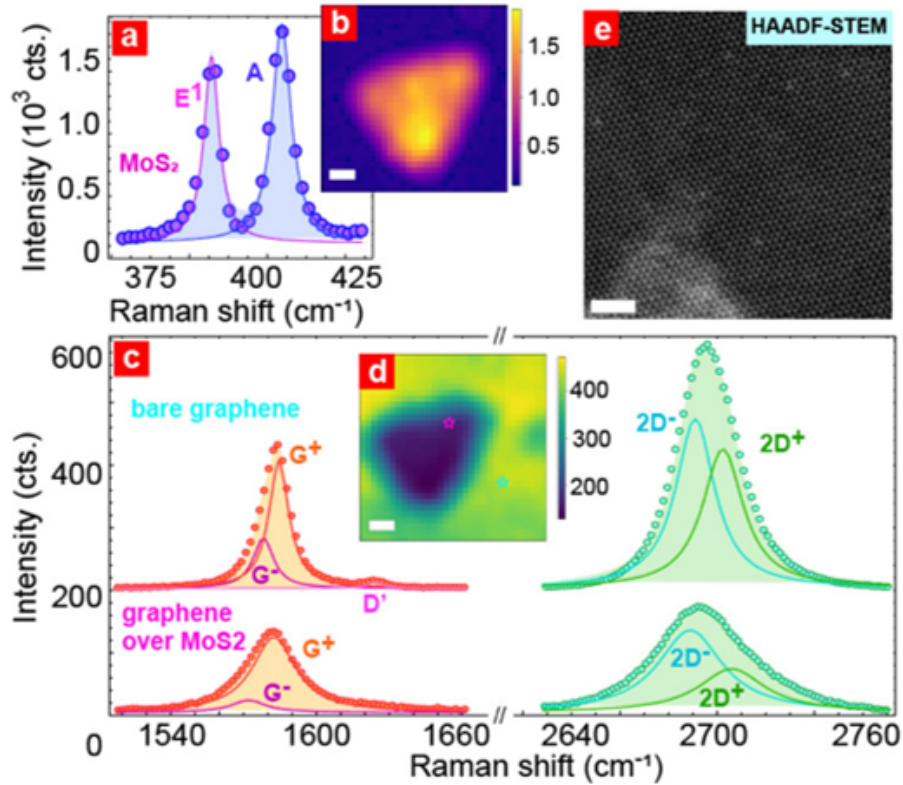
Figure 4.26. from [50], (a) typical MoS$_2$ Raman spectrum, fitted with E$_{2g}$ and A$_{1g}$ lines. (b) A-line intensity map. (c) Typical Raman spectra for graphene off/on MoS$_2$ island, fitted by G(orange), D (pink), and 2D (green) lines; splitting of G- and 2D-lines is shown in the fit. (d) Raman map of 2D-aplitude showing the island location, cg. map in (b). (e) High-angular annular dark-field scanning transmission electron microscopy (HADF_STEM) image of MoS$_2$ lattice: notice grain boundaries and individual defects; scale bar is 2nm.

In highly doped areas, neutral excitons are bound to free charges and are converted into trions [79].

While it is useful to shed light on the photoluminescent variability, the confocal photoluminescence characterization does not have the spacial resolution to determine the mechanism of non-uniform optical signaling. We developed a multidimensional imaging method combining sSNOM and Kelvin probe force microscopy with photoluminescence and Raman microscopy.
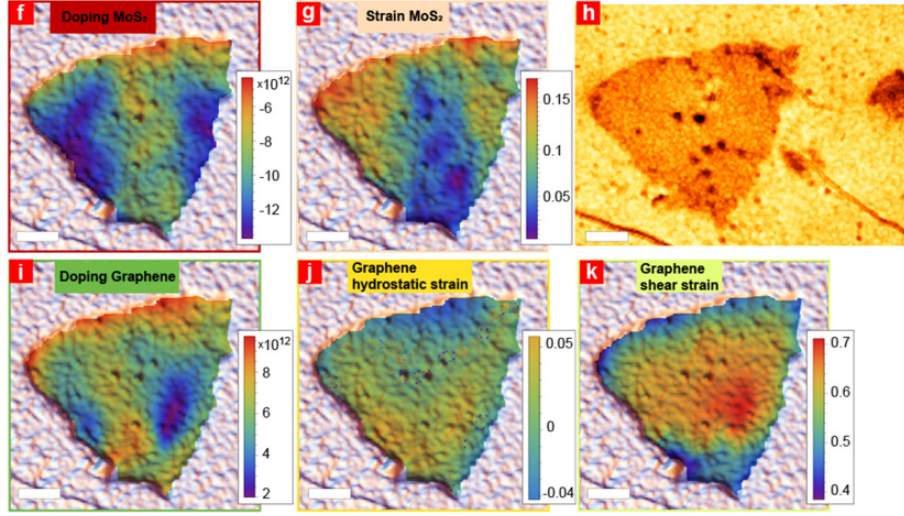
Figure 4.27. from [50], Raman mapping of doping and strain non-uniformities in the heterostructure. (f and g) Calculated doping and strain for MoS_2 layer overlaid with SEM map; (h) sSNOM phase image of the same area. (i-k) single layer graphene doping, hydrostatic and shear strain maps. All scale bars except in (e) are 1 μm.

Multiple sources of optical non-uniformity, stemming from the variation of the doping level, have been studied with micro-Raman imaging: typical Raman spectra of monolayer graphene/MoS_2 heterostructure are shown in Figure 4.26 Panel a presents A- and E-modes of the MoS_2 layer; an A-intensity map is shown in the inset of b. Mode frequencies, fitted as in a, allow us to determine the strain and doping (60) of the island underneath the graphene, generating the maps presented in panels f and g (see the Methods section for details). MoS_2 doping is lower along the vertical axis of the island; thus, both the amount of charge transfer and graphene E_F should be lower. Charge doping and strain in graphene have been calculated. Parts i and j of Figure 4.27 show graphene doping and isotropic/hydrostatic strain. Furthermore, the splitting of the G and 2D doublet modes (see the fitted curves in panel c) yields the shear (non-isotropic) component of the strain (panel k).

4.3.7   Summary

The analysis above reveal the existence of non-uniformities in 2D materials at the nanoscale level and the multidimensional characterization which I proposed in Aim 2 allow for the identification of doping and strain variations as the origin of inhomogenieties of optical and electrical properties. When these defects are averaged over the device area, variability in local response induces a broadening of the spectral signal, which raises device-to-device variability and, ultimately, lowers the sensitivity and the limit of detection by increasing background signal and systematic error. The work above show that in order to improve the performance of devices based on 2D heterostructures, non-uniformity of doping and strain – two major mechanisms for optical signal variations – must be addressed. New methods of strain-free and doping-free transfer need to be developed, and failing that, each device must be analyzed thoroughly for deviations.

4.4   Instrumentation

SEM sample imaging was performed on a field emission scanning electron microscope Zeiss Auriga FIB/FESEM. Confocal PL and Raman characterization were performed using a Horiba Jobin Yvon LabRAM HR-Evolution Raman system; 488 nm (for Raman) and 532 nm (for PL) laser excitation wavelengths were used. A Horiba XploRA Raman system was used for taking the Raman spectra at 532 nm of excitation; WiTec Raman alpha 300 Confocal system, excitation: 488 nm, 532 nm. sSNOM maps were collected using a scattering type scanning near-field optical microscope (custom-built Neaspec system) in pseudoheterodyne mode excitation 1577–1579 cm^{-1} (at PSU, laboratory

of Dr. Rotkin). The AFM/KPFM characterization was performed using (1) Oxford Research AFM (MFP-3D infinity); (2) Dimension Icon AFM in PeakForce Kelvin probe force microscopy in frequency modulated mode (PFKPFM-FM, Bruker Nano Inc., Santa Barbara, CA). Prior to measuring the samples, the KPFM response of the probe was checked against an Au–Si–Al standard and the work function of the Al reference metal layer was calibrated against a freshly cleaved highly oriented pyrolytic graphite (HOPG) reference sample (PFKPFM-SMPL, HOPG-12M, Bruker SPM Probes, Camarillo, CA); 4.6 eV was used for the work function reference value for HOPG.

Chapter 5: Conclusions and Future work

Current device fabrication techniques leave much to be desired. Due to inhomogenieties caused by transfer methods and growth conditions lead to device to device variations that will effect the performance of two dimensional devices. New techniques must be developed to fabricate these devices without defects and new methodologies must be utilized to detect these variations to ensure uniform properties across all fabricated devices. In this thesis I have developed a new method for determining the number of layers in two dimensional materials using only optical microscopy and optical contrast by Fresnel equations. This methodology can be extended to any two dimensional materials and their Van der Waals heterostructures. I have also used advanced Raman analysis to extract strain and doping information from large characterization area for use in registering Raman spectral maps with other microscopy methods. This methodology can be extended to other two dimensional materials. Finally, I used the registration techniques for examining local variations of layered materials and discovered novel properties of these heterostructures which will be useful in future device fabrication.

Each of my three aims has a future work which may be investigated. The control and detection of lattice angles in bilayer graphene is critical for the application of multi-layered graphene structures. More research is needed into the control of the growth of these materials to prevent these mismatches from occurring unintentionally. structures Layered double hydroxides have interesting interactions with graphene

substrates. More research is needed in the work function characterization of graphene in these heterostructures. Molybdenum disulfide photoluminescence may be controlled by strain engineering of graphene in MoS_2/graphene heterostructures. In terms of registration, more signals may be found for registration purposes in large area two dimensional materials for spectroscopic analysis. This research can be extended into other high resolution optical spectroscopic methods such as FT-IR. Finally, the detection and prediction of few-layer flakes in homogeneous materials seems perfectly extensible into two dimensional heterostructures. Research into the apparent color of these heterostructures is not something currently being studied and optical estimation of layer number or z height is possible using Fresnel equations.

Figure 5.1. .

References

[1] Deji Akinwande, Nicholas Petrone, and James Hone. Two-dimensional flexible nanoelectronics. *Nature Communications*, 5(1):5678, December 2014. Number: 1 Publisher: Nature Publishing Group.

[2] George Anagnostopoulos, Charalampos Androulidakis, Emmanuel N. Koukaras, Georgia Tsoukleri, Ioannis Polyzos, John Parthenios, Konstantinos Papagelis, and Costas Galiotis. Stress Transfer Mechanisms at the Submicron Level for Graphene/Polymer Systems. *ACS Applied Materials & Interfaces*, 7(7):4216–4223, February 2015.

[3] Tsuneya Ando. Magnetic Oscillation of Optical Phonon in Graphene. *Journal of the Physical Society of Japan*, 76(2):024712, February 2007.

[4] Hadi Arjmandi-Tash, Liubov A. Belyaeva, and Grégory F. Schneider. Single molecule detection with graphene and other two-dimensional materials: nanopores and beyond. *Chemical Society Reviews*, 45(3):476–493, Feb 2016.

[5] Frederick Aryeetey, Tetyana Ignatova, and Shyam Aravamudhan. Quantification of defects engineered in single layer MoS2. *RSC Advances*, 10(39):22996–23001, June 2020. Publisher: The Royal Society of Chemistry.

[6] Frederick Aryeetey, Sajedeh Pourianejad, Olubukola Ayanbajo, Kyle Nowlin, Tetyana Ignatova, and Shyam Aravamudhan. Bandgap recovery of monolayer mos 2 using defect engineering and chemical doping. *RSC Advances*, 11(34):20893–20898, 2021.

[7] B. B. Avants, C. L. Epstein, M. Grossman, and J. C. Gee. Symmetric diffeomorphic image registration with cross-correlation: Evaluating automated labeling of elderly and neurodegenerative brain. *Medical image analysis*, 12(1):26–41, Feb 2008.

[8] Amelie Axt, Ilka Hermes, Victor Bergmann, Niklas Tausendpfund, and Stefan Weber. Know your full potential: Quantitative kelvin probe force microscopy on nanoscale electrical devices. *Beilstein Journal of Nanotechnology*, 9:1809–1819, Jun 2018.

[9] Olubunmi O. Ayodele, Sajedeh Pourianejad, Anthony Trofe, Aleksandrs Prokofjevs, and Tetyana Ignatova. Application of soxhlet extractor for ultra-clean graphene transfer. *ACS Omega*, 7(8):7297–7303, Mar 2022.

[10] Yang Bai, Weiqi Wang, Ranran Wang, Jing Sun, and Lian Gao. Controllable synthesis of 3d binary nickel–cobalt hydroxide/graphene/nickel foam as a binder-free electrode for high-performance supercapacitors. *Journal of Materials Chemistry A*, 3(23):12530–12538, Jun 2015.

[11] L Banszerus, H Janssen, M Otto, A Epping, T Taniguchi, K Watanabe, B Beschoten, D Neumaier, and C Stampfer. Identifying suitable substrates for high-quality graphene-based heterostructures. *2D Materials*, 4(2):025030, February 2017.

[12] W. Bao, L. Jing, J. Velasco, Y. Lee, G. Liu, D. Tran, B. Standley, M. Aykol, S. B. Cronin, D. Smirnov, M. Koshino, E. McCann, M. Bockrath, and C. N. Lau. Stacking-dependent band gap and quantum transport in trilayer graphene. *Nature Physics*, 7(12):948–952, 2011.

[13] M. Beshkova, L. Hultman, and R. Yakimova. Device applications of epitaxial graphene on silicon carbide. *Vacuum*, 128:186–197, June 2016.

[14] Md. Sajibul Alam Bhuyan, Md. Nizam Uddin, Md. Maksudul Islam, Ferdaushi Alam Bipasha, and Sayed Shafayat Hossain. Synthesis of graphene. *International Nano Letters*, 6(2):65–83, Jun 2016.

[15] Merijntje S. Bronsgeest, Nedjma Bendiab, Shashank Mathur, Amina Kimouche, Harley T. Johnson, Johann Coraux, and Pascal Pochet. Strain Relaxation in CVD Graphene: Wrinkling with Shear Lag. *Nano Letters*, 15(8):5098–5104, August 2015. Publisher: American Chemical Society.

[16] Sheneve Z. Butler, Shawna M. Hollen, Linyou Cao, Yi Cui, Jay A. Gupta, Humberto R. Gutiérrez, Tony F. Heinz, Seung Sae Hong, Jiaxing Huang, Ariel F. Ismach, Ezekiel Johnston-Halperin, Masaru Kuno, Vladimir V. Plashnitsa, Richard D. Robinson, Rodney S. Ruoff, Sayeef Salahuddin, Jie Shan, Li Shi, Michael G. Spencer, Mauricio Terrones, Wolfgang Windl, and Joshua E. Goldberger. Progress, Challenges, and Opportunities in Two-Dimensional Materials Beyond Graphene. *ACS Nano*, 7(4):2898–2926, April 2013. Publisher: American Chemical Society.

[17] C. Casiraghi, A. Hartschuh, H. Qian, S. Piscanec, C. Georgi, A. Fasoli, K. S. Novoselov, D. M. Basko, and A. C. Ferrari. Raman Spectroscopy of Graphene Edges. *Nano Letters*, 9(4):1433–1441, April 2009.

[18] F. Cavani, F. Trifirò, and A. Vaccari. Hydrotalcite-type anionic clays: Preparation, properties and applications. *Catalysis Today*, 11(2):173–301, Dec 1991.

[19] Biswanath Chakraborty, Achintya Bera, D. V. S. Muthu, Somnath Bhowmick, U. V. Waghmare, and A. K. Sood. Symmetry-dependent phonon renormalization in monolayer MoS$\{\}\_\{2\}$ transistor. *Physical Review B*, 85(16):161403, April 2012. Publisher: American Physical Society.

[20] Jiayi Chen, Chenhong Qian, Peng Ren, Han Yu, Xiangjia Kong, Chenglong Huang, Huanhuan Luo, and Gang Chen. Light-responsive micelles loaded with doxorubicin for osteosarcoma suppression. *Frontiers in Pharmacology*, 12, 2021.

[21] Xiaoqing Chen, Khurram Shehzad, Li Gao, Mingsheng Long, Hui Guo, Shuchao Qin, Xiaomu Wang, Fengqiu Wang, Yi Shi, Weida Hu, Yang Xu, and Xinran Wang. Graphene Hybrid Structures for Integrated and Flexible Optoelectronics. *Advanced Materials*, 32(27):1902039, 2020.

[22] Yingwen Cheng, Hongbo Zhang, Chakrapani V. Varanasi, and Jie Liu. Improving the performance of cobalt–nickel hydroxide-based self-supporting electrodes for supercapacitors using accumulative approaches. *Energy and Environmental Science*, 6(11):3314–3321, Oct 2013.

[23] Warren Cheung and Ghassan Hamarneh. N-sift: N-dimensional scale invariant feature transform for matching medical images. In *2007 4th IEEE International Symposium on Biomedical Imaging: From Nano to Macro*, page 720–723, Arlington, VA, USA, 2007. IEEE.

[24] H. Cheun Lee, Wei-Wen Liu, Siang-Piao Chai, Abdul Rahman Mohamed, Azizan Aziz, Cheng-Seong Khe, N. M. S. Hidayah, and U. Hashim. Review of the synthesis, transfer, characterization and growth mechanisms of single and multilayer graphene. *RSC Advances*, 7(26):15644–15693, 2017.

[25] Woosuk Choi, Young Soo Seo, Jun Young Park, K. B. Kim, Jongwan Jung, Naesung Lee, Yongho Seo, and Suklyun Hong. Effect of annealing in ar/h2 environment on chemical vapor deposition-grown graphene transferred with poly (methyl methacrylate). *IEEE Transactions on Nanotechnology*, 14(1):70–74, Jan 2015.

[26] S. Chunhavittayatera, O. Chitsobhuk, and K. Tongprasert. Image registration using hough transform and phase correlation. In *2006 8th International Conference Advanced Communication Technology*, volume 2, page 5 pp. – 977, Feb 2006.

[27] Giulio Cocco, Emiliano Cadelano, and Luciano Colombo. Gap opening in graphene by shear strain. *Physical Review B*, 81(24):241412, June 2010. arXiv: 1006.1999.

[28] Feiyun Cui, Yun Yue, Yi Zhang, Ziming Zhang, and H. Susan Zhou. Advancing biosensors with machine learning. *ACS Sensors*, 5(11):3346–3364, Nov 2020.

[29] A. Das, B. Chakraborty, S. Piscanec, S. Pisana, A. K. Sood, and A. C. Ferrari. Phonon renormalization in doped bilayer graphene. *Physical Review B*, 79(15):155417, April 2009. Publisher: American Physical Society.

[30] A. Das, S. Pisana, B. Chakraborty, S. Piscanec, S. K. Saha, U. V. Waghmare, K. S. Novoselov, H. R. Krishnamurthy, A. K. Geim, A. C. Ferrari, and A. K. Sood. Monitoring dopants by Raman scattering in an electrochemically top-gated graphene transistor. *Nature Nanotechnology*, 3(4):210–215, April 2008.

[31] Anoop S. Dhoot, Jonathan D. Yuen, Martin Heeney, Iain McCulloch, Daniel Moses, and Alan J. Heeger. Beyond the metal-insulator transition in polymer

electrolyte gated polymer field-effect transistors. *Proceedings of the National Academy of Sciences*, 103(32):11834–11837, August 2006. Publisher: National Academy of Sciences Section: Physical Sciences.

[32] Richard O. Duda and Peter E. Hart. Use of the Hough transformation to detect lines and curves in pictures. *Communications of the ACM*, 15(1):11–15, January 1972.

[33] C. Faugeras, P. Kossacki, D. M. Basko, M. Amado, M. Sprinkle, C. Berger, W. A. de Heer, and M. Potemski. Effect of a magnetic field on the two-phonon Raman scattering in graphene. *Physical Review B*, 81(15):155436, April 2010. arXiv: 1001.1614.

[34] Y. Feldman, G. L. Frey, M. Homyonfer, V. Lyakhovitskaya, L. Margulis, H. Cohen, G. Hodes, J. L. Hutchison, and R. Tenne. Bulk synthesis of inorganic fullerene-like ms2 (m = mo, w) from the respective trioxides and the reaction mechanism. *Journal of the American Chemical Society*, 118(23):5362–5367, Jan 1996.

[35] A. C. Ferrari, J. C. Meyer, V. Scardaci, C. Casiraghi, M. Lazzeri, F. Mauri, S. Piscanec, D. Jiang, K. S. Novoselov, S. Roth, and A. K. Geim. Raman Spectrum of Graphene and Graphene Layers. *Physical Review Letters*, 97(18), October 2006.

[36] Andrea C. Ferrari. Raman spectroscopy of graphene and graphite: Disorder, electron–phonon coupling, doping and nonadiabatic effects. *Solid State Communications*, 143(1-2):47–57, July 2007.

[37] Andrea C. Ferrari and Denis M. Basko. Raman spectroscopy as a versatile tool for studying the properties of graphene. *Nature Nanotechnology*, 8(4):235–246, April 2013. arXiv: 1306.5856.

[38] Otakar Frank, Jana Vejpravova, Vaclav Holy, Ladislav Kavan, and Martin Kalbac. Interaction between graphene and copper substrate: The role of lattice orientation. *Carbon 68, 440-451 (2014)*, January 2014.

[39] Libo Gao, Wencai Ren, Feng Li, and Hui-Ming Cheng. Total color difference for rapid and accurate identification of graphene. *ACS Nano*, 2(8):1625–1633, Aug 2008.

[40] Zan Gao, Clifton Bumgardner, Ningning Song, Yunya Zhang, Jingjing Li, and Xiaodong Li. Cotton-textile-enabled flexible self-sustaining power packs via roll-to-roll fabrication. *Nature Communications*, 7(11):11586, May 2016.

[41] Zhaoli Gao, Meng-Qiang Zhao, Md Masruck Alam Ashik, and Alan T Charlie Johnson. Recentadvances in the propertiesand synthesis of bilayer graphene and transition metal dichalcogenides. *Journal of Physics: Materials*, 3(4):042003, sep 2020.

[42] A. K. Geim and K. S. Novoselov. The rise of graphene. *Nature Materials*, 6(3):183–191, 2007.

[43] A. N. Grigorenko, M. Polini, and K. S. Novoselov. Graphene plasmonics. *Nature Photonics*, 6(11):749–758, November 2012. Number: 11 Publisher: Nature Publishing Group.

[44] Jingbin Han, Yibo Dou, Jingwen Zhao, Min Wei, David G. Evans, and Xue Duan. Flexible coal ldh@pedot core/shell nanoplatelet array for high-performance energy storage. *Small (Weinheim an Der Bergstrasse, Germany)*, 9(1):98–106, Jan 2013.

[45] Wilford N. Hansen and Galen J. Hansen. Standard reference surfaces for work function measurements in air. *Surface Science*, 481:172–184, Jun 2001. ADS Bibcode: 2001SurSc.481..172H.

[46] Yishan He and Xinguang Qiu. Chidamide combined with doxorubicin leads to synergistic anti-cancer effect and induces autophagy through inhibiting the pi3k/akt/mtor pathway in anaplastic thyroid carcinoma. page 2020.05.19.105288, May 2020.

[47] Cheng Hu, Tongyao Wu, Xinyue Huang, Yulong Dong, Jiajun Chen, Zhichun Zhang, Bosai Lyu, Saiqun Ma, Kenji Watanabe, Takashi Taniguchi, Guibai Xie, Xiaojun Li, Qi Liang, and Zhiwen Shi. In-situ twistable bilayer graphene. *Scientific Reports*, 12(1):204, 2022.

[48] Mingyuan Huang, Hugen Yan, Changyao Chen, Daohua Song, Tony F. Heinz, James Hone, and Mildred S. Dresselhaus. Phonon Softening and Crystallographic Orientation of Strained Graphene Studied by Raman Spectroscopy. *Proceedings of the National Academy of Sciences of the United States of America*, 106(18):7304–7308, 2009.

[49] Mingyuan Huang, Hugen Yan, Tony F. Heinz, and James Hone. Probing Strain-Induced Electronic Structure Change in Graphene by Raman Spectroscopy.

Nano Letters, 10(10):4074–4079, October 2010. Publisher: American Chemical Society.

[50] Tetyana Ignatova, Sajedeh Pourianejad, Xinyi Li, Kirby Schmidt, Frederick Aryeetey, Shyam Aravamudhan, and Slava V. Rotkin. Multidimensional imaging reveals mechanisms controlling multimodal label-free biosensing in vertical 2dm-heterostructures. *ACS Nano*, 16(2):2598–2607, February 2022. Publisher: American Chemical Society.

[51] Muhammad Waqas Iqbal, Kinza Shahzad, Rehan Akbar, and Ghulam Hussain. A review on raman finger prints of doping and strain effect in tmdcs. *Microelectronic Engineering*, 219:111152, Jan 2020.

[52] Jens Christian Johannsen, Søren Ulstrup, Federico Cilento, Alberto Crepaldi, Michele Zacchigna, Cephise Cacho, I. C. Edmond Turcu, Emma Springate, Felix Fromm, Christian Raidel, Thomas Seyller, Fulvio Parmigiani, Marco Grioni, and Philip Hofmann. Direct view of hot carrier dynamics in graphene. *Physical Review Letters*, 111(2):027403, Jul 2013.

[53] Amal Kasry, Marcelo A. Kuroda, Glenn J. Martyna, George S. Tulevski, and Ageeth A. Bol. Chemical Doping of Large-Area Stacked Graphene Films for Use as Transparent, Conducting Electrodes. *ACS Nano*, 4(7):3839–3844, July 2010. Publisher: American Chemical Society.

[54] Keun Soo Kim, Yue Zhao, Houk Jang, Sang Yoon Lee, Jong Min Kim, Kwang S. Kim, Jong-Hyun Ahn, Philip Kim, Jae-Young Choi, and Byung Hee Hong. Large-scale pattern growth of graphene films for stretchable transparent electrodes.

Nature, 457(7230):706–710, February 2009. Number: 7230 Publisher: Nature Publishing Group.

[55] Kyounghwan Kim, Ashley DaSilva, Shengqiang Huang, Babak Fallahazad, Stefano Larentis, Takashi Taniguchi, Kenji Watanabe, Brian J. LeRoy, Allan H. MacDonald, and Emanuel Tutuc. Tunable moiré bands and strong correlations in small-twist-angle bilayer graphene. *Proceedings of the National Academy of Sciences*, 114(13):3364–3369, 2017.

[56] Katharina Klein, Alexander M. Gigler, Thomas Aschenbrenner, Roberto Monetti, Wolfram Bunk, Ferdinand Jamitzky, Gregor Morfill, Robert W. Stark, and Jürgen Schlegel. Label-free live-cell imaging with confocal raman microscopy. *Biophysical Journal*, 102(2):360–368, Jan 2012.

[57] J. Theo Kloprogge and Ray L. Frost. Fourier transform infrared and raman spectroscopic study of the local structure of mg-, ni-, and co-hydrotalcites. *Journal of Solid State Chemistry*, 146(2):506–515, Sep 1999.

[58] Kevin R. Knox, Shancai Wang, Alberto Morgante, Dean Cvetko, Andrea Locatelli, Tevfik Onur Mentes, Miguel Angel Niño, Philip Kim, and R. M. Osgood. Spectromicroscopy of single and multilayer graphene supported by a weakly interacting substrate. *Physical Review B*, 78(20):201408, Nov 2008.

[59] Pavel V. Kolesnichenko, Qianhui Zhang, Tinghe Yun, Changxi Zheng, Michael S. Fuhrer, and Jeffrey A. Davis. Disentangling the effects of doping, strain and disorder in monolayer WS_2 by optical spectroscopy. *2D Materials*, 7(2):025008, Jan 2020.

[60] Stefano Larentis, John R. Tolsma, Babak Fallahazad, David C. Dillen, Kyounghwan Kim, Allan H. MacDonald, and Emanuel Tutuc. Band offset and negative compressibility in graphene-mos2 heterostructures. *Nano Letters*, 14(4):2039–2045, 2014.

[61] Changgu Lee, Xiaoding Wei, Jeffrey W. Kysar, and James Hone. Measurement of the Elastic Properties and Intrinsic Strength of Monolayer Graphene. *Science*, 321(5887):385–388, July 2008. Publisher: American Association for the Advancement of Science Section: Report.

[62] DaeEung Lee, Gwanghyun Ahn, and Sunmin Ryu. Two-Dimensional Water Diffusion at a Graphene–Silica Interface. *Journal of the American Chemical Society*, 136(18):6634–6642, May 2014.

[63] Ji Eun Lee, Gwanghyun Ahn, Jihye Shim, Young Sik Lee, and Sunmin Ryu. Optical separation of mechanical strain from charge doping in graphene. *Nature Communications*, 3(1), January 2012.

[64] Mi-Sun Lee, Kyongsoo Lee, So-Yun Kim, Heejoo Lee, Jihun Park, Kwang-Hyuk Choi, Han-Ki Kim, Dae-Gon Kim, Dae-Young Lee, SungWoo Nam, and Jang-Ung Park. High-Performance, Transparent, and Stretchable Electrodes Using Graphene–Metal Nanowire Hybrid Structures. *Nano Letters*, 13(6):2814–2821, June 2013.

[65] Max C. Lemme, Deji Akinwande, Cedric Huyghebaert, and Christoph Stampfer. 2d materials for future heterogeneous electronics. *Nature Communications*, 13(1):1392, 2022.

[66] F J W-M Leong, M Brady, and J O'D McGee. Correction of uneven illumination (vignetting) in digital microscopy images. *Journal of Clinical Pathology*, 56(8):619–621, Aug 2003.

[67] Hong Li, Qing Zhang, Chin Chong Ray Yap, Beng Kang Tay, Teo Hang Tong Edwin, Aurelien Olivier, and Dominique Baillargeat. From bulk to monolayer mos2: Evolution of raman scattering. *Advanced Functional Materials*, 22(7):1385–1390, 2012.

[68] Liang Li, Renzhi Ma, Yasuo Ebina, Nobuo Iyi, and Takayoshi Sasaki. Positively charged nanosheets derived via total delamination of layered double hydroxides. *Chemistry of Materials*, 17(17):4386–4391, Aug 2005.

[69] T. Li, G.H. Li, L. H. Li, L. Liu, Y. Xu, H.Y. Ding, and T. Zhang. Large-scale self-assembly of 3d flower-like hierarchical ni/co-ldhs microspheres for high-performance flexible asymmetric supercapacitors. *ACS Applied Materials & Interfaces*, 8(4):2562–2572, Feb 2016.

[70] Tsung-Yi Lin, Piotr Dollár, Ross Girshick, Kaiming He, Bharath Hariharan, and Serge Belongie. Feature pyramid networks for object detection. (arXiv:1612.03144), Apr 2017. arXiv:1612.03144 [cs].

[71] Tsung-Yi Lin, Priya Goyal, Ross Girshick, Kaiming He, and Piotr Dollár. Focal loss for dense object detection. (arXiv:1708.02002), Feb 2018. arXiv:1708.02002 [cs].

[72] Rubén Mas-Ballesté, Cristina Gómez-Navarro, Julio Gómez-Herrero, and Félix Zamora. 2d materials: to graphene and beyond. *Nanoscale*, 3(1):20–30, Jan 2011.

[73] Edward McCann and Vladimir I. Fal'ko. Landau-level degeneracy and quantum hall effect in a graphite bilayer. *Physical Review Letters*, 96(8):086805, Mar 2006.

[74] Kathleen M. McCreary, Aubrey T. Hanbicki, Jeremy T. Robinson, Enrique Cobas, James C. Culbertson, Adam L. Friedman, Glenn G. Jernigan, and Berend T. Jonker. Large-Area Synthesis of Continuous and Uniform MoS2 Monolayer Films on Graphene. *Advanced Functional Materials*, 24(41):6449–6454, 2014.

[75] Patrick M. Misun, Jörg Rothe, Yannick R. F. Schmid, Andreas Hierlemann, and Olivier Frey. Multi-analyte biosensor interface for real-time monitoring of 3d microtissue spheroids in hanging-drop networks. *Microsystems & Nanoengineering*, 2(11):1–9, Jun 2016.

[76] T. M. G. Mohiuddin, A. Lombardo, R. R. Nair, A. Bonetti, G. Savini, R. Jalil, N. Bonini, D. M. Basko, C. Galiotis, N. Marzari, K. S. Novoselov, A. K. Geim, and A. C. Ferrari. Uniaxial Strain in Graphene by Raman Spectroscopy: G peak splitting, Gruneisen Parameters and Sample Orientation. *Physical Review B*, 79(20):205433, May 2009. arXiv: 0812.1538.

[77] M. Mohr, J. Maultzsch, E. Dobardzic, S. Reich, I. Milosevic, M. Damnjanovic, A. Bosak, M. Krisch, and C. Thomsen. The phonon dispersion of graphite by inelastic x-ray scattering. *Physical Review B*, 76(3):035439, Jul 2007. arXiv:0705.2418 [cond-mat].

[78] M. Mohr, J. Maultzsch, and C. Thomsen. Splitting of the Raman 2 D band of graphene subjected to strain. *Physical Review B*, 82(20):201409, November 2010.

[79] Shinichiro Mouri, Yuhei Miyauchi, and Kazunari Matsuda. Tunable Photoluminescence of Monolayer MoS2 via Chemical Doping. *Nano Letters*, 13(12):5944–5948, December 2013. Publisher: American Chemical Society.

[80] Zhiping Mu, Dongshan Fu, and Gopinath Kuduvalli. A probabilistic framework based on hidden markov model for fiducial identification in image-guided radiation treatments. *IEEE transactions on medical imaging*, 27(9):1288–1300, Sep 2008.

[81] Niclas S Mueller, Sebastian Heeg, Miriam Pena Alvarez, Patryk Kusch, Soren Wasserroth, Nick Clark, Fredrik Schedin, John Parthenios, Konstantinos Papagelis, Costas Galiotis, Martin Kalbac, Aravind Vijayaraghavan, Uwe Huebner, Otakar Frank, and Stephanie Reich. Evaluating arbitrary strain configurations and doping in graphene with raman spectroscopy. *2D Materials*, 5(1):015016, Nov 2017.

[82] Niclas S Mueller, Sebastian Heeg, Miriam Peña Alvarez, Patryk Kusch, Sören Wasserroth, Nick Clark, Fredrik Schedin, John Parthenios, Konstantinos Papagelis, Costas Galiotis, Martin Kalbáč, Aravind Vijayaraghavan, Uwe Huebner, Roman Gorbachev, Otakar Frank, and Stephanie Reich. Evaluating arbitrary strain configurations and doping in graphene with Raman spectroscopy. *2D Materials*, 5(1):015016, November 2017.

[83] C. Neumann, S. Reichardt, P. Venezuela, M. Drögeler, L. Banszerus, M. Schmitz, K. Watanabe, T. Taniguchi, F. Mauri, B. Beschoten, S. V. Rotkin, and C. Stampfer. Raman spectroscopy as probe of nanometre-scale strain variations

in graphene. *Nature Communications*, 6(1):8429, September 2015. Number: 1 Publisher: Nature Publishing Group.

[84] Zhen Hua Ni, Ting Yu, Yun Hao Lu, Ying Ying Wang, Yuan Ping Feng, and Ze Xiang Shen. Uniaxial Strain on Graphene: Raman Spectroscopy Study and Band-Gap Opening. *ACS Nano*, 2(11):2301–2305, November 2008.

[85] Wataru Norimatsu and Michiko Kusunoki. Epitaxial graphene on SiC{0001}: advances and perspectives. *Physical Chemistry Chemical Physics*, 16(8):3501–3511, January 2014. Publisher: The Royal Society of Chemistry.

[86] Mohammad Norouzi, Vinith Yathindranath, James A. Thliveris, Brian M. Kopec, Teruna J. Siahaan, and Donald W. Miller. Doxorubicin-loaded iron oxide nanoparticles for glioblastoma therapy: a combinational approach for enhanced delivery of nanoparticles. *Scientific Reports*, 10(11):11292, Jul 2020.

[87] K. S. Novoselov, A. K. Geim, S. V. Morozov, D. Jiang, M. I. Katsnelson, I. V. Grigorieva, S. V. Dubonos, and A. A. Firsov. Two-dimensional gas of massless Dirac fermions in graphene. *Nature*, 438(7065):197–200, November 2005. Number: 7065 Publisher: Nature Publishing Group.

[88] K. S. Novoselov, A. K. Geim, S. V. Morozov, D. Jiang, Y. Zhang, S. V. Dubonos, I. V. Grigorieva, and A. A. Firsov. Electric Field Effect in Atomically Thin Carbon Films. *Science*, 306(5696):666–669, October 2004. Publisher: American Association for the Advancement of Science Section: Report.

[89] K. S. Novoselov, A. K. Geim, S. V. Morozov, D. Jiang, Y. Zhang, S. V. Dubonos, I. V. Grigorieva, and A. A. Firsov. Electric Field Effect in Atomically Thin

Carbon Films. *Science*, 306(5696):666–669, October 2004. Publisher: American Association for the Advancement of Science Section: Report.

[90] K. S. Novoselov, A. Mishchenko, A. Carvalho, and A. H. Castro Neto. 2D materials and van der Waals heterostructures. *Science*, 353(6298), July 2016. Publisher: American Association for the Advancement of Science Section: Review.

[91] Jong Sik Oh, Kyong Nam Kim, and Geun Young Yeom. Graphene Doping Methods and Device Applications. *Journal of Nanoscience and Nanotechnology*, 14(2):1120–1133, February 2014.

[92] Jeff Orchard. Globally optimal multimodal rigid registration: An analytic solution using edge information.

[93] Nahee Park, Haeyong Kang, Jeongmin Park, Yourack Lee, Yoojoo Yun, Jeong-Ho Lee, Sang-Goo Lee, Young Hee Lee, and Dongseok Suh. Ferroelectric Single-Crystal Gated Graphene/Hexagonal-BN/Ferroelectric Field-Effect Transistor. *ACS Nano*, 9(11):10729–10736, November 2015. Publisher: American Chemical Society.

[94] H. Peelaers and C. G. Van de Walle. Effects of strain on band structure and effective masses in mos$_2$. *Physical Review B*, 86(24):241401, Dec 2012.

[95] F. M. D. Pellegrino, G. G. N. Angilella, and R. Pucci. Strain effect on the optical conductivity of graphene. *Physical Review B*, 81(3):035411, January 2010. arXiv: 0912.3614.

[96] Vitor M. Pereira and Antonio H. Castro Neto. All-graphene integrated circuits via strain engineering. *Physical Review Letters*, 103(4):046801, July 2009. arXiv: 0810.4539.

[97] S. Piscanec, M. Lazzeri, F. Mauri, A. C. Ferrari, and J. Robertson. Kohn Anomalies and Electron-Phonon Interaction in Graphite. *Physical Review Letters*, 93(18):185503, October 2004.

[98] Istavan Pocsik, Martin Hundhausen, Koos Margit, and Lothar Ley. Origin of the D peak in the Raman spectrum of microcrystalline graphite. *Journal of Non-Crystalline Solids*, (227-230):1083–1086, 1998.

[99] John Proctor, Eugene Gregoryanz, Konstantin Novoselov, Mustafa Lotya, Jonathan Coleman, and M. Halsall. High-pressure Raman spectroscopy of graphene. *Physical Review B*, 80, August 2009.

[100] V. S. Prudkovskiy, K. P. Katin, M. M. Maslov, P. Puech, R. Yakimova, and G. Deligeorgis. Efficient cleaning of graphene from residual lithographic polymers by ozone treatment. *Carbon*, 109:221–226, Nov 2016.

[101] Sergio Puebla, Hai Li, Hua Zhang, and Andres Castellanos-Gomez. Apparent colors of 2d materials. *Advanced Photonics Research*, 3(4):2100221, 2022.

[102] B. Radisavljevic, A. Radenovic, J. Brivio, V. Giacometti, and A. Kis. Single-layer mos2 transistors. *Nature Nanotechnology*, 6(33):147–150, Mar 2011.

[103] Rahul Rao, Ahmad E. Islam, Simranjeet Singh, Rajiv Berry, Roland K. Kawakami, Benji Maruyama, and Jyoti Katoch. Spectroscopic evaluation of

charge-transfer doping and strain in graphene/MoS2 heterostructures. *Physical Review B*, 99(19):195401, May 2019. Publisher: American Physical Society.

[104] Hugo E Romero, Prasoon Joshi, Awnish K Gupta, Humberto R Gutierrez, Milton W Cole, Srinivas A Tadigadapa, and Peter C Eklund. Adsorption of ammonia on graphene. *Nanotechnology*, 20(24):245501, June 2009.

[105] T. Roy, M. Tosun, J.S. Kang, A.B. Sachid, S.B. Desai, M. Hettick, C.C. Hu, and A. Javey. Field-effect transistors built from all two-dimensional material components. *ACS Nano*, 8(6):6259–6264, 2014.

[106] Deblina Sarkar, Wei Liu, Xuejun Xie, Aaron C. Anselmo, Samir Mitragotri, and Kaustav Banerjee. Mos2 field-effect transistor for next-generation label-free biosensors. *ACS Nano*, 8(4):3992–4003, Apr 2014.

[107] Ken-ichi Sasaki, Masayuki Yamamoto, Shuichi Murakami, Riichiro Saito, Mildred S. Dresselhaus, Kazuyuki Takai, Takanori Mori, Toshiaki Enoki, and Katsunori Wakabayashi. Kohn anomalies in graphene nanoribbons. *Physical Review B*, 80(15), October 2009.

[108] F. Schedin, A. K. Geim, S. V. Morozov, E. W. Hill, P. Blake, M. I. Katsnelson, and K. S. Novoselov. Detection of individual gas molecules adsorbed on graphene. *Nature Materials*, 6(9):652–655, September 2007.

[109] Kirby Schmidt, Anthony Trofe, and Tetyana Ignatova. Multimodal image registration of raman spectral maps in two dimensional materials by strain and doping analysis. (arXiv:2207.04292), Jul 2022. arXiv:2207.04292 [cond-mat].

[110] Simranjeet Singh Sekhon, Prabhsharan Kaur, Yang-Hoon Kim, and Satpal Singh Sekhon. 2d graphene oxide–aptamer conjugate materials for cancer diagnosis. *npj 2D Materials and Applications*, 5(11):1–19, Feb 2021.

[111] Jihye Shim, Chun Hung Lui, Taeg Yeoung Ko, Young-Jun Yu, Philip Kim, Tony F. Heinz, and Sunmin Ryu. Water-Gated Charge Doping of Graphene Induced by Mica Substrates. *Nano Letters*, 12(2):648–654, February 2012.

[112] Chen Si, Zhimei Sun, and Feng Liu. Strain engineering of graphene: a review. *Nanoscale*, 8(6):3207–3217, 2016. Publisher: Royal Society of Chemistry.

[113] Eric Singh, Pragya Singh, Ki Seok Kim, Geun Young Yeom, and Hari Singh Nalwa. Flexible molybdenum disulfide (mos2) atomic layers for wearable electronics and optoelectronics. *ACS Applied Materials and Interfaces*, 11(12):11061–11105, Mar 2019.

[114] H. Sirringhaus, T. Kawase, R. H. Friend, T. Shimoda, M. Inbasekaran, W. Wu, and E. P. Woo. High-Resolution Inkjet Printing of All-Polymer Transistor Circuits. *Science*, 290(5499):2123–2126, December 2000. Publisher: American Association for the Advancement of Science Section: Report.

[115] B. H. Son, H. S. Kim, H. Jeong, Ji-Yong Park, Soonil Lee, and Y. H. Ahn. Electron beam induced removal of pmma layer used for graphene transfer. *Scientific Reports*, 7(11):18058, Dec 2017.

[116] C. Stampfer, F. Molitor, D. Graf, K. Ensslin, A. Jungen, C. Hierold, and L. Wirtz. Raman imaging of doping domains in graphene on SiO2. *Applied Physics Letters*, 91(24):241907, December 2007. Publisher: American Institute of Physics.

[117] Ji Won Suk, Alexander Kitt, Carl W. Magnuson, Yufeng Hao, Samir Ahmed, Jinho An, Anna K. Swan, Bennett B. Goldberg, and Rodney S. Ruoff. Transfer of CVD-Grown Monolayer Graphene onto Arbitrary Substrates. *ACS Nano*, 5(9):6916–6924, September 2011. Publisher: American Chemical Society.

[118] Hongyan Sun, Ding Chen, Yuming Wu, Qilong Yuan, Liangchao Guo, Dan Dai, Yang Xu, Pei Zhao, Nan Jiang, and Cheng-Te Lin. High quality graphene films with a clean surface prepared by an uv/ozone assisted transfer process. *Journal of Materials Chemistry C*, 5(8):1880–1884, Feb 2017.

[119] Jie Sun, Xuejian Li, Weiling Guo, Miao Zhao, Xing Fan, Yibo Dong, Chen Xu, Jun Deng, and Yifeng Fu. Synthesis methods of two-dimensional mos2: A brief review. *Crystals*, 7(77):198, Jul 2017.

[120] Xiang Sun, Gongkai Wang, Hongtao Sun, Fengyuan Lu, Mingpeng Yu, and Jie Lian. Morphology controlled high performance supercapacitor behaviour of the ni-co binary hydroxide system. *Journal of Power Sources*, 238:150–156, 2013.

[121] Yan Tao, Li Zaijun, Li Ruiyi, Ning Qi, Kong Hui, Niu Yulian, and Liu Junkang. Nickel–cobalt double hydroxides microspheres with hollow interior and hedgehog-like exterior structures for supercapacitors. *Journal of Materials Chemistry*, 22(44):23587–23592, Oct 2012.

[122] C. Thomsen and S. Reich. Double resonant raman scattering in graphite. *Physical Review Letters*, 85(24):5214–5217, Dec 2000.

[123] Hans Tornatzky, Roland Gillen, Hiroshi Uchiyama, and Janina Maultzsch. Phonon dispersion in mos$_2$. *Physical Review B*, 99(14):144309, Apr 2019.

[124] F. Tuinstra and J. L. Koenig. Raman Spectrum of Graphite. *The Journal of Chemical Physics*, 53(3):1126–1130, August 1970. Publisher: American Institute of Physics.

[125] Shrestha Tyagi, Ashwani Kumar, Manoj Kumar, and Beer Pal Singh. Large area vertical aligned mos2 layers toward the application of thin film transistor. *Materials Letters*, 250:64–67, Sep 2019.

[126] Sami Ullah, Xiaoqin Yang, Huy Q. Ta, Maria Hasan, Alicja Bachmatiuk, Klaudia Tokarska, Barbara Trzebicka, Lei Fu, and Mark H. Rummeli. Graphene transfer methods: A review. *Nano Research*, 14(11):3756–3772, Nov 2021.

[127] Adriana Vela, M. V. O. Moutinho, F. J. Culchac, P. Venezuela, and Rodrigo B. Capaz. Electronic structure and optical properties of twisted multilayer graphene. *Physical Review B*, 98(15):155135, Oct 2018.

[128] Matěj Velický, Alvaro Rodriguez, Milan Bouša, Andrey V. Krayev, Martin Vondráček, Jan Honolka, Mahdi Ahmadi, Gavin E. Donnelly, Fumin Huang, Héctor D. Abruña, Kostya S. Novoselov, and Otakar Frank. Strain and charge doping fingerprints of the strong interaction between monolayer mos2 and gold. *The Journal of Physical Chemistry Letters*, 11(15):6112–6118, Aug 2020.

[129] Pedro Venezuela, Michele Lazzeri, and Francesco Mauri. Theory of double-resonant raman spectra in graphene: Intensity and line shape of defect-induced and two-phonon bands. *Physical Review B*, 84(3):035433, Jul 2011.

[130] Y. P. Venkata Subbaiah, K. J. Saji, and A. Tiwari. Atomically thin mos2: A versatile nongraphene 2d material. *Advanced Functional Materials*, 26(13):2046–2069, 2016.

[131] Iuliia M. Vyshkvorkina, Yury V. Stebunov, Aleksey V. Arsenin, Valentyn S. Volkov, and Sergey M. Novikov. Comparison of cvd-grown and exfoliated graphene for biosensing applications. *AIP Conference Proceedings*, 2359(1):020035, Jun 2021.

[132] N. Wakabayashi, H. G. Smith, and R. M. Nicklow. Lattice dynamics of hexagonal mos$_2$ studied by neutron scattering. *Physical Review B*, 12(2):659–663, Jul 1975.

[133] S. G. Walton, S. C. Hernández, D. R. Boris, Tz B. Petrova, and G. M. Petrov. Electron beam generated plasmas for the processing of graphene. *Journal of Physics D: Applied Physics*, 50(35):354001, Aug 2017.

[134] Xuanye Wang, Jason W. Christopher, and Anna K. Swan. 2D Raman band splitting in graphene: Charge screening and lifting of the K -point Kohn anomaly. *Scientific Reports*, 7(1):13539, October 2017. Number: 1 Publisher: Nature Publishing Group.

[135] Ying Wang, Longhua Tang, Zhaohui Li, Yuehe Lin, and Jinghong Li. In situ simultaneous monitoring of atp and gtp using a graphene oxide nanosheet–based sensing platform in living cells. *Nature Protocols*, 9(88):1944–1955, Aug 2014.

[136] Zhen Wang, Hui Xia, Peng Wang, Xiaohao Zhou, Chunsen Liu, Qinghua Zhang, Fang Wang, Menglin Huang, Shiyou Chen, Peisong Wu, Yunfeng Chen, Jiafu Ye, Shenyang Huang, and Weida Hu. Controllable doping in 2d layered materials. *Advanced Materials*, 33(48):2104942, 2021.

[137] Zhuo Wang, Xin Zhang, Junhui Wang, Linda Zou, Zhaotie Liu, and Zhengping Hao. Preparation and capacitance properties of graphene/nial layered double-

hydroxide nanocomposite. *Journal of Colloid and Interface Science*, 396:251–257, Apr 2013.

[138] F. Withers, O. Del Pozo-Zamudio, A. Mishchenko, A.P. Rooney, A. Gholinia, K. Watanabe, T. Taniguchi, S.J. Haigh, A.K. Geim, A.I. Tartakovskii, and K.S. Novoselov. Light-emitting diodes by band-structure engineering in van der Waals heterostructures. *Nature Materials*, 14(3):301–306, 2015.

[139] S. Yang, C. Jiang, and S.-H. Wei. Gas sensing in 2D materials. *Applied Physics Reviews*, 4(2), 2017.

[140] Lei Ye, Hao Li, Zefeng Chen, and Jianbin Xu. Near-infrared photodetector based on mos2/black phosphorus heterojunction. *ACS Photonics*, 3(4):692–699, Apr 2016.

[141] YuMeng You, ZhenHua Ni, Ting Yu, and ZeXiang Shen. Edge chirality determination of graphene by Raman spectroscopy. *Applied Physics Letters*, 93(16):163112, October 2008.

[142] Dongdong Yu, Feng Yang, Caiyun Yang, Chengcai Leng, Jian Cao, Yining Wang, and Jie Tian. Fast rotation-free feature-based image registration using improved n-sift and gmm-based parallel optimization. *IEEE Transactions on Biomedical Engineering*, 63(8):1653–1664, Aug 2016.

[143] Wenzhi Yu, Kaiwen Gong, Yanyong Li, Binbin Ding, Lei Li, Yongkang Xu, Rong Wang, Lianbi Li, Guangyu Zhang, and Shenghuang Lin. Flexible 2d materials beyond graphene: Synthesis, properties, and applications. *Small*, 18(14):2105383, 2022.

[144] Young-Jun Yu, Yue Zhao, Sunmin Ryu, Louis E. Brus, Kwang S. Kim, and Philip Kim. Tuning the graphene work function by electric field effect. *Nano Letters*, 9(10):3430–3434, Oct 2009.

[145] Kaiyi Zhang, Jianwu Wang, Tianyi Liu, Yifei Luo, Xian Jun Loh, and Xiaodong Chen. Machine learning-reinforced noninvasive biosensors for healthcare. *Advanced Healthcare Materials*, 10:2100734, 2021.

[146] Ying Zhang, Bing Zheng, Changfeng Zhu, Xiao Zhang, Chaoliang Tan, Hai Li, Bo Chen, Jian Yang, Junze Chen, Ying Huang, Lianhui Wang, and Hua Zhang. Single-layer transition metal dichalcogenide nanosheet-based nanosensors for rapid, sensitive, and multiplexed detection of dna. *Advanced Materials*, 27(5):935–939, 2015.

[147] Yuanbo Zhang, Yan-Wen Tan, Horst L. Stormer, and Philip Kim. Experimental observation of the quantum Hall effect and Berry's phase in graphene. *Nature*, 438(7065):201–204, November 2005. Number: 7065 Publisher: Nature Publishing Group.

[148] Zhi-Min Zhang, Shan Chen, and Yi-Zeng Liang. Baseline correction using adaptive iteratively reweighted penalized least squares. *Analyst*, 135(5):1138–1146, Apr 2010.

[149] Jingwen Zhao, Jiale Chen, Simin Xu, Mingfei Shao, Qiang Zhang, Fei Wei, Jing Ma, Min Wei, David G. Evans, and Xue Duan. Hierarchical nimn layered double hydroxide/carbon nanotubes architecture with superb energy density for flexible supercapacitors. *Advanced Functional Materials*, 24(20):2938–2946, 2014.

[150] Yinan Zhong, Fenghua Meng, Chao Deng, Xinliang Mao, and Zhiyuan Zhong. Targeted inhibition of human hematological cancers in vivo by doxorubicin encapsulated in smart lipoic acid-crosslinked hyaluronic acid nanoparticles. *Drug Delivery*, 24(1):1482–1490, Jan 2017.